ABSTRACT

Title of Thesis:	A STUDY ON CRITICAL HEAT FLUX MECHANISMS AND THE TRANSITION TO FILM BOILING
	Jason Christopher Thompson, Master of Science, 2015
Thesis Directed By:	Professor, Jungho Kim, Department of Mechanical Engineering

An infrared (IR) thermometry technique was used to study the critical heat flux (CHF) and the transition to film boiling during pool boiling and submerged jet impingement. Highly resolved temporal and spatial heat transfer measurements were obtained by measuring temperature distributions on the surfaces of an IR transparent test heater with a mid-range IR camera. Measurements were obtained for the nucleate boiling regime, CHF, early transition boiling regime, and through the transition to film boiling. The local heat flux, temperature, and dryout characteristics were used to compare the submerged jet and pool boiling conditions. It was found that similar mechanisms govern CHF and the transition to film boiling. This finding supports that the hydrodynamic models are incorrect, and CHF is governed by the surface characteristics and the dynamics of the microlayer.

A STUDY ON CRITICAL HEAT FLUX MECHANISMS AND THE TRANSITION TO FILM BOILING

By

Jason Christopher Thompson

Thesis submitted to the Faculty of the Graduate School of the
University of Maryland, College Park, in partial fulfillment
of the requirements for the degree of
Master of Science
2015

Advisory Committee:
Professor Jungho Kim (Chair)
Professor Siddhartha Das
Professor Amir Riaz

Acknowledgements

I would like to thank the individuals who contributed to this work. Dr. Kim provided this opportunity and contributed valuable advice. His efforts enabled me to pursue a career that I believe is interesting and important. Luyuan Gong assisted in building the test apparatus and engaged in constructive discussion. Valentin Solotych taught me practical skills that were used to the build the experiment and, along with Alex Scammell, provided useful input. Dr. Thamire motivated me to pursue graduate school and developed my interest in this subject.

Table of Contents

List of Tables

List of Figures

Nomenclature

α	Absorptivity
α_{therm}	Thermal diffusivity
δ	Perturbation
Δt	Time-step
ε	Emissivity
ρ	Reflectivity
A	Area
CHF	Critical heat flux
CLD	Contact line density
CLL	Contact line length
H_j	Jet height
k	Thermal conductivity
L	Contact line length
NB	Nucleate boiling
q”	Heat flux
Q	Heat transfer
T	Temperature
t	Time
TB	Transition boiling
TtFB	Transition to film boiling
v	Contact line speed
WF	Wetted fraction
x_{var}	Arbitrary variable

Subscripts

∞	Ambient condition
c	Camera
l	Liquid
s	Black paint
sat	Saturated
si	Silicon
T	Kapton tape
v	Vapor
W	Wall

Chapter 1: Introduction

Boiling heat transfer equipment is used extensively in industry because it is the most effective way to remove heat while maintaining low system temperatures. However, the performance is limited by the critical heat flux (CHF) and the transition to film boiling, which is usually associated with system failure. The nature of CHF and the transition to film boiling is not well understood. As a result, systems usually operate well below optimal conditions. For example, nuclear power plants, which generate 18% of the worlds electricity, have historically been licensed to operate at less than 85% of CHF to ensure core integrity [1]. Significantly more power could be generated if the power plants could operate closer to CHF or if CHF could be increased.

Numerous studies have been conducted on CHF, and it is important to make a few distinctions. Consider the boiling curves shown in Figure 1. Most research is conducted using the constant wall heat flux condition (left plot), where the transition to film boiling, sometimes called burnout, occurs at CHF. The constant wall temperature case (right plot) demonstrates the transition boiling regime before film boiling. This research was able to capture early transition regime data, due to the test heater characteristics, before rapidly transitioning to film boiling. The observed transition is marked qualitatively by (a) in Figure 1. For these reasons, it is important to distinguish the transition to film boiling and the maximum heat flux of the nucleate boiling regime, CHF.

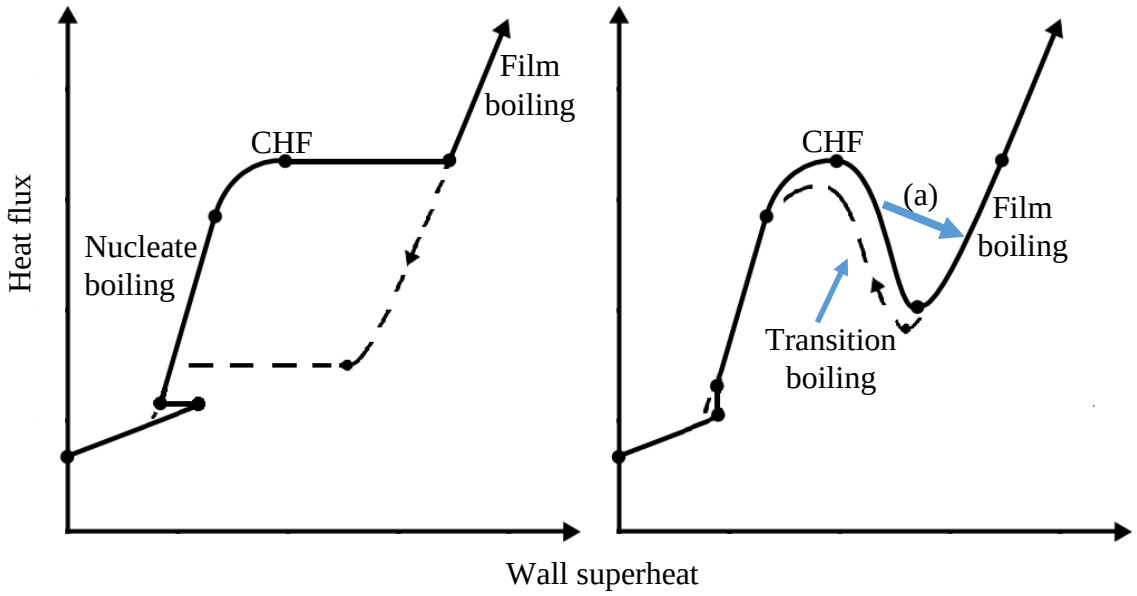

Figure 1: Constant wall flux and temperature boiling curves. The label (a) shows qualitatively where the transition to film boiling occurred during this research. The dashed lines show the hysteresis in the boiling curve.

There is an additional comment on the terminology used to describe CHF and the transition to film boiling. Burnout and total dryout are synonyms for the transition to film boiling. Dryout, dry patches, and dry spots are used to describe vapor concentrations on the test heater surface.

Chapter 2: Literature Review

Section 2.1: Pool Boiling Literature Review

The earliest work on CHF and the transition to film boiling was by Kutateladze [2]. He postulated that the transition to film boiling occurs due to hydrodynamic instabilities between the vapor and liquid. Large vapor columns form on the surface as the heat flux approaches CHF. Liquid droplets fall though the vapor columns to rewet the surface, but they meet more resistance as the heat flux and vapor mass flow rate increases. The transition to film boiling occurs when the liquid droplets cannot penetrate the vapor columns.

Zuber [3], Dihr, and Lienhard [4] refined the hydrodynamic instability model. Their model assumes that CHF occurs when the vapor columns leaving the surface become Helmholtz unstable. The Helmholtz instability is an instability due to a non-zero relative velocity at the liquid-vapor interface. If the relative velocity reaches a critical value, the vapor column will collapse and prevent liquid from rewetting the surface. The critical velocity is defined in Equation 1 where ρ is the density, λ is the Helmholtz unstable wavelength, and σ is the surface tension.

Equation 1

$$u_c \cong \left(\frac{2\pi\sigma}{\rho_v\lambda}\right)^{1/2}$$

Researchers have made a few assumptions to calculate the heat flux that the vapor-liquid interface reached the critical velocity. First, they assumed the vapor columns have a center to center spacing equal to the most dangerous wavelength. The most

dangerous wavelength is the dominant disturbance wavelength when the system becomes Helmholtz unstable as defined in Equation 2.

Equation 2

$$\lambda_D = 2\pi \left(\frac{3\sigma}{(\rho_l - \rho_v)g}\right)^{1/2}$$

They also defined the radius of the vapor columns as $\lambda_D/4$ and the Helmholtz unstable wavelength as λ_D. Last, the vapor mass flow rate is calculated, by assuming all of the heat is used to convert liquid to vapor, and set equal to the liquid mass flow rate. The heat flux at which the interface becomes unstable is defined in Equation 3, where h_{lv} is the latent heat of vaporization.

Equation 3

$$q"_{CHF,Zuber} = 0.131\rho_v h_{lv} \left(\frac{\sigma(\rho_l - \rho_v)g}{\rho_v^2}\right)^{1/4}$$

Equation 3 has had reasonable agreement with experimental data, and hydrodynamic stability models have been the status quo for over half a century. However, most of the assumptions made by Zuber, Lienhard, and Dihr do not have a strong theoretical basis. For example, the vapor column geometry has not been experimentally observed. The agreement with experimental data may be simply because Equation 3 includes the important thermal properties and are in dimensional agreement with the heat flux. As a result, new theoretical models have been postulated.

Rohsenow and Griffith [5] stated that CHF occurs when the nucleation sites reached a critical bubble packing. The critically packed nucleation sites coalesce and the liquid cannot penetrate to rewet.

Haramura and Katto developed the macrolayor model [6]. This model suggests that large vapor bubbles form and hover over the surface in the slug and column nucleate boiling regime. A liquid film and vapor regions are trapped beneath the large bubble. Below CHF, the hovering bubble regularly departs and the liquid is replenished. CHF occurs when the liquid layer is depleted before the vapor bubble departs. Guan et al. [7] state that the vapor bubble departs based on a vapor momentum condition. The researchers use the momentum condition to predict how CHF should increase with system pressure and show good agreement with experimental data. Rajvanshi et al. [8] predicted the initial thickness of the film beneath the macrolayer by assuming a correlation with the bubble frequency as a function of distance from the heater surface. Kim and Ahn [9] use a visualization technique to confirm the existence of a macrolayer under a large vapor mushroom. Ma and Dihn [10] studied the rupture dynamics of evaporating liquid films. This research provided insight to liquid film dynamics beneath the macrolayer. Bang et al. [11] confirmed the existence of a liquid film beneath a large vapor clot. However, their visual data did not show that the large vapor bubble needed to depart for rewetting to occur. In addition, they found that local dry patches beneath the vapor clot are the source of burnout. Other researchers have also shown visual evidence that contradicts the macrolayer model, and the validity of the model has come under question.

The previous CHF models have only considered hydrodynamic phenomenon, but many researchers believe that the surface-liquid interaction is significant. Kandlikar [12], [13] researched the contact angle and its effect on CHF. He

developed a new hydrodynamic model that postulated that CHF occurs when the momentum forces due to evaporation at the triple phase contact line exceed the surface tension and gravity forces. His model has shown good agreement with experimental data and follows the experimentally observed trend that non-wetting fluids have low CHF.

O'Connor and You [14] used a painting technique to enhance heat transfer by creating a thin porous surface. They found that they could reduce the superheat to initiate pool boiling by 85%, decrease the superheats in the nucleate boiling regime by 75%, and increase CHF by 109% with their surface enhancement.

Buongiorno et al. [15] studied the separate effects of surface roughness, wettability, and porosity. The surface roughness is the RMS deviation from the average surface position. It is known that rough surfaces trap more vapor and increase the nucleation site density, which decreases the wall superheats for the onset of nucleation and in the nucleate boiling regime. The effect of surface roughness on CHF has been widely speculated. The porous surfaces are defined by their void fraction and pore dimensions, and induce capillary action, or wicking. They found that surface porosity had a significant effect on CHF. Surface wettability was less important, and surface roughness was insignificant.

McCarthy et al. [16] studied the surface wickability, roughness, and morphology and their effect on CHF. The researchers classify the wickability by measuring the rate the surface draws fluid from a capillary tube, defined as the wicked volume flux, V_o". They found that the surface wickability was the single key factor in dictating CHF on highly wetting surfaces. They defined the dimensionless

wicking number *Wi* as shown in Equation 4, and indicate that CHF can be expressed in terms of *Wi* as shown in Equation 5.

Equation 4

$$Wi \equiv \frac{V_o" \rho_l}{\rho_v^{1/2}[\sigma g(\rho_l - \rho_v)]^{1/4}}$$

Equation 5

$$\frac{q"_{CHF,Wicking}}{q"_{CHF,Zuber}} = 1 + Wi$$

Infrared (IR) technology has recently developed and has been a useful tool for analyzing boiling mechanics, e.g., Theofanous [17,18], Buongiorno [19], and Kim [20]. Theofanous' research was among the most enlightening. He began by highlighting the contradicting results throughout the literature with respect to hydrodynamic instability phenomena. He observed that Zuber's model is based on a specific heater configuration, but the results have been generalized and applied to other configurations, such as boiling on submerged wires, confined horizontal plates, etc. He claimed that the indiscriminant application of this theory and the practice of creating universal models based of non-universal testing configurations has led to the development of inappropriate models, such as the macrolayer. He further doubted the validity of hydrodynamic models because of their inability to account for the large scatter in CHF data, the documented effects of surface enhancement, and their poor agreement with reduced and microgravity measurements. His research used IR technology to make surface temperature measurements and x-ray radiography to measure the void fraction of the flow field. He observed reversible dry spots that formed on the surface at low heat fluxes. As the heat flux approached CHF, these dry spots did not rewet (they become irreversible) and triggered transition to film boiling.

He concluded that macro flow fields above the test heater did not show any connection to the local dry patches observed on the test surface, and that the CHF behavior must be governed solely by the surface characteristics and micro dynamics.

The dry patch dynamics described by Theofanous have also been observed by other researchers. For example, Chu, No, and Song [21] used a total internal reflection technique to study dry patch formation near CHF. They determined that the dry patches form due to the lateral coalescence of growing bubbles. Nishio and Tanaka [22] studied the contact line density, defined as the length of contact line per unit area, with a visual light optical technique. They found that the contact line density increases until burnout at CHF.

The present work is an extension of work by Jung, Kim, and Kim [23] that also studied dry patch behavior. Similar test heater and data acquisition techniques [20] were used in both experiments. The researchers studied the contact line movement, contact line density, wetted fraction, dryout frequency, average dryout duration, and the distribution of dry spot sizes to characterize CHF mechanisms.

Many researchers have studied the effects of subcooling and pressure on CHF [24 - 26]. It has been observed that subcooling generally increases CHF because vapor columns condense more rapidly and offer less resistance to inflowing liquid.

Section 2.2: Impinging Jet Literature Review

Impinging jet experiments have significantly more configurations and design variables than pool boiling experiments. An impinging jet is classified as free if it is in an air or vapor atmosphere, submerged when it is submerged within a liquid pool, and confined if the nozzle has a flanged exit. The flanged nozzle exit creates a flow channel between itself and the heated wall. The impinging jet is also defined by the flow rate, degree of subcooling, distance from heated surface, fluid development length, nozzle cross-sectional shape, and nozzle cross-sectional area.

A heated wall subjected to an impinging jet is divided into the stagnation region, directly under the jet, and the parallel flow region, where the flow is parallel to the wall. The boiling curve for an impinging jet is shown in Figure 2. Qualitatively, the parallel flow region has the same boiling curve as pool boiling. However, the stagnation region has unique behavior in the transition regime, where heat transfer is much higher. This regime has been studied by Seiler [27], Auracher [28], Robidou [29], and many more. The enhanced heat transfer occurs because the jet breaks up dry patches and creates microbubbles, which induce better mixing. The heat transfer in this regime is strongly dependent on the subcooling, jet velocity, and jet configuration.

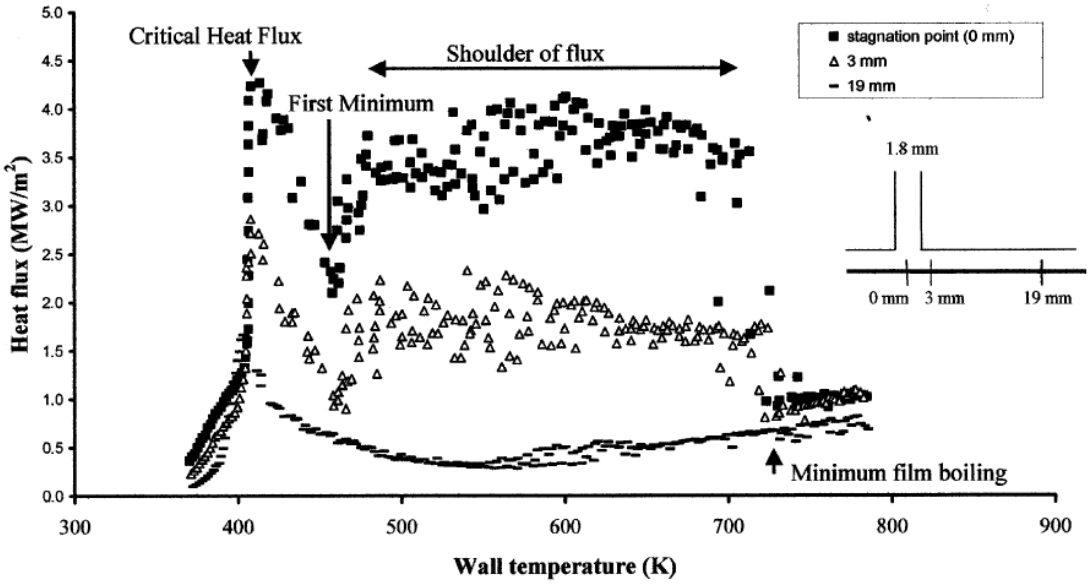

Figure 2: Confined impinging water jet boiling curve [27]**. The stagnation region (located under the impinging jet) has significantly higher heat transfer in the transition boiling regime, because the jet breaks up dry patches and produces enhanced mixing. Otherwise, the boiling curves qualitatively follow the pool boiling behavior.**

The single phase heat transfer was studied by Wolf [30]. He found that the heat transfer is not a function of the wall superheat or heat transfer, but only the jet configuration. He also observed that the single phase heat transfer becomes less efficient with radial distance. Incropera et al. [31, 32] studied the effect of using a two phase jet, and found that it enhances the convection before the onset of nucleate boiling. Wolf and Auracher et al. [28] found that the nucleate boiling heat transfer is not a function of radial distance, jet velocity, jet height, or jet classification, but CHF was strongly dependent on these variables.

Generally, CHF models are not used for impinging jet heat transfer. The wide variety of jet configurations are difficult to capture with a single model, so empirical correlations are used. The correlations vary based on the jet configuration. Lienhard et al. [33] offers a correlation for an impinging free jet on a disk heater. Qui et al. [34] recommends a correlation for saturated liquids from free jets impinging on a

horizontal heater in the stagnation region. They found that CHF is proportional to $(V/d)^{1/3}$ and $(\rho_v/\rho_l)^{1.4/3}$, where V is the jet velocity and d is the jet diameter.

Researchers have recently started investigating surface enhancement for impinging jet heat transfer. Qiu et al. [35] used a hydrophilic surface treatment to increase CHF by approximately 30% for a free water jet impinging on a flat heater. The enhancement was independent of jet velocity and subcooling. Garimella et al. [34, 35] used microporous structures to increase CHF by approximately 100% in a variety of jet configurations.

There has also been significant research to optimize CHF with respect to the jet configuration. Cho et al. [38] studied the nozzle-plate spacing for confined jet impingement. They found that CHF did not have a monotonic relationship with the jet spacing, and they proposed a correlation to calculate CHF with different configurations. Garimella et al. [39] also investigated the optimal confined impinging jet geometry. They studied the optimal jet diameter (d) and length (l) aspect ratio (l/d), and found that very small aspect ratios had the highest heat transfer coefficients.

Jet impingement has been used to quench superheated materials, which usually results in film boiling. Liu and Wang [40] used simplified two phase boundary layer equations to make a semi-empirical correlation to predict the wall Nusselt number during film boiling. Timm et al [41] studied the amount of subcooling necessary to avoid the film boiling regime during quenching.

Chapter 3: Experimental Technique

This section describes the experimental technique. The apparatus, data acquisition system, and test conditions are described first, followed by a description of the data post processing technique and validation. Finally, the experimental uncertainty is evaluated.

Section 3.1: Apparatus, Data Acquisition and Test Conditions

3.1.1 Apparatus

The experiments were conducted using the apparatus shown in Figure 3. The chamber was sealed to the atmosphere using butyl O-rings and thin butyl sheets. The main subsystems for the apparatus were the auxiliary heaters, condenser, bellows, test heater, and the jet flow loop.

Film heaters were placed around the outside of the chamber so the saturation conditions in the chamber could be controlled. A PID controller was used to actuate a relay that connected 115 V AC power to the 35 Ω heaters.

The condenser loop was in the vapor space above the liquid in the chamber. It circulated water from an ice bucket and was manually actuated. The purpose of this system was to prevent saturation pressure from exceeding atmospheric pressure, and it was used in conjunction with the film heaters.

The top half of the chamber contained stainless steel bellows and its housing. The equilibrium bellow position was set to be about the midpoint in the housing, so it had compliance to expand or contract to maintain the system at approximately atmospheric conditions as boiling occurred.

The test heater was located at the bottom of the chamber on an aluminum plate. A hole in the plate provided optical access to the test heater. The test heater is described in more detail in a following subsection.

A gear pump was used to pump liquid from the bottom of the pool through a 2 mm diameter x 13.5 mm long nozzle and onto the test heater. Acrylic tubes were used to transport the fluid on the outside of the chamber to insulate it. Approximately 5 cm of ¼" copper tube submerged within the saturated pool were used to transport the fluid to the test heater. The nozzle was connected to the copper tube with a Swagelok ¼" fitting. A hand calculation was used to verify that the liquid would remain at saturated conditions and no condensation was observed on the copper tube in the vapor space of the chamber.

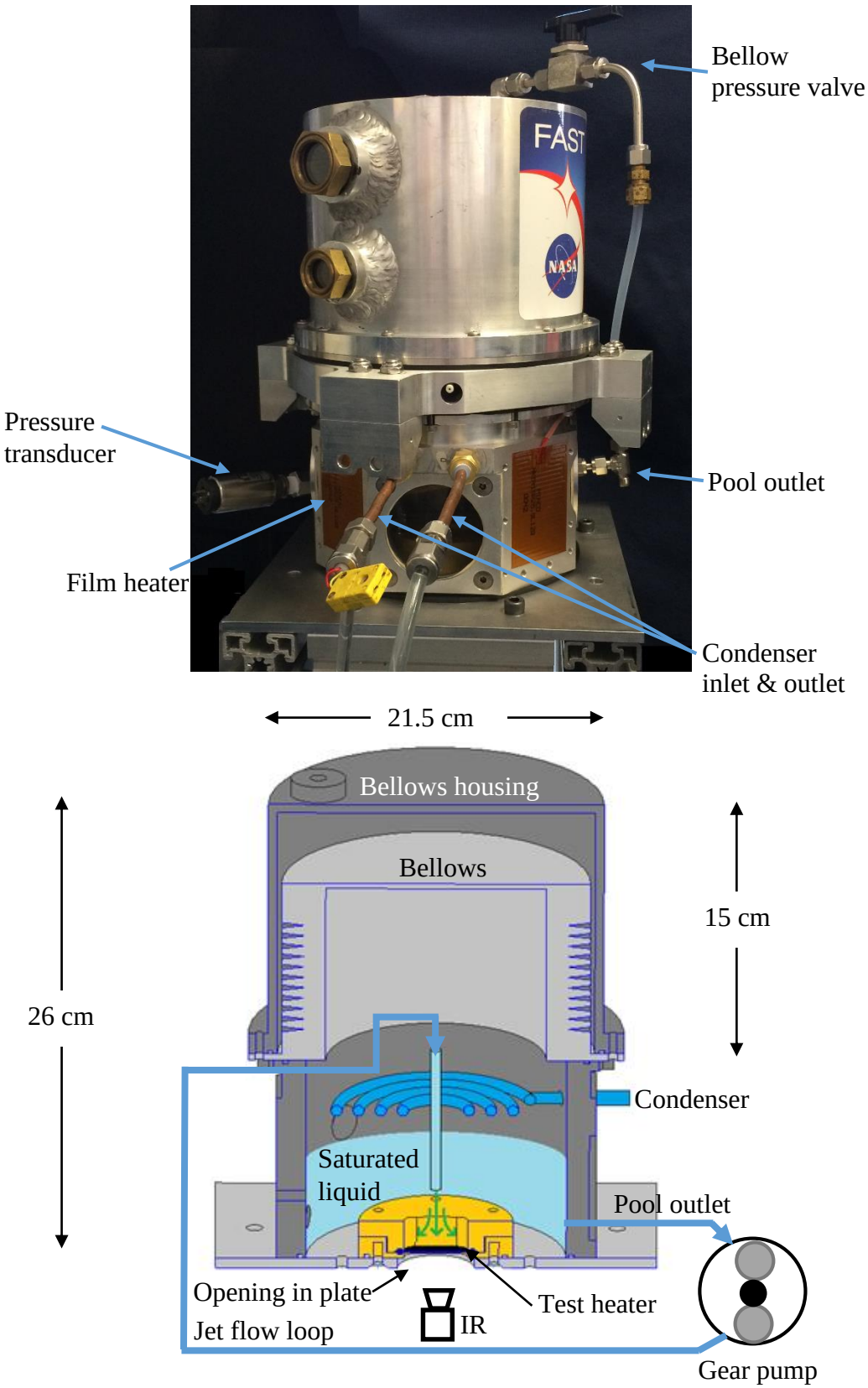

Figure 3: Test apparatus. The main subsystems were the film heaters, condenser, bellows, test heater, and the jet flow loop. The IR camera had optical access to the test heater.

3.1.2 Test Fluid: Novec 7000

The refrigerant Novec 7000 (previously HFE-7000) was used for all experiments. It has a saturation temperature of 35 ˚C at atmospheric pressure. Table 1 shows the fluid properties at room temperature and Figure 4 shows the pressure and temperature saturation curve. The fluid is compatible with the butyl seals used for the apparatus.

Table 1: Novec 7000 liquid properties.

Temperature [˚C]	25
Density [kg/m^3]	1400
Thermal conductivity [W/m-K]	0.075
Kinematic Viscosity [m^2/s]	0.32
Specific Heat [J/kg-K]	1300
Surface Tension [dynes/cm]	12.4
Latent Heat of Vaporization [kJ/kg]	142

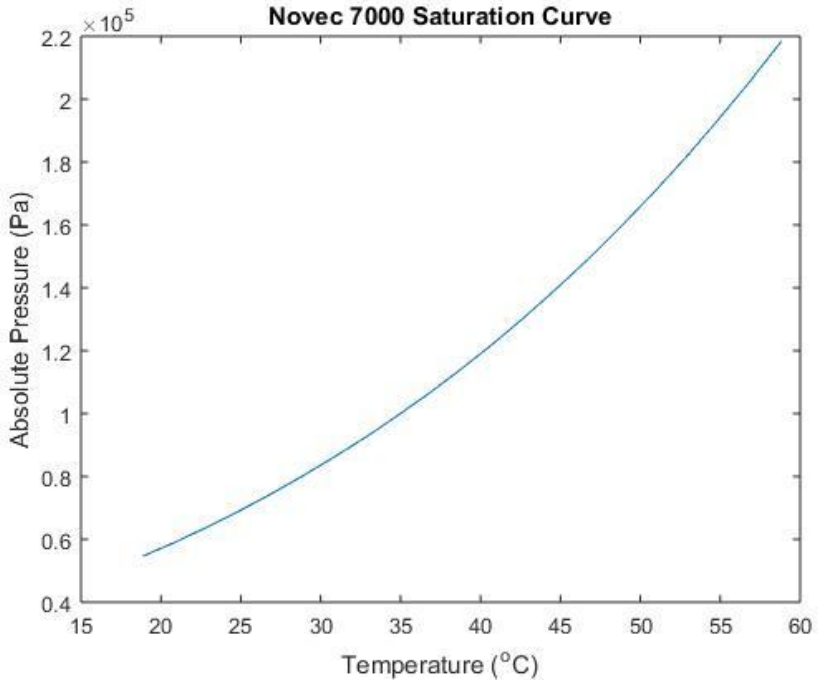

Figure 4: Novec 7000 saturation curve.

3.1.3 Test Heater

The test heater (Figure 5) consisted of a silicon substrate that was 44 x 22 x 0.5 mm. Kapton tape, 38 μm thick, was placed on top of the silicon substrate, followed by a 6 μm silkscreened layer of IR black paint.

The Kapton tape and silicon were IR transparent, so the black paint was the temperature measured by the IR camera. The paint was thin and had a high thermal conductivity, so it was assumed that it was uniform temperature in the z-direction. The Kapton tape acted as an insulator and inhibited heat from spreading in the lateral directions. If the tape was not present, the temperatures gradients would have been small and the triple phase contact line would have been unresolved. The Kapton tape and black paint were also placed on the bottom side of the silicon as a second temperature reference. The silicon had much larger thermal mass than the Kapton and its temperature did not change rapidly, so it was assumed that the thermal resistance of the Kapton tape did not affect the measurement. The temperature measurements are explained more detail in Section 3.2: Post Processing. The important optical and thermal properties of the test heater are displayed in Table 2. The optical properties were evaluated experimentally by the process described in Kim et al. [20].

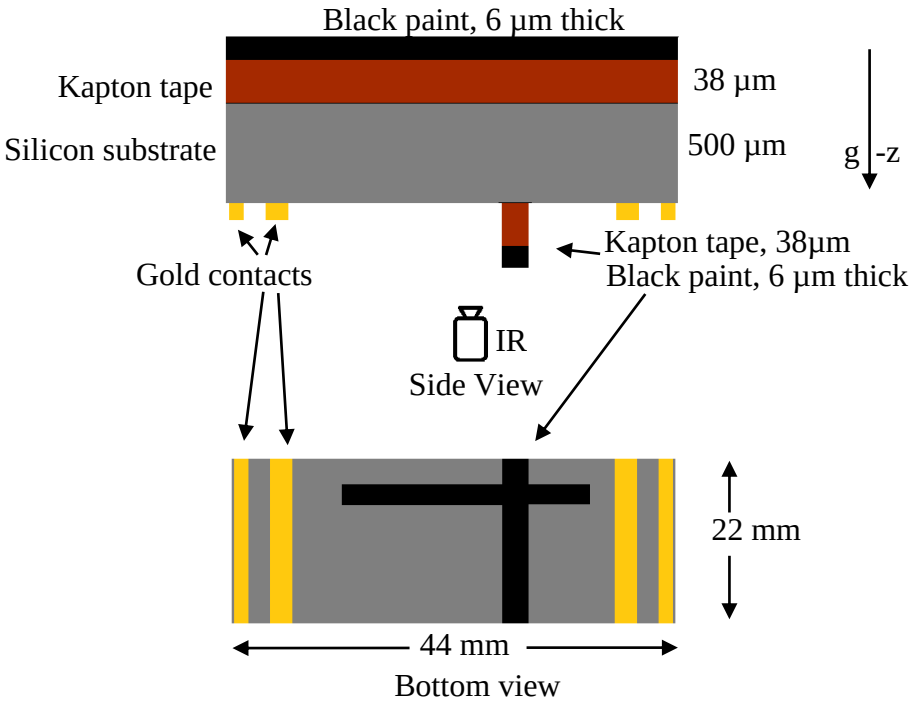

Figure 5: Test heater. The heater consisted of a 44 x 22 x 0.5 mm silicon substrate, covered with 38 µm thick Kapton tape, and 6 µm of black paint.

Table 2: Important test heater thermal and optical properties.

Experimental constant	Value	Uncertainty
Kapton thermal conductivity (k_T)	0.12 (W/mK)	0.01 (W/mK)
Kapton thermal diffusivity ($\alpha_{thermal,T}$)	$7.753*10^{-8}$ (m^2/s)	$5*10^{-9}$ (m^2/s)
Absorptivity of Kapton (α_T)	7110 (m^{-1})	500 (m^{-1})
Absorptivity of silicon (α_{si})	21 (m^{-1})	0.1 (m^{-1})
Reflectivity of silicon-air interface ($\rho_{\infty\text{-}si}$)	0.36	0.008
Reflectivity of silicon-Kapton interface ($\rho_{si\text{-}T}$)	0.12	0.006
Emissivity of black paint (ε_s)	0.9	0.01
Reflectivity of air-black paint interface (ρ_s)	0.1	0.01

The silicon had isentropic boron doping and a resistivity between 1 and 3 Ω-cm. The silicon was joule heated and required contacts for electric leads, which were added in a three step process. First, boron dopant was spin coated on at the contact locations and the silicon was doped again to minimize the contact resistance. The silicon was annealed for 45 minutes at 1025 ˚C and the dopant penetrated approximately 1 μm into the silicon. Next, 200 angstroms of chromium was sputtered on at the contacts. The chromium served as an electrically conductive adhesive between the gold and silicon. Finally, 1500 angstroms of gold was sputtered on top of the chromium. Electrical leads were soldered to the gold contacts. The contact resistance was negligible, and a 4 wire measurement was used to determine that the

silicon had a resistance of 26 Ω between the inner leads at room temperature. However, the resistance increased with temperature and was approximately 55 Ω at 200 °C.

The test heater was clamped between butyl O-rings in two Hydlar Z (made from Kevlar) holders. O-rings were used because the fluid would decompose silicone and most epoxies, which contaminates the fluid. The holder cross-section is shown in Figure 6. A problem with this geometry was that the Kapton tape tended to delaminate at the O-ring contacts. The silicon expanded with temperature at a greater rate than the Hydlar Z holder and the O-rings resisted the tape movement, causing it to delaminate.

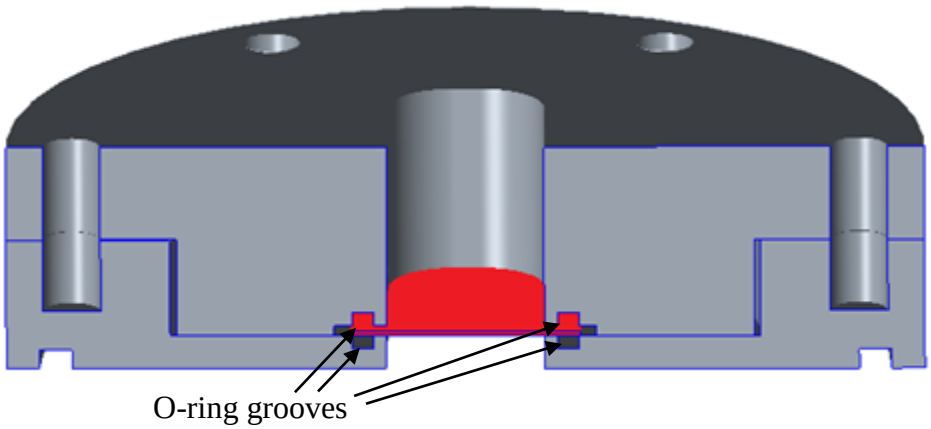

Figure 6: Test heater and holder. The test heater is shown in red and was sealed using butyl O-rings.

The heater was designed to act like an infinite boiling surface. The boiling surface was surrounded by 1.9 cm walls to prevent liquid resupply from the sides. The minimum length dimension of the surface was approximately 14 mm, which is larger than the most dangerous wavelength for Novec 7000 (10.3 mm).

3.1.4 Instrumentation and Data Acquisition

Pressure, temperature, and volumetric flow rate measurements were made during the experiments. The instrumentation is listed in Table 3. Altair software was used to interface with the IR camera and store videos of the test heater. The pressure transducer, thermocouple, and flowmeter data was acquired using conditioning circuits, Arduino Uno, and LabVIEW software. This data was used to determine the saturation conditions and the volumetric flow rate of the jet.

Table 3: Summary of Instrumentation.

	Model	Range	Uncertainty	Output
Flowmeter	Omega FLR 1000	0-200 ml/min	±1.0 ml/min	0-5 V
Pressure transducer	Omega PX 212	0-202650 Pa	±400 Pa	0-100 mV
Thermocouple	K-type	-200-1350 °C	±0.2 °C	-6-55mV
IR-Camera	FLIR5600	30-200 °C	±1.0 °C	N/A

The pressure transducer and thermocouple signals were conditioned to be between 0 and 5 volts by using the circuits highlighted in Figure 7. The pressure transducer was conditioned by using voltage followers and a differential amplifier.

An adafruit K-type AD8495 Breakout thermocouple amplifier was used for each of the four thermocouple measurements. The unconditioned amplifier had a dynamic range of 1000 °C and the Arduino resolution was only about 1°C. Voltage followers and a non-inverting amplifier circuit were used to condition each thermocouple amplifier and improve resolution. Three thermocouples were conditioned to measure temperatures from 0 to 80°C, and the last was conditioned for 0 to 200°C.

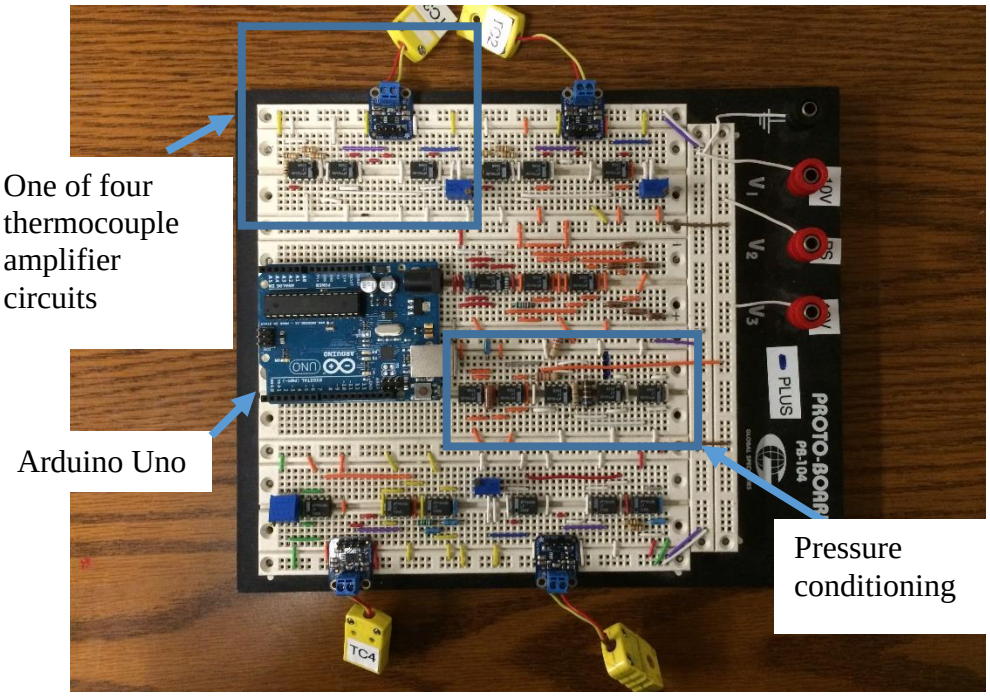

Figure 7: Signal conditioning circuits for the thermocouples and pressure transducer. The thermocouple, pressure transducer, and flowmeter data was acquired using Arduino Uno.

The pressure transducer, thermocouples, and flow meter were each calibrated and the results are shown in Figure 8 to Figure 10. The flow meter had nonlinear behavior, so the calibration was repeated three times.

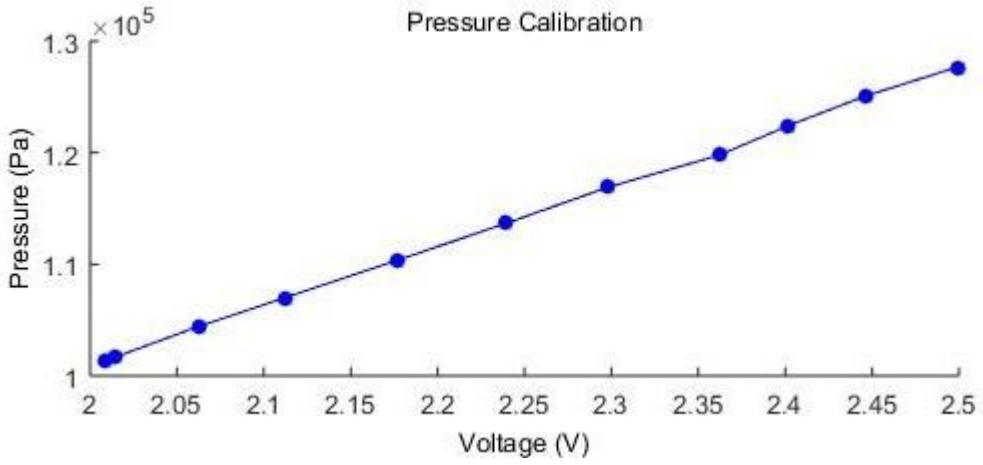

Figure 8: Pressure transducer calibration results.

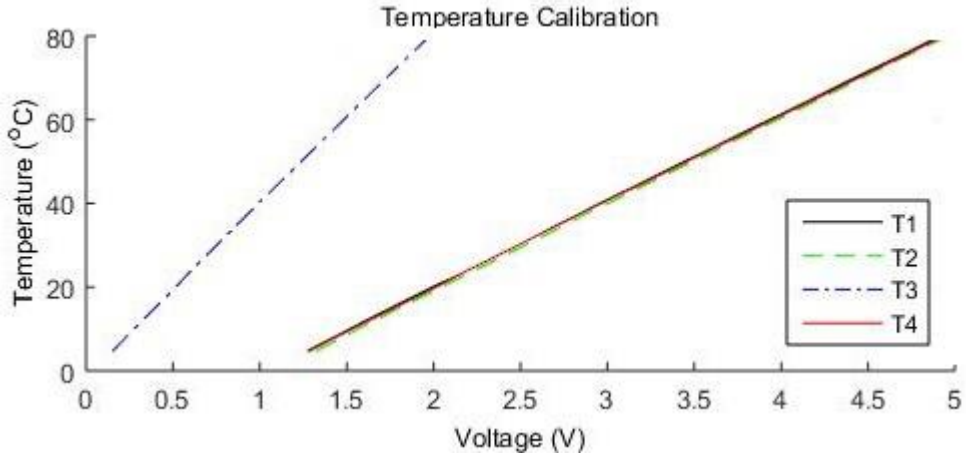

Figure 9: Temperature calibration. T1, T2, and T4 were conditioned to measure 0 to 80 °C. T3 was conditioned to measure 0 to 200 °C.

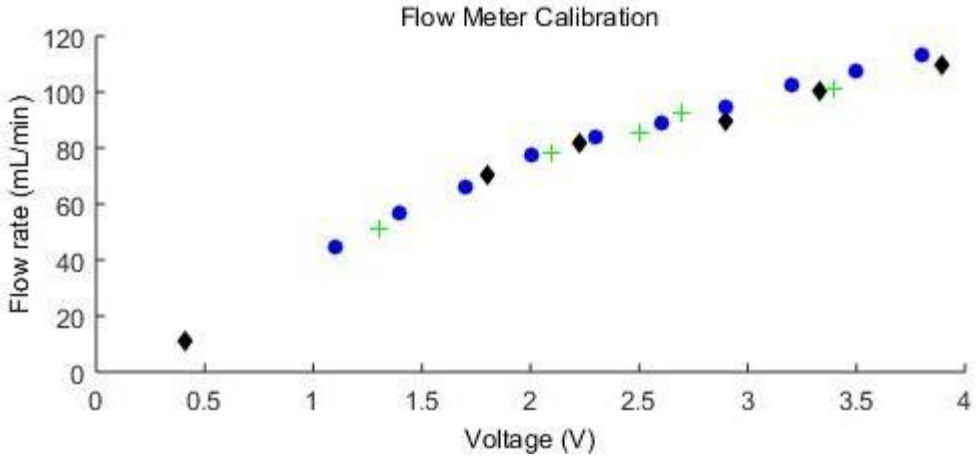

Figure 10: Flowmeter calibration results.

A FLIR5600 midrange (3.0-5.1 μm) infrared (IR) camera was used to measure the temperature of the heater (the black paint shown in Figure 5). IR radiation was received by the CCD of the camera and the software converted it to temperature by assuming the camera was viewing a black body (a surface with emissivity of 1). The heater was not a black body, however, and the data was altered by the layers of the test heater and the reflections at interfaces. This problem is addressed in Section 3.2: Post Processing.

The temperatures differences on the test heater ranged up to 140 ˚C. A sample temperature distribution near CHF is shown in Figure 11. The camera needed to use multiple integration times (ITs), or shutter times, to accurately resolve temperature ranges this large (greater than approximately 70 ˚C). The camera alternated the IT every frame and then the software saved a video for each IT. Each video had a unique range of accurate temperature data.

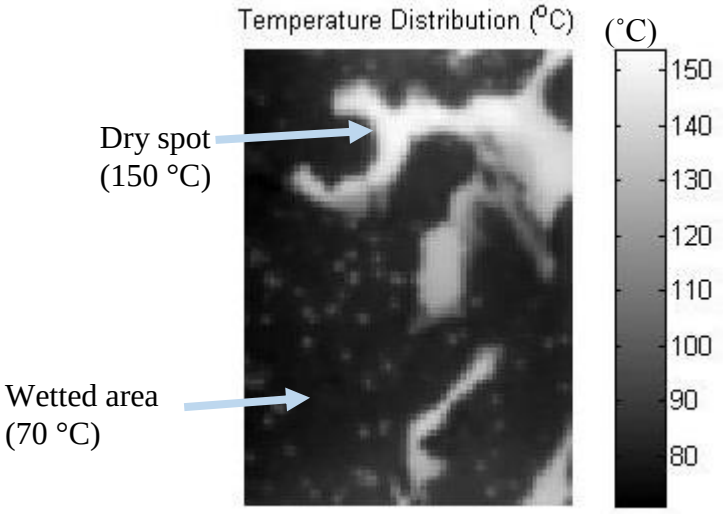

Figure 11: A sample temperature distribution near CHF. The camera must use multiple integration times to accurately resolve temperature ranges this large.

The camera could not accurately measure temperatures above the calibration range for a given IT, because the pixels became saturated. However, the camera had reasonable accuracy when it measured temperatures below the minimum of the calibration range. Consider Figure 12 as an example. Two ITs were used to measure nucleate boiling on the test heater and the measurements were separated by 0.0012 seconds. The first IT was calibrated for 40 to 89 °C and could accurately measure the test heater temperatures. The second IT was calibrated for temperatures above 80 °C,

which was about 20 °C above the maximum heater temperature. The absolute difference in temperatures is plotted in the right image. The average difference was 0.8 °C and some error may be attributed to the transient behavior between frames.

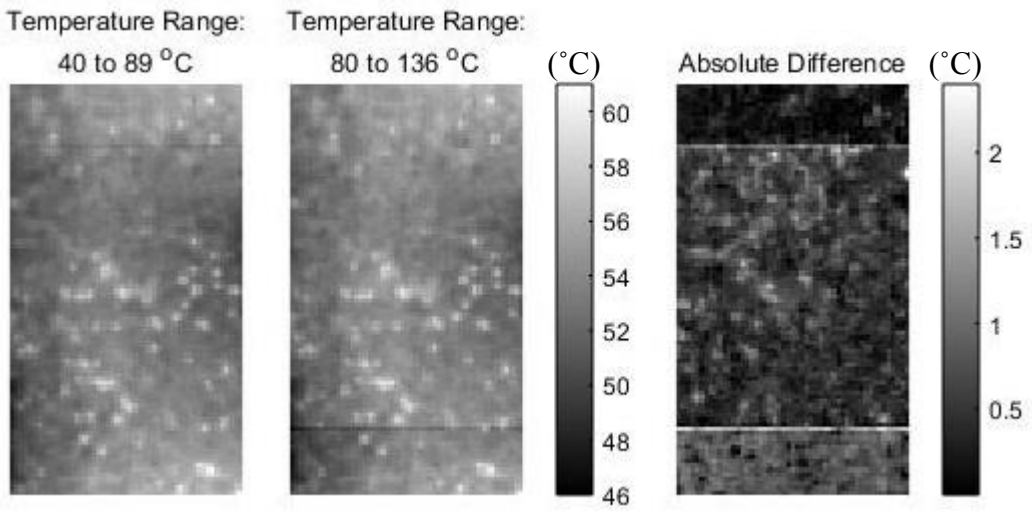

Figure 12: IT comparison #1. The left most image is a temperature measurement with an IT calibration range of 40 to 89 ˚C. The middle image has an IT calibration range of 80 to 136 ˚C. The right most image is the absolute difference between them. The error associated with using the IT with a calibration range greater than the measured temperatures was small.

The error increased as the temperature measurements were farther out of the calibration range. Figure 13 shows that error increased by an order of magnitude when the measured temperature was 50 °C less than the minimum of the calibration range.

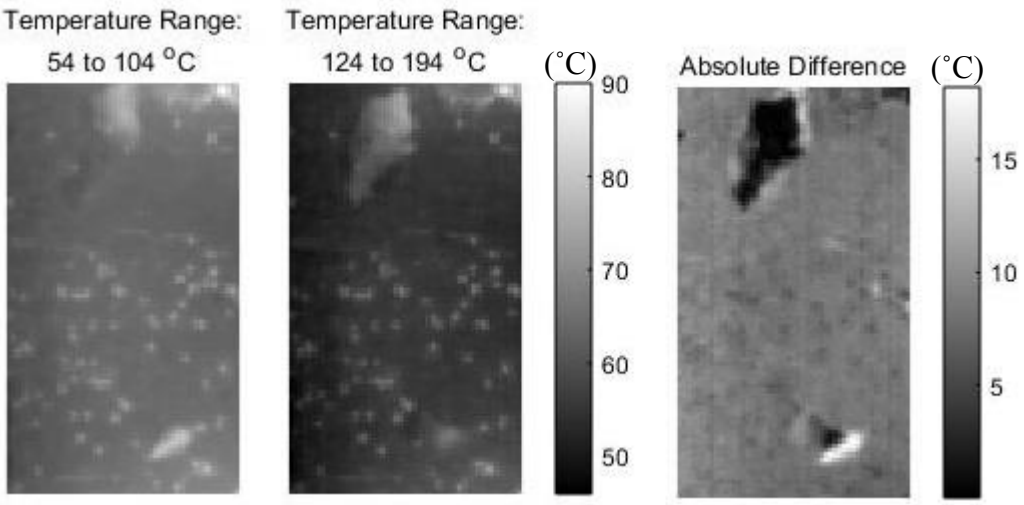

Figure 13: IT comparison #2. The left most image is a temperature measurement with an IT calibration range of 54 to 104 ˚C. The middle image has an IT calibration range of 124 to 194 ˚C. The right most image is the absolute difference between them. The error associated with using the IT with a calibration range greater than the measured temperatures was large.

An alternative methodology would be to use only one IT with a reasonably high calibration range and sacrifice accuracy at lower temperatures. The advantage is that the spatial and temporal resolution could be increased, but the user would need to be cautious of the issues demonstrated in Figure 13.

The camera frequency, number of ITs, and heat flux is summarized in Table 4 for each experiment (see **3.1.6 Test Conditions**). Only a representative sample is included, and complete tables for each experiment are in the **Appendix**. The recorded frequency in the table is for each IT, so the camera frequency was the reported frequency multiplied by the number of ITs.

Table 4: Summary of camera settings during all experiments.

Experiment number	Heat flux (W/cm^2)	Number of integration times (IT)	Frequency per IT (Hz)	Was dryout present?
1	4.7	1	839	No
1	10.8	2	420	Yes
1	18.4	3	167	Yes
1	CHF	3	167	Yes
2	4.7	1	500	No
2	10.6	2	250	Yes
2	17.1	2	250	Yes
2	CHF	2	250	Yes
3	5.0	1	200	No
3	12.2	2	250	Yes
3	15.4	2	250	Yes
3	CHF	2	250	Yes
4	4.5	1	200	No
4	10.22	2	250	Yes
4	21.65	2	250	Yes
4	CHF	2	250	Yes

One final point regarding the IR camera that is relevant to the post processing is that the radiation measured by one pixel had a small dependence on the neighboring pixels. This caused the camera to smear a step change in temperature. As a result, a step change in temperature could not be accurately resolved if less than approximately eight pixels were used. For this reason, the black tape on the bottom surface of the silicon was at least eight pixels wide, as demonstrated in Figure 14.

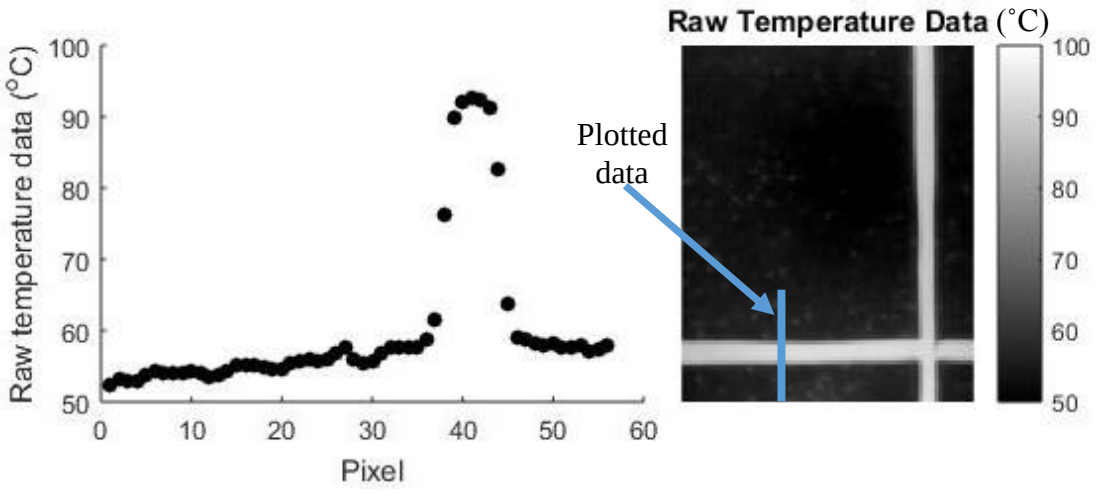

Figure 14: Camera smearing example. The dark regions of the temperature image are nucleate boiling observed on the top surface. The white lines are the black paint on the bottom of the silicon, and they were at least 8 pixels wide to ensure that the camera could accurately measure the temperature.

3.1.5 Data Collection Procedure

The test apparatus was degassed (i.e., non-condensables were removed) and at saturated conditions before any measurements were made. To degas, the chamber (Figure 3) was flipped upside down and approximately 1/3 of the volume was filled with the test fluid. A vacuum was then pulled at the highest point of the test chamber to boil the fluid and remove non-condensables. To avoid wasting fluid, the vacuum on the chamber was only held for a few seconds, and the chamber was then allowed to return to equilibrium. The chamber conditions were compared to saturation conditions to determine the state of degassing. Usually five repetitions of the above process were necessary to remove non-condensables to below 5000 ppm.

Heat transfer measurements were obtained by recording IR videos of the test heater. The camera was located approximately 0.3 m below the test heater and allowed to reach an equilibrium temperature before the experiments to ensure the

ambient conditions were not changing as data was collected. The flow rate, system pressure, and bulk fluid temperature were recorded for each IR measurement.

The first measurement was of the unheated test heater, which was at the same temperature as the bulk fluid. The jet was used for this measurement in all four experiments to increase convection and promote uniform temperatures within the test heater. This measurement was used to calculate the ambient conditions and is discussed in more detail in Section 3.2: Post Processing. The heat transfer measurements were taken next. The voltage supplied to the test heater was slowly increased and the system was allowed to stabilize for a few minutes. A measurement was taken at each heat flux and the process was continued until film boiling was achieved. Video measurements were between 2 and 60 seconds.

3.1.6 Test Conditions

This subsection summarizes the conditions for each of the four experiments conducted. All experiments were conducted at saturated conditions on an upward facing heater. The test conditions were defined as the jet configuration, volumetric flow rate, state of degassing, and saturation pressure (and temperature).

The jet was submerged, 13.5 mm long, 2 mm in diameter, and at saturated conditions for all four experiments. The control variables were the jet height and flow rate. A cross-section of the test conditions is shown in Figure **15** and the test matrix is shown in Table 5.

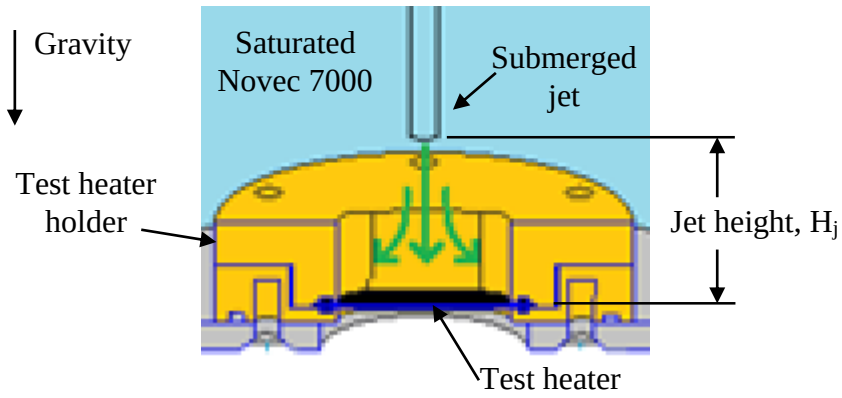

Figure 15**: Cross-section of the test conditions. The jet was submerged, 13.5 mm long, 2 mm in diameter, and at saturated conditions for all four experiments. The jet height varied from 3.3 mm to 7.4 mm.**

Table 5: Test conditions for each experiment.

	Jet flow rate [ml/min]		Jet Reynolds Number	Jet height, H_j [mm]
	[ml/min]	[g/s]		
Experiment 1	0	0	0	7.4
Experiment 2	88	2.05	2220	7.4
Experiment 3	0	0	0	3.3
Experiment 4	105	2.45	2653	3.3

The volumetric flow rate for experiments 2 and 4 is plotted for each IR measurement in Figure 16. Experiment 2's flow rate was relatively steady, while the flow rate for experiment 4 varied within 4% of the mean. The flow conditions were stable for each measurement.

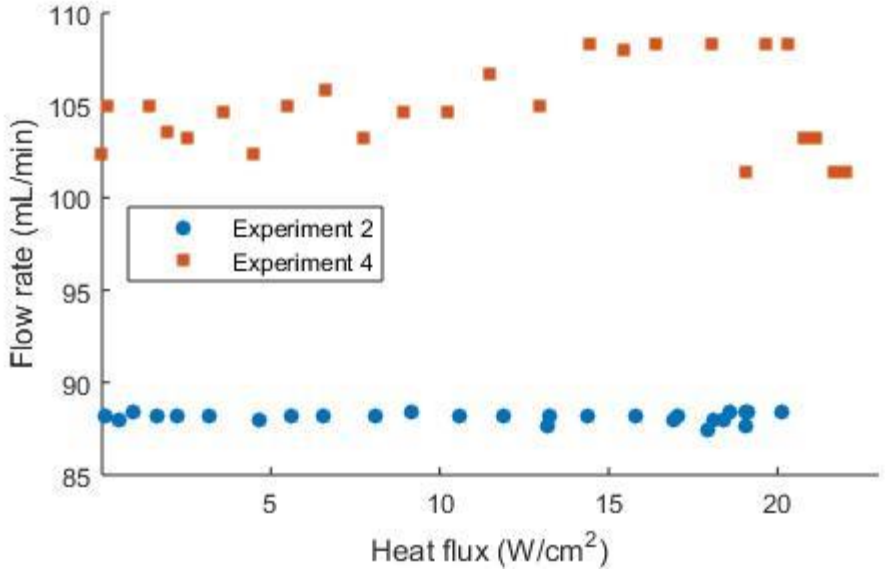

Figure 16: Jet flow rate for experiment 2 (far jet) and 4 (close jet).

The Novec 7000 was degassed before each experiment and the state of degassing was recorded. The state of degassing was quantified by the air mole fraction and mass concentration in the vapor space. The results are tabulated in Table 6.

Table 6: Degassing summary. The state of degassing was quantified by the air mole fraction and mass concentration in the vapor space.

	Initial air mole fraction	Initial air mass concentration (ppm)	Final air mole fraction	Final air mass concentration (ppm)
Experiment 1	0.021	3112	0.036	5300
Experiment 2	0.029	4259	0.036	5395
Experiment 3	0.027	4057	0.034	5085
Experiment 4	0.034	5100	0.040	6048

The pressure was allowed to increase near CHF for each experiment. Starting the chiller caused a sudden drop in pressure that initiated the transition to film boiling prematurely, so it was not used. The pressure is plotted in Figure 17.

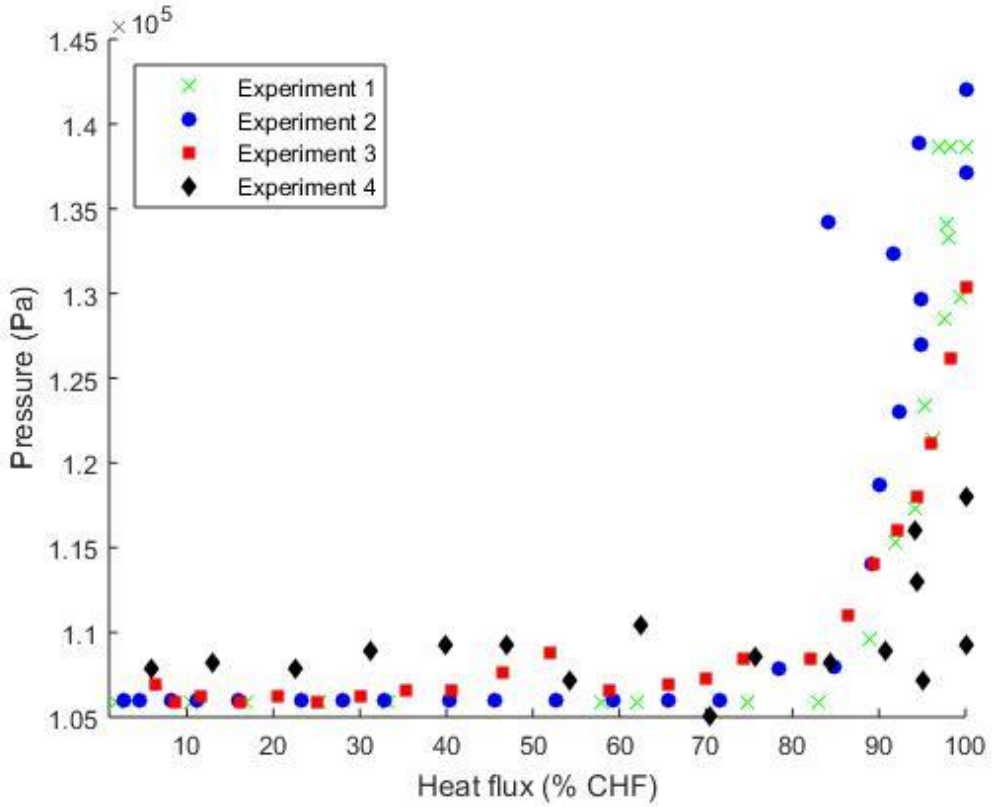

Figure 17: System pressure. The x-axis is the heat flux divided by the maximum heat flux and multiplied by 100. The system pressure was allowed to increase, because actuating the chiller caused a premature transition to film boiling.

Section 3.2: Post Processing

This section documents the post processing procedure. The unprocessed IR videos were used to evaluate the temperature, heat flux, wetted fraction, contact line characteristics, frequency of dryout events, average duration of dry time, and the dry patch size distribution. The parameters are defined in their respective subsection and in the **Glossary**. MATLAB was used to process all data.

Figure 18 shows the area of analysis for the experiments. The black lines are the black paint on the bottom of the test heater. Those pixels were used to calculate the temperature of the silicon and were otherwise ignored.

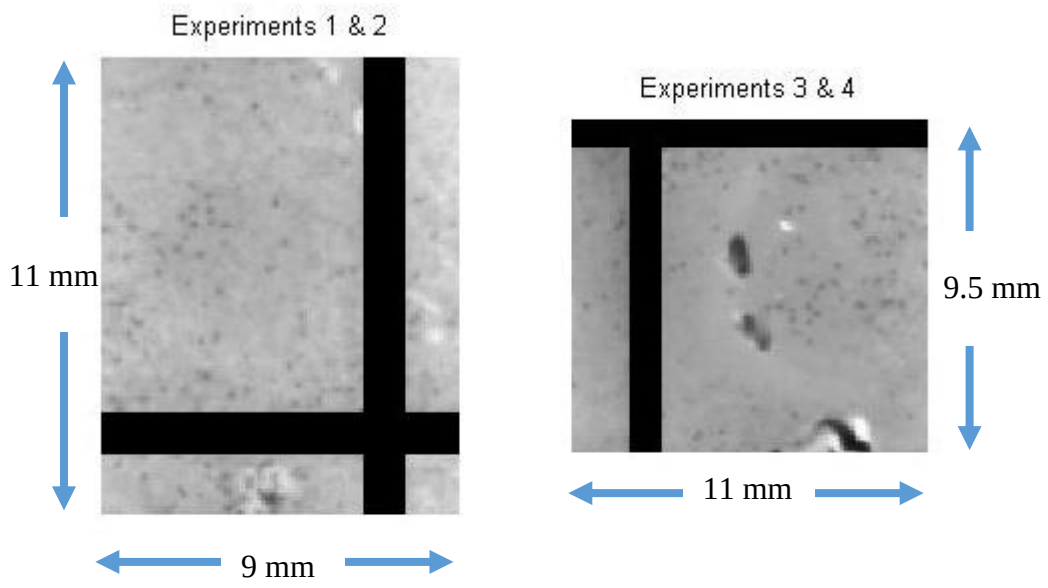

Figure 18: Experimental domain. The black lines are the black paint on the bottom of the test heater. They were used to calculate the silicon temperature and were otherwise ignored.

3.2.1 IR Thermometry

As discussed previously, the Altair software converted radiation to temperature by assuming the camera measured a black body. The test heater was not a black body, however, and the temperatures needed to be corrected. The IR thermography technique described in Kim et al. [20] was used and its application is summarized below.

The temperatures were corrected by evaluating the radiation contributions received by the camera. The black surface on the top of the heater (see Figure 5) is considered first. The camera received ambient radiation reflected by the test heater, radiation emitted by the silicon and Kapton tape, and radiation emitted by the black paint that was partially transmitted though the test heater. This is summarized by Equation 6, where E is blackbody radiation, σT^4. Each of the optical coefficients (ρ, ε,

τ) are cumulative values that include the absorption, emission, and multiple reflections within the test heater. See Kim et al. [20] for their derivation and definition. The optical coefficients were calculated with the optical properties in Table 2.

Equation 6

$$E_c = \rho_{\infty-c}E_\infty + \varepsilon_{si-c}E_{si} + \varepsilon_{T-c}E_T + \tau_{s-c}E_s$$

For the black paint on the bottom of the test heater, the camera received radiation that was emitted and reflected by the black paint, as expressed in Equation 7.

Equation 7

$$E_c = \rho_{\infty,s}E_\infty + \varepsilon_s E_s$$

The silicon and Kapton temperature profiles were needed at every frame (time-step) to calculate their radiation contribution in Equation 6. The silicon was assumed to be the same temperature as the black paint on the bottom surface and, based on its low thermal resistance, a constant temperature in the z-direction (see Figure 5). The temperatures over the entire silicon surface were solved for at every time-step by using the 2-D steady heat equation to interpolate the data at the black paint (Equation 8). The boundaries of the silicon were treated as adiabatic and the center line pixels of the black paint were used as boundary conditions, based on the camera smearing discussion in **3.1.4 Instrumentation and Data Acquisition**. The numerical problem is shown in Figure 19 and had good accuracy due to the high thermally conductivity of the silicon.

Equation 8

$$\frac{\partial^2 T}{\partial x^2} + \frac{\partial^2 T}{\partial y^2} = 0$$

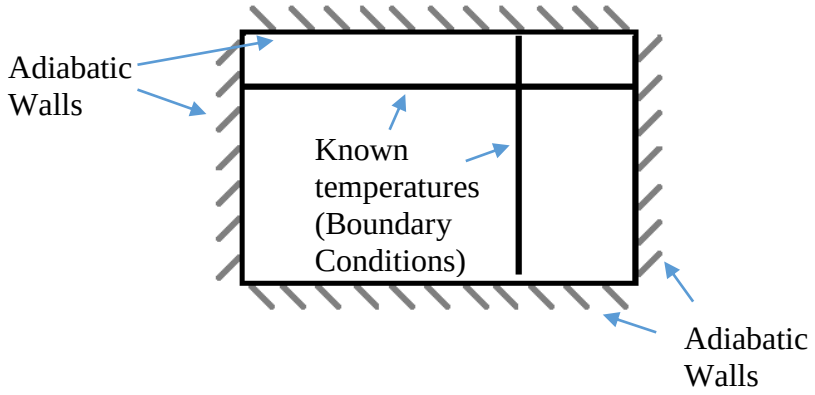

Figure 19: Numerical problem used for the calculation of the silicon temperature distribution.

The transient heat equation was used to calculate the temperature profile within the Kapton tape for every time-step. Most of the heat transfer was in the z-direction, so only the 1-D heat equation was used (see Equation 9). The boundary conditions were the temperatures of the silicon and top surface, which were obtained from the radiation equations. As a result, the equations were coupled and were solved simultaneously using the algorithm shown in Figure 20. The error from guessing an initial profile decayed completely within 0.1 seconds.

Equation 9

$$\frac{\partial T}{\partial t} = \alpha_T \frac{\partial T}{\partial z}$$

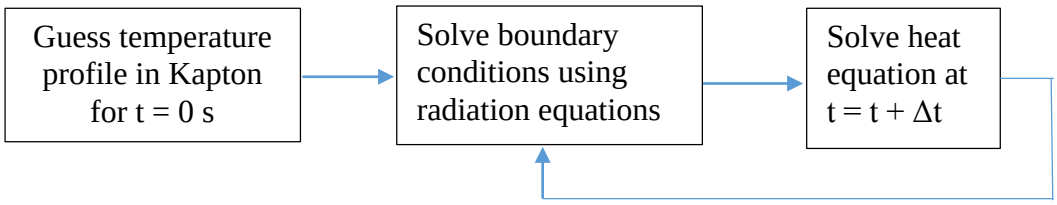

Figure 20: Algorithm used to solve the coupled radiation (Equation 6 and Equation 7) and heat (Equation 9) equations.

3.2.2 Temperature and Heat Transfer Calculations

The **3.2.1 IR Thermometry** section provided the framework for obtaining accurate spatially and temporally resolved temperature data. However, the use of multiple integration times (ITs) and the ambient temperature condition have not been addressed.

An IR video was obtained for each IT and their frames were offset (in seconds) by the camera frame rate. In the ideal case, the videos measured the temperature at the same time. However, the contact line may have moved by a few pixels during the offset. An algorithm was derived to address this problem and combine the IT videos into one data set. There were two important facts used for the derivation:

1. Each IT had a temperature range it was calibrated to accurately resolve.
2. ITs were adequate at resolving temperatures less than the minimum temperature of their calibration range.

The first part of the algorithm was to use the highest temperature range IT as the default data set, which was derived from the second fact. The temperature at each pixel was updated to the data from a lower IT if it was measured to be within that calibration range for all the integration time measurements. For example, consider the hypothetical case where two integration times were used. The first accurately

resolved temperatures at the wetted areas and the second accurately resolved temperatures at the dry areas. There are four cases for a given pixel:

1. It was wet in both frames, so the lower IT data was used.
2. It was wet in the first frame but dry in the second, so the higher IT data was used.
3. It was dry in the first frame but wet in the second. The lower IT was saturated, so the higher IT data was used.
4. It was dry in both frames, so the higher IT data was used.

Case 2 and 4 are the result of the higher IT's definition as the default data set. That is, the measurements were "made" when the higher IT video recorded. Case 3 has compromised accuracy because the measured temperature was less than the minimum of the calibration range. This caused the advancing areas (defined as area that was wetted within the last time-step) to have a higher uncertainty in the heat transfer measurements, although the integration times were carefully selected to minimize this error (see the discussion in **3.1.4 Instrumentation and Data Acquisition**). The lower integration time was used in case 1, which was a majority of the surface, because it increased the accuracy of the measurement.

The radiation calculations (Equation 6 and Equation 7) required information about the ambient temperature. The first measurement (described in **3.1.5 Data Collection Procedure**) was when the test heater was the same temperature as the bulk fluid. This data was substituted into Equation 6 and Equation 7 and the local ambient temperature was evaluated for each experiment (where $E_\infty(x,y) = \sigma T_\infty^4(x,y)$). The raw data and results of the ambient temperature calculation for experiment 1 are shown in

Figure 21. The large cold spot is the reflection from the center of the camera. A cryocooler was used to cool the camera core so that it was more sensitive to IR radiation. Once the ambient condition was known, the algorithms in **3.2.1 IR Thermometry** were used to obtain spatially and temporally resolved temperature data.

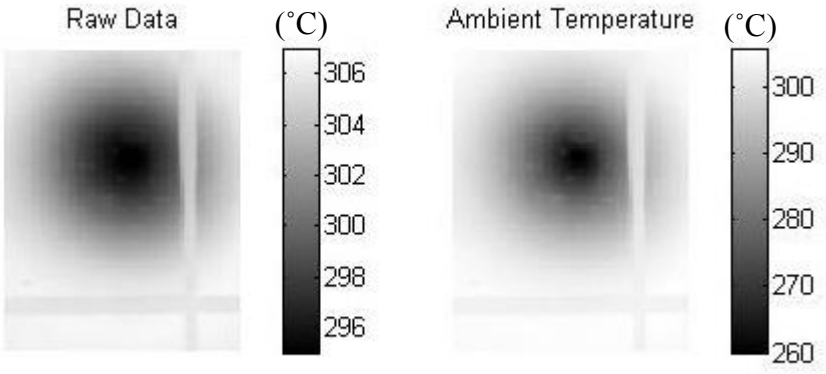

Figure 21: Ambient temperature calculation for experiment 1. This data was used for the radiation calculations (Equation 6 and Equation 7). The cold spot is the reflection from the center of the camera.

The 38 μm thick Kapton tape was discretized into 41 layers for the numerical transient heat equation calculation. The two nodes closest to the boiling surface were used to numerically calculate the heat transfer into the fluid (Equation 10). The thermal conductivity of the tape was used because the black paint was assumed to have zero thermal resistance.

Equation 10

$$q" = -k_T \frac{T_{Top\ node} - T_{Second\ node}}{\Delta z}$$

3.2.3 Wetted Fraction

The wetted fraction (WF) is the fraction of the surface that was covered by liquid. The heat transfer for each IR video was scaled from zero to one and used to determine if a pixel was wet or dry. If the heat transfer at a pixel was below some threshold, usually 0.48, it was classified as a dry spot.

The data was stored as binary maps for each frame, where 1's were dry spots and 0's were wet spots. This data was used to calculate the area of each dry patch and the wetted fraction, which was calculated for each frame and for each movie by dividing the number of wetted pixels by the total number of pixels. An example of this data is shown in Figure 22.

There were imperfections in the silicon that were approximately two pixels in size that would occasionally register as dry spots erroneously. The imperfections were probably a result of the doping process. To avoid this problem, dry spots of two pixels or less and dry spots of 5 pixels or less that remain unchanged for two frames were reclassified as wet.

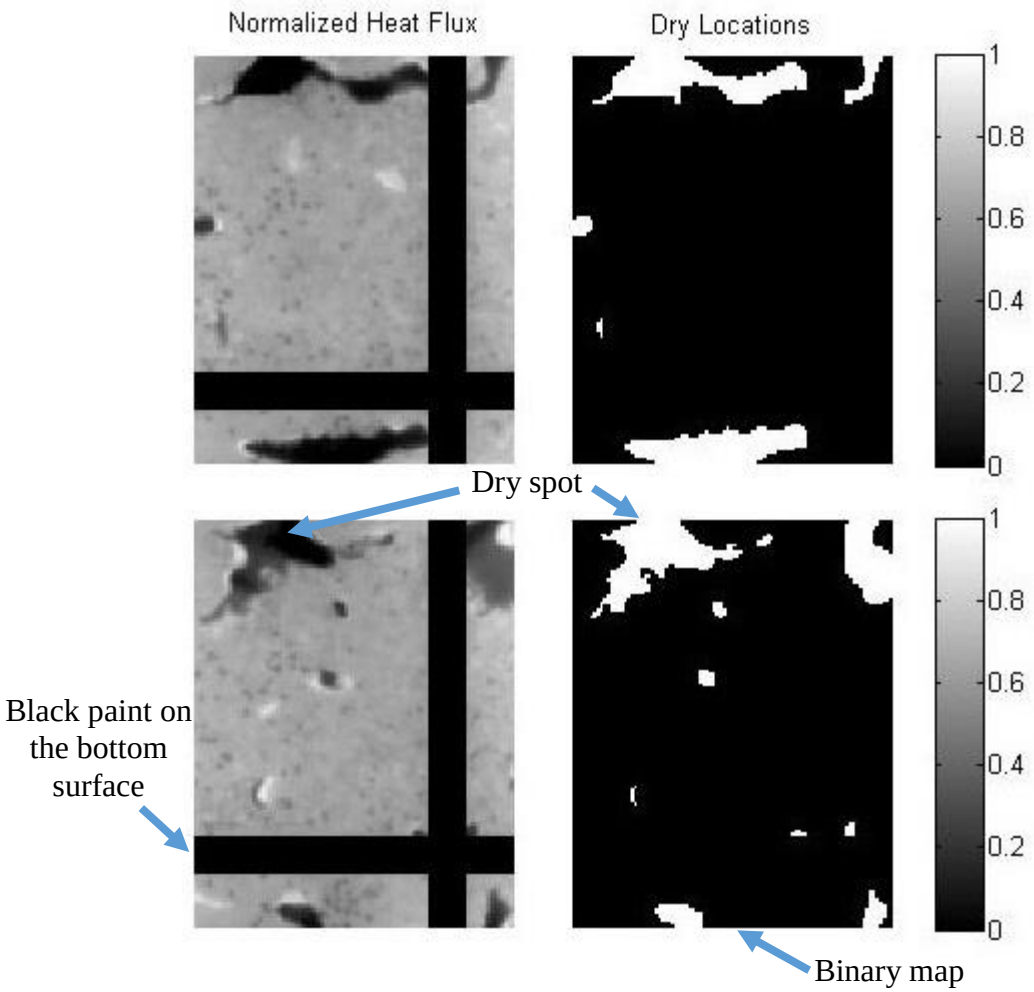

Figure 22: Wetted Fraction demonstration. The left plots are the normalized heat flux. A pixel was classified as dry if the heat flux was below a threshold. The right images show the binary map for the wet and dry spots. The white locations are dry spots.

3.2.4 Contact Line

The triple phase contact line, or just contact line, is the boundary between the liquid, vapor, and solid boiling surface. Only average temperatures were resolved at the contact line. The binary map from the **3.2.3 Wetted Fraction** section was used to identify the contact line. A pixel was labeled as a contact point if it was wet (0) and it neighbored a dry spot (1).

The contact line length is the length (in millimeters) of the contact line and was calculated by counting the number of pixels on the contact line and dividing by

the spatial resolution (pixels per millimeter). This information was resolved for each individual dry spot and the total length per frame. The contact line density (CLD) is the total contact line length in a given frame divided by the total area. A sample of the contact line is shown in Figure 23. The figure shows that the dry spots were assumed to end at the black paint on the bottom surface. All experiments were subjected to this error, and it is believed that it does not change the relative behavior.

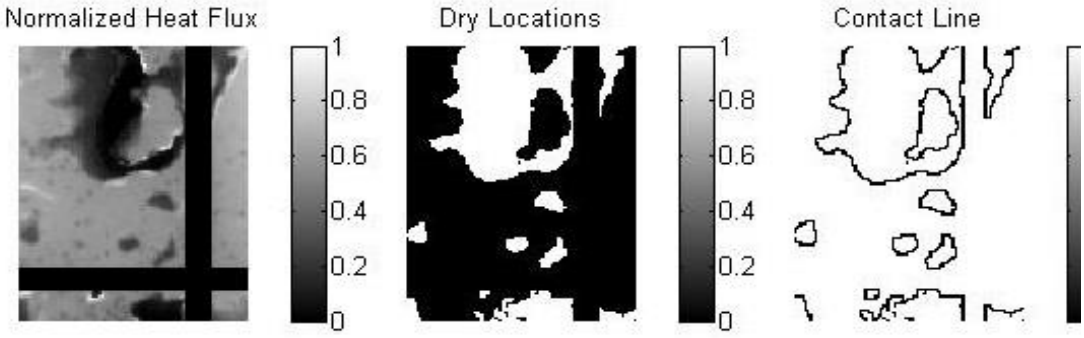

Figure 23: Contact line demonstration. The normalized heat flux (left image) was used to generate the map of the dry locations (middle image). A pixel was defined as part of the contact line (right image) if it was wet (0) and it neighbored a dry spot (1).

3.2.5 Advancing and Receding Area

The advancing area is the area that was vapor (dry) in the previous frame but is wet in the present frame. The receding area is the area that was wet in the previous frame but is dry in the present frame. This analysis was conducted by using the binary map of the wetted area. Advancing and receding areas were mapped for each frame and the area of each dry spot was stored. The area was calculated by counting the number of cells in each dry spot and dividing by the pixel per area conversion. An example of the advancing and receding areas is shown in Figure 24.

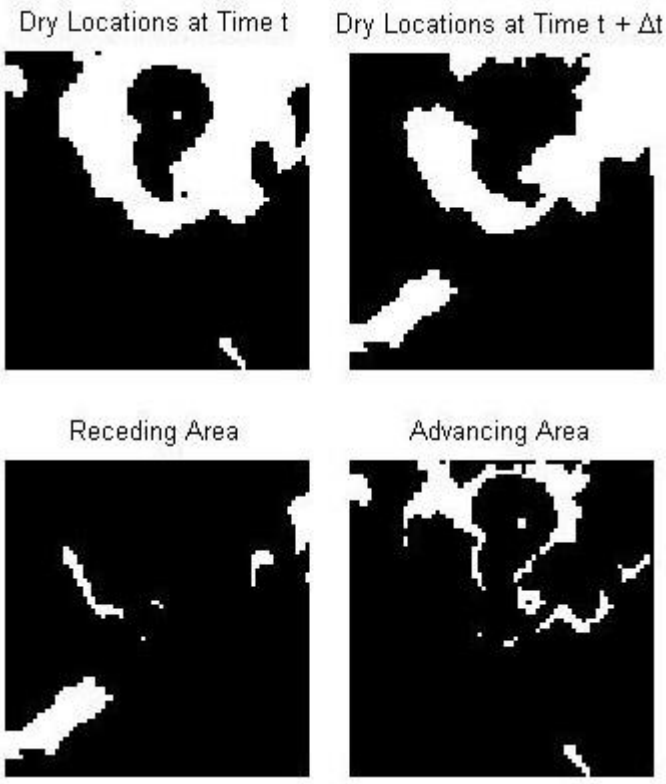

Figure 24: Advancing and receding area demonstration. Dry, advancing, and receding areas are white.

3.2.6 Contact Line Speed

The contact line speed is the speed (mm/s) that the contact line moves at each advancing and receding area. This was calculated by the area-based technique formulated by Jung et al. [23]. The contact line speed is defined in Equation 11 and an example is shown in Figure 25. The sum of L_1 and L_2 is equal to the contact line length of the receding area, which was obtained by the methods described in the previous subsections.

Equation 11

$$v = \frac{A}{\frac{1}{2}(L_1 + L_2)\Delta t}$$

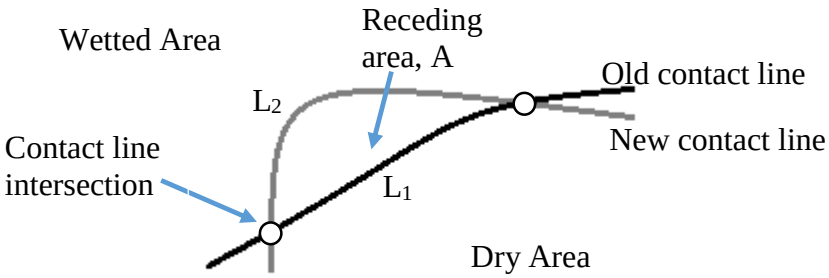

Figure 25: Contact line speed diagram. The contact line speed was calculated by dividing the advancing or receding area, A, by one half of the area's contact line length and the time-step.

3.2.7 Dryout Frequency and Average Duration of Dry Time

The dryout frequency is the frequency a dryout event occurs at an average pixel. This was calculated by dividing the number of times the pixels transition from wet (0) to dry (1) by the product of the number of frames, the time-step, and the number of pixels.

The average duration of dry time is the average duration of a dryout event at an average pixel. This is calculated by multiplying the number of frames the pixels are dry (1) by the time-step and dividing by the number of times the pixels transition from wet (0) to dry (1).

Section 3.3: Validation

Two validations were conducted to build confidence in the accuracy of the temperature and heat transfer measurements. The first validation used two gold mirrors to measure the temperature on both sides of the test heater when it was exposed to an air jet. The second was an energy balance that compared the heat flux measured during boiling to the amount of power input from the power supply.

The equation based post processing parameters, such as the contact line speed, dry spot frequency, etc., were verified using hand calculations for a small sample. The other parameters were verified by visual inspection.

3.3.1 Air Jet Validation

The test heater was arranged in the geometry shown in Figure 26. Two gold plated mirrors were used to measure the test heater temperature. The radiation from the bottom mirror was the same data that would be obtained during a boiling experiment and the top mirror enabled a direct measurement of the top surface.

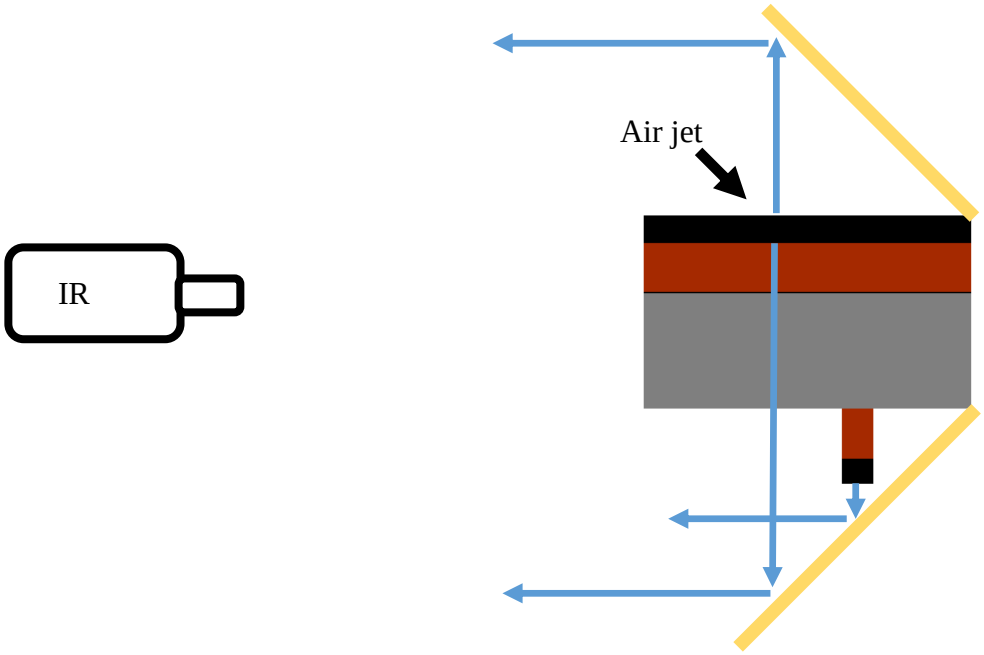

Figure 26: Air jet validation geometry. Two gold mirrors were used to obtain IR measurements of the test heater.

For the validation, the test heater was heated to a steady temperature of 77 °C, briefly subjected to a jet of compressed air, and then allowed to reheat. The IR measurement was then processed with the IR thermometry technique, where the direct measurement of the top surface was processed using Equation 7. The direct measurement of the top surface and the measurement through the test heater should have returned the same value after post processing. The average difference between the two measurements was 0.48 °C and the results are plotted in Figure 27.

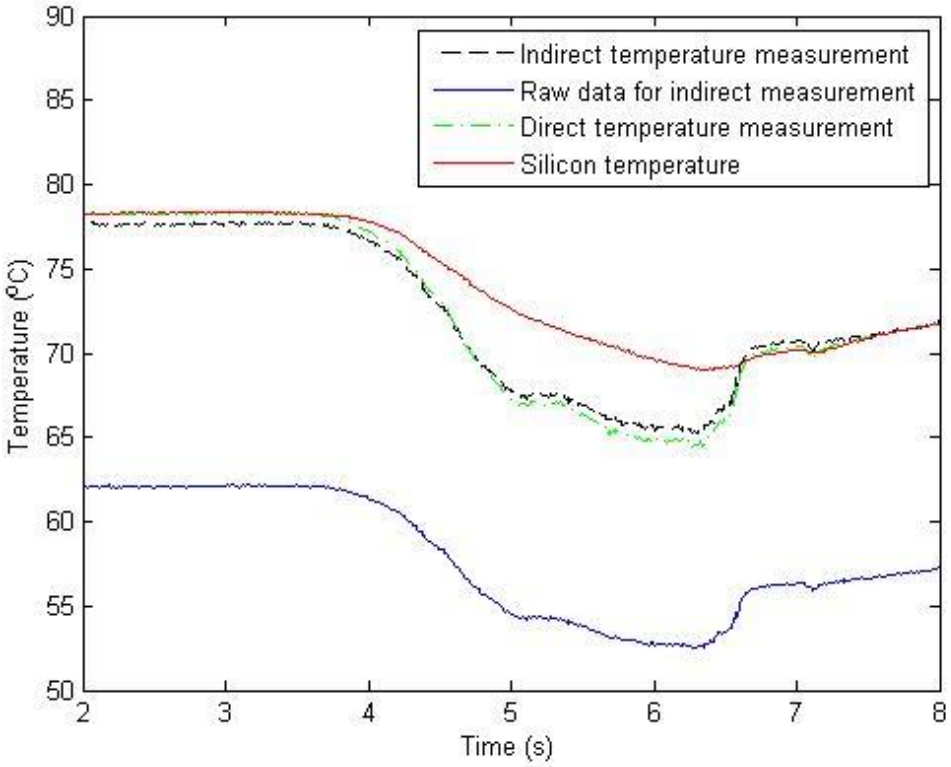

Figure 27: Jet validation results. The "Indirect temperature measurement" is the post processed top surface temperature obtained from the bottom mirror. "Raw data for indirect measurement" is the raw temperature measurement of the top surface from the bottom mirror. "Direct temperature measurement" is the post processed temperature measured from the top mirror. Finally, Silicon temperature is the post processed temperature measurement from the black paint on the bottom surface.

3.3.2 Energy Balance Validation

The power supply voltage and current was divided by an effective heat transfer area of 5.7 cm^2 to estimate the expected heat flux for each IR measurement. This estimate was compared to the heat fluxes calculated with the IR thermometry technique. The results for experiment 1 (pool boiling) and 2 (far jet) are shown in Figure 28.

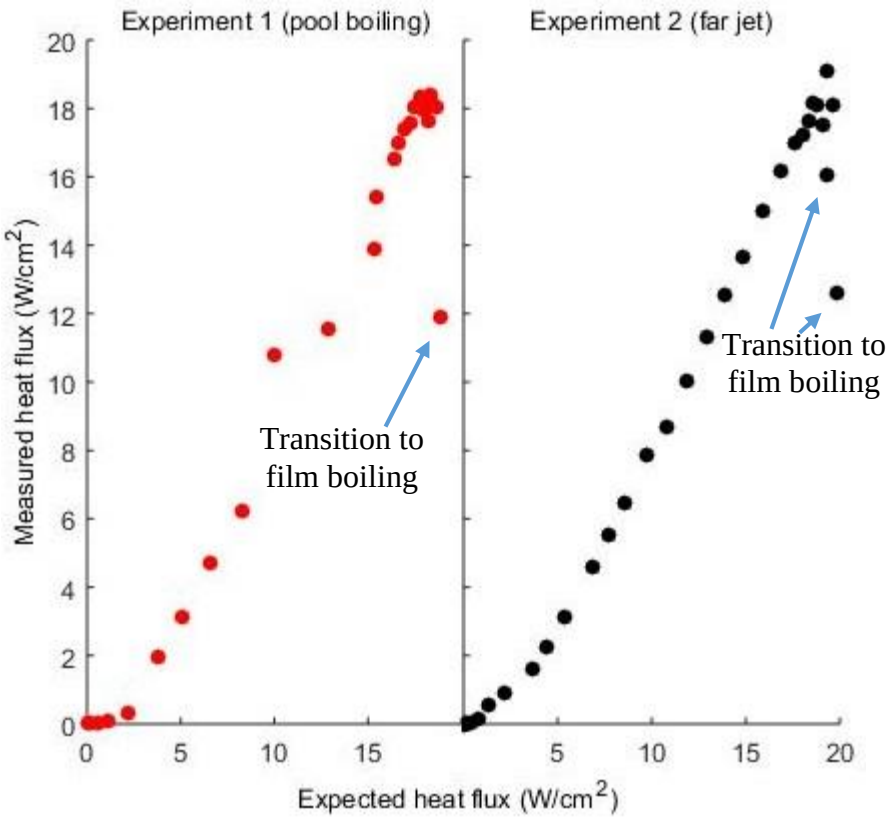

Figure 28: Energy balance validation. The expected heat flux was calculated by multiplying the power supply voltage and current by the estimated heat transfer area for each IR measurement. The measured heat flux was obtained using the IR thermometry technique.

The transition to film boiling measurements were significantly less than the expected value for two reasons. First, the current measurement from the power supply was not accurate. The current was manually recorded at the beginning of the measurement and the transition to film boiling caused it to decrease significantly due to the increase in surface temperature and electrical resistance. Second, the pixels saturated after the surface transitioned to film boiling and the temperatures were not accurately resolved.

This validation was not as rigorous as the jet validation. Although a reasonable first order guess, the effective heat transfer area is effectively a curve

fitting parameter and should vary with heat flux. This may explain the non-linear behavior in Figure 28.

Section 3.4: Experimental Uncertainty

The heat flux measurement (Equation 10) was sensitive to the uncertainty of the properties listed in Table 2, except the Kapton thermal diffusivity, and the IR camera temperature uncertainty. The reflectivity and emissivity of the black paint must sum to one, so only the emissivity was considered. It was assumed that all the uncertainties were independent and the propagation of uncertainties was used (Equation 12) to determine the uncertainty in heat flux.

Equation 12

$$\partial q" = \sqrt{[(\frac{\partial q"}{\partial T})^2 \partial T^2 + (\frac{\partial q"}{\partial k_T})^2 \partial k_T^2 + (\frac{\partial q"}{\partial \varepsilon_s})^2 \partial \varepsilon_s^2 + (\frac{\partial q"}{\partial \alpha_T})^2 \partial \alpha_T^2 + (\frac{\partial q"}{\partial \alpha_{si}})^2 \partial \alpha_{si}^2 + (\frac{\partial q"}{\partial \rho_{\infty-si}})^2 \partial \rho_{\infty-si}^2 + (\frac{\partial q"}{\partial \rho_{si-T}})^2 \partial \rho_{si-T}^2]}$$

The analysis was conducted by perturbing the variables of Equation 12 in the post processing code and calculating the heat flux. The temperature perturbation was implemented by increasing the silicon temperature by the camera uncertainty, 1 °C. This resulted in a conservative estimate of the sensitivity, because the camera uncertainty would tend to average out over all the pixels. The sensitivity of heat flux to each variable was calculated numerically by Equation 13. The results are summarized in Table 7. The thermal conductivity was the largest contributor to the uncertainty and the temperature uncertainty was the smallest, which gives additional justification to the careful us of only one integration time.

Equation 13

$$\frac{\partial q"}{\partial x_{var}} = \frac{q"_{measured} - q"_{perturbed}}{\delta x_{var}}$$

Table 7: Heat flux uncertainty analysis.

$q"_{measured}$ (W/m^2)	4.8	11.0	15.6	18.8
Property (x_{var})	$\left\|\frac{\partial q"}{\partial x_{var}}\right\|$	$\left\|\frac{\partial q"}{\partial x_{var}}\right\|$	$\left\|\frac{\partial q"}{\partial x_{var}}\right\|$	$\left\|\frac{\partial q"}{\partial x_{var}}\right\|$
T (°C)	0.268	0.11	0.12	0.06
k_T (W/mK)	34	91	130	157
ε_s	5	7	29	19
α_T (m^{-1})	0.00013	0.00034	0.00072	0.0005
α_{si} (m^{-1})	2	5.4	7.2	9
$\rho_{\infty\text{-si}}$	21.25	46.25	80	76.25
$\rho_{si\text{-}T}$	21	61.7	93.3	83.3
Uncertainty (W/m^2)	0.50	1.09	1.70	1.87

Chapter 4: Results

The surface average and local results are discussed in this section. The local results were evaluated with respect to radial distance from the jet.

Section 4.1: Full Area Investigation

4.1.1 Boiling Regimes

The boiling curves for all experiments are shown in Figure 29. The wall temperature was defined as the average wetted (liquid area) temperature for the following reasons. First, the wetted temperature was the only temperature independent of the test heater configuration. The silicon was significantly hotter than the boiling surface due to the insulating Kapton tape, and its temperature increased with tape thickness. The temperature of dry patches was also a function of the Kapton thickness, because they superheated to the temperature of the silicon. Second, the average wetted temperature was a good estimate of the wall temperature in the case of zero tape thickness. The average silicon temperature would approach the wetted temperature, because the high thermal conductivity of the silicon would inhibit temperature increases at dry spots.

The wall superheat was defined as the independent variable. The true independent variable in these experiments was the power supply voltage. However, the input power was not constant because the silicon's electrical resistance was proportional to temperature. As a result, the power at a given voltage decreased as the wetted fraction decreased and the silicon temperature increased. This behavior caused the test heater to stabilize itself near CHF and early transition boiling regime data was

obtained. This regime cannot be achieved if the independent variable is the heat flux, so the wall superheat was believed to be more representative. In addition, CHF mechanisms were believed to be more sensitive to wall superheat because the dryout characteristic plots had less scatter when it was used as the independent variable.

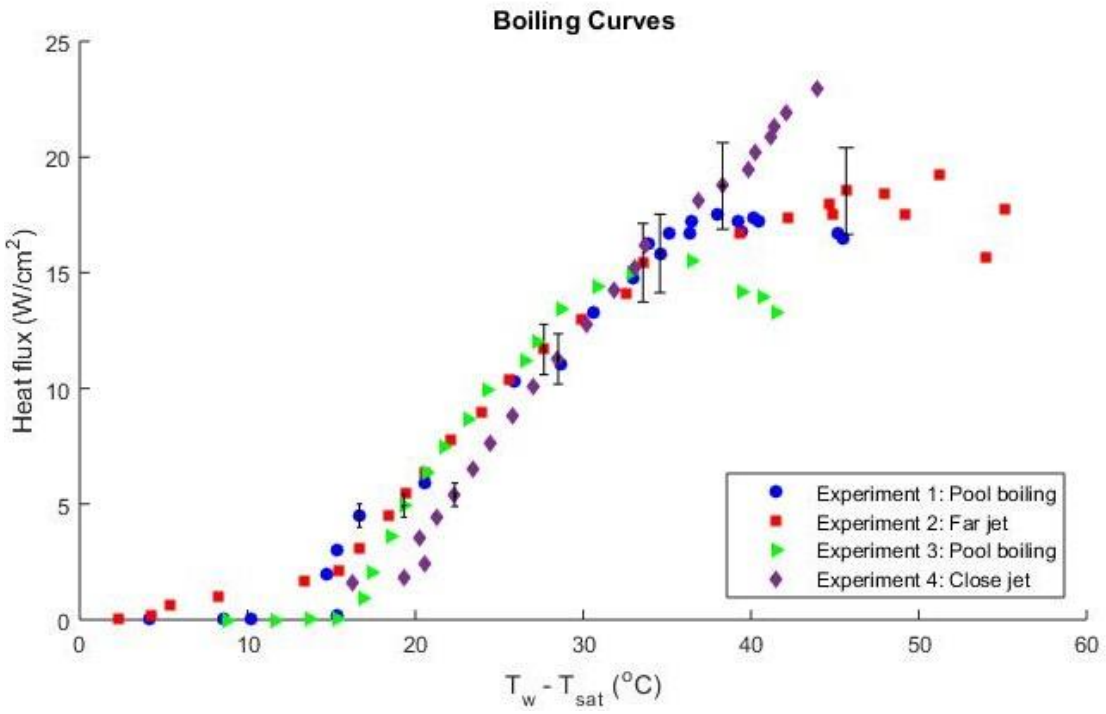

Figure 29: Boiling curves for experiment 1 and 3 (pool boiling), experiment 2 (88 ml/min jet elevated 7.4 mm above the test heater), and experiment 4 (105 ml/min jet elevated 3.3 mm above the test heater). Uncertainty bars are shown for representative heat fluxes.

4.1.1.1 Single Phase Heat Transfer

Experiments 2 and 4 both demonstrated much stronger single phase convection than the pool boiling cases. Sample post processed temperature (°C) data is shown in Figure 30. The top row is from experiment 1 (pool boiling) and shows waves of natural convection that were observed. The second row shows the jet from experiment 4 (close jet) impinging on the surface, which caused large variations in the surface temperature.

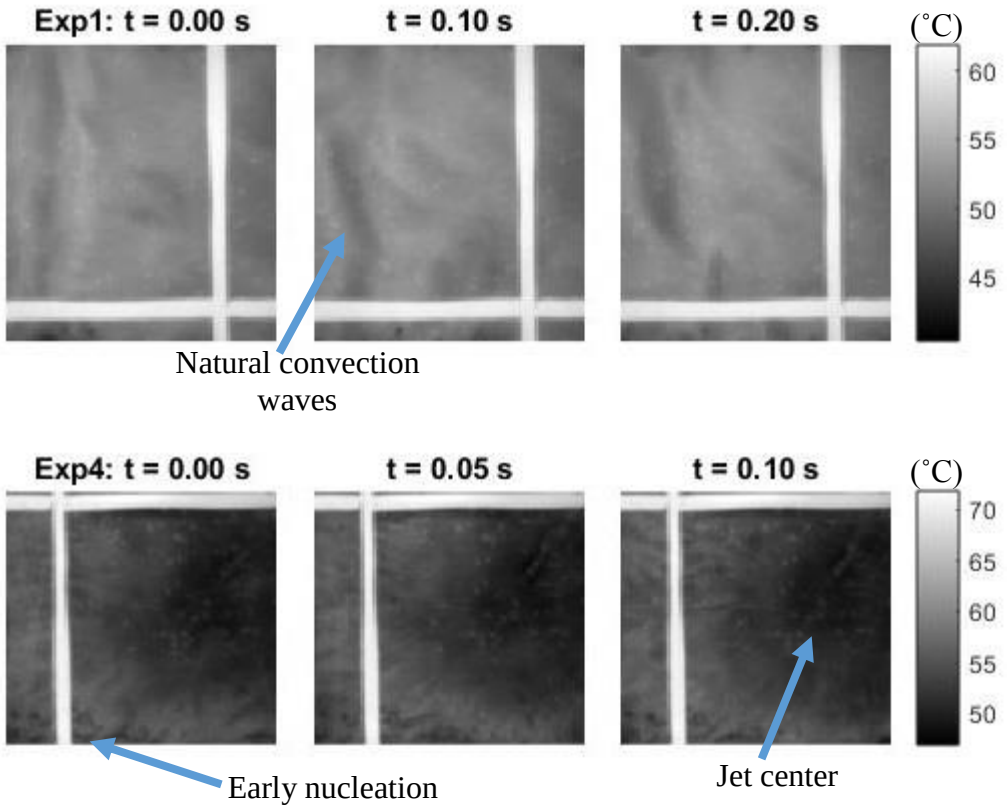

Figure 30: Temperature (ºC) data for experiments 1 (pool boiling) (top row) and 4 (close jet) (bottom row) before the onset of nucleation.

4.1.1.2 Isolated Bubble Nucleate Boiling Regime

Nucleate boiling was initiated when the wall superheat was between 15 and 20 °C. Generally, forced convection suppresses the thermal boundary layer and delays the onset of nucleate boiling to higher superheats. That was observed in experiment 4 (close jet), where the convection was much stronger, but not in experiment 2 (far jet). Temperature measurements from the early nucleate boiling regime are shown for experiments 1 (pool boiling) and 2 (far jet) in Figure 31. The images show the largest bubble spacing observed. For experiment 1, the onset of nucleation occurred for the entire surface on the order of tens of seconds and corresponded to a drop in wall

superheat and enhanced heat transfer. In experiment 2, the boundaries of the surface had higher wall superheats because they were farther from the jet center. These locations achieved nucleate boiling locally, while the center did not boil until the heat flux was increased. The bubbles became denser as the heat flux was increased, and eventually the surface appeared to be uniform temperature. Local dryout began after the bubbles were at their densest apparent packing.

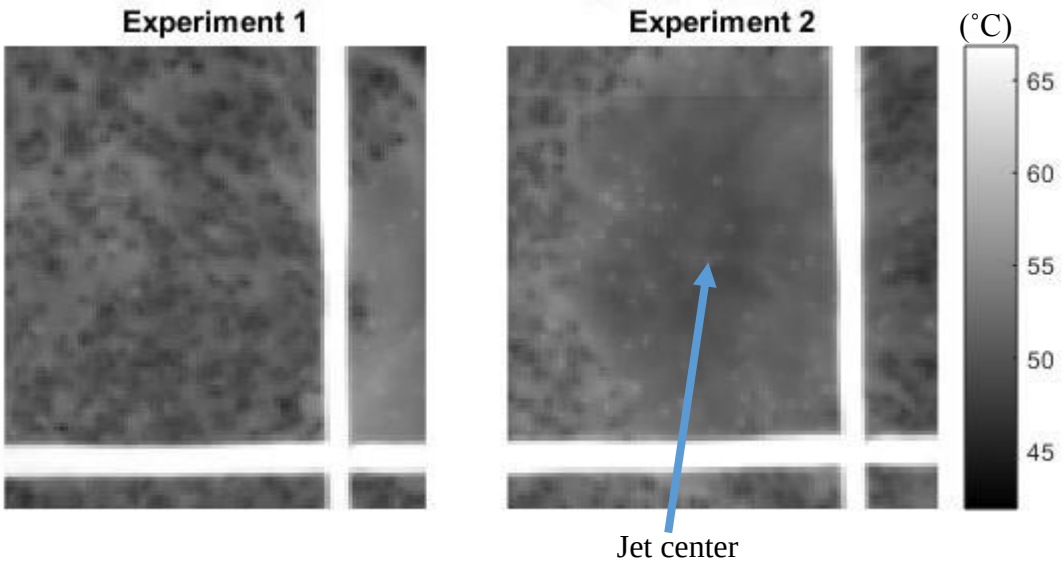

Figure 31: Temperature (ºC) data for experiment 1 (pool boiling) (left image) and experiment 2 (far jet) (right image) during early nucleate boiling. The low temperature points are nucleation sites.

The boiling curves generally coincided in the early nucleate boiling regime. This implies that the forced convection had little enhancement on the average heat transfer in this regime, and it is incorrect to treat the heat transfer as the superposition of the forced convection and nucleate boiling heat transfer. This treatment would imply that experiment 4 should have the lowest wall superheats during nucleate boiling. The high superheat observed may be due to the suppressed thermal boundary layer preventing optimal nucleation and departure heat transfer.

4.1.1.3 Slug and Column Nucleate Boiling and Early Transition Boiling

Experiment 1 (pool boiling) temperature and heat flux data near CHF is shown in Figure 32. The results were qualitatively the same for the other pool boiling case, experiment 3. It is unclear why CHF for experiment 1 (17.5 W/cm^2) was greater than experiment 3 (15.5 W/cm^2). The ¼" Swagelok fitting that held the jet nozzle was confined within the test heater walls (Figure 6) for experiment 3, but not experiment 1, and it is possible that the additional impedance to the liquid inflow triggered CHF prematurely. Differences in surface characteristics, nucleation site density, and the degree of degassing may have also contributed.

The images from Figure 32 show one frame samples of the boiling characteristics from select measurements and the general trend that the wetted fraction decreased as the wall superheat increased. Relatively small dry spots with very short lifetimes, fast contact line speeds, and moderate heat transfer were observed during all measurements after the onset of dryout. As the wall superheat was increased in the nucleate boiling regime, larger dry spots also formed that were characterized by long lifetimes, approximately zero heat transfer, high temperatures, and slow contact line speeds. Generally, the large dry spots at least partially rewetted and they migrated locally. It was observed that the probability of the dry spots rewetting decreased as their area increased.

The mechanism of heat transfer at the dry spots was not well understood. It is believed that liquid was entrained in dry patches as they formed, and the quality of the vapor space increased over their lifetime. Large dry spots formed when the

entrained liquid of incipient (generally small) dry spots boiled before they were rewetted, which resulted in superheating.

Figure 32 demonstrates enhanced heat transfer at parts of the dry spot boundaries, which was observed in all four experiments. These areas were recently rewetted (advancing areas) and the high heat transfer is due to the thermal storage within the tape from the superheated dry spot.

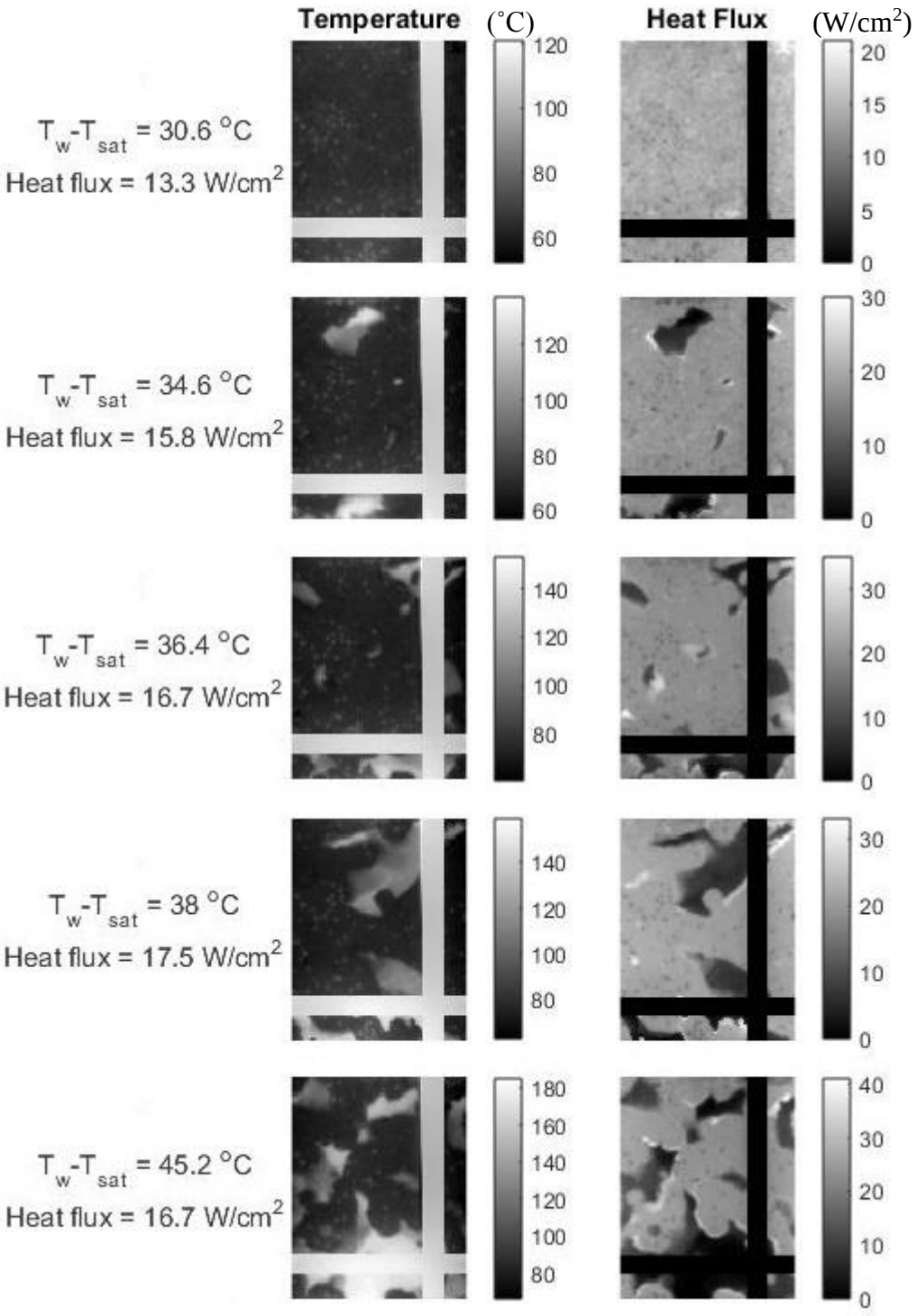

Figure 32: Slug and column nucleate boiling through transition boiling regimes for experiment 1 (pool boiling). The average wall superheat and heat flux on each row corresponds to the full IR measurement average, not the frame average.

Temperature and heat flux data near CHF from experiment 2 (far jet) and Experiment 4 (close jet) are shown in Figure 33 and Figure 34. CHF during experiment 2 was approximately 18.5 W/cm^2. Distinct local boiling regimes were observed during experiment 4 and CHF was only achieved locally. The maximum average measurement was 22.9 W/cm^2.

Similar pool boiling dry spot mechanics were observed during the impinging jet experiments. However, the distribution of dryout varied with radial distance from the jet. For example, large and small dry spots, as described above, were observed on the periphery of the jet during experiment 4, but not near the jet center. During experiment 2, only small, moderate heat transfer, and quickly rewetted dry spots were observed under the jet before CHF.

As shown in Figure 29, experiment 2 followed approximately the same boiling curve as the pool boiling experiments after the onset of nucleate boiling, except it reached higher superheats. This demonstrates that the jet did not enhance heat transfer, it only enabled rewetting and improved stability. Heat transfer enhancement was observed during experiment 4, where slope of the boiling curve did not decrease with the wetted fraction as it did in the other experiments. This observation is discussed in more detail in Section 4.2: Local Investigation

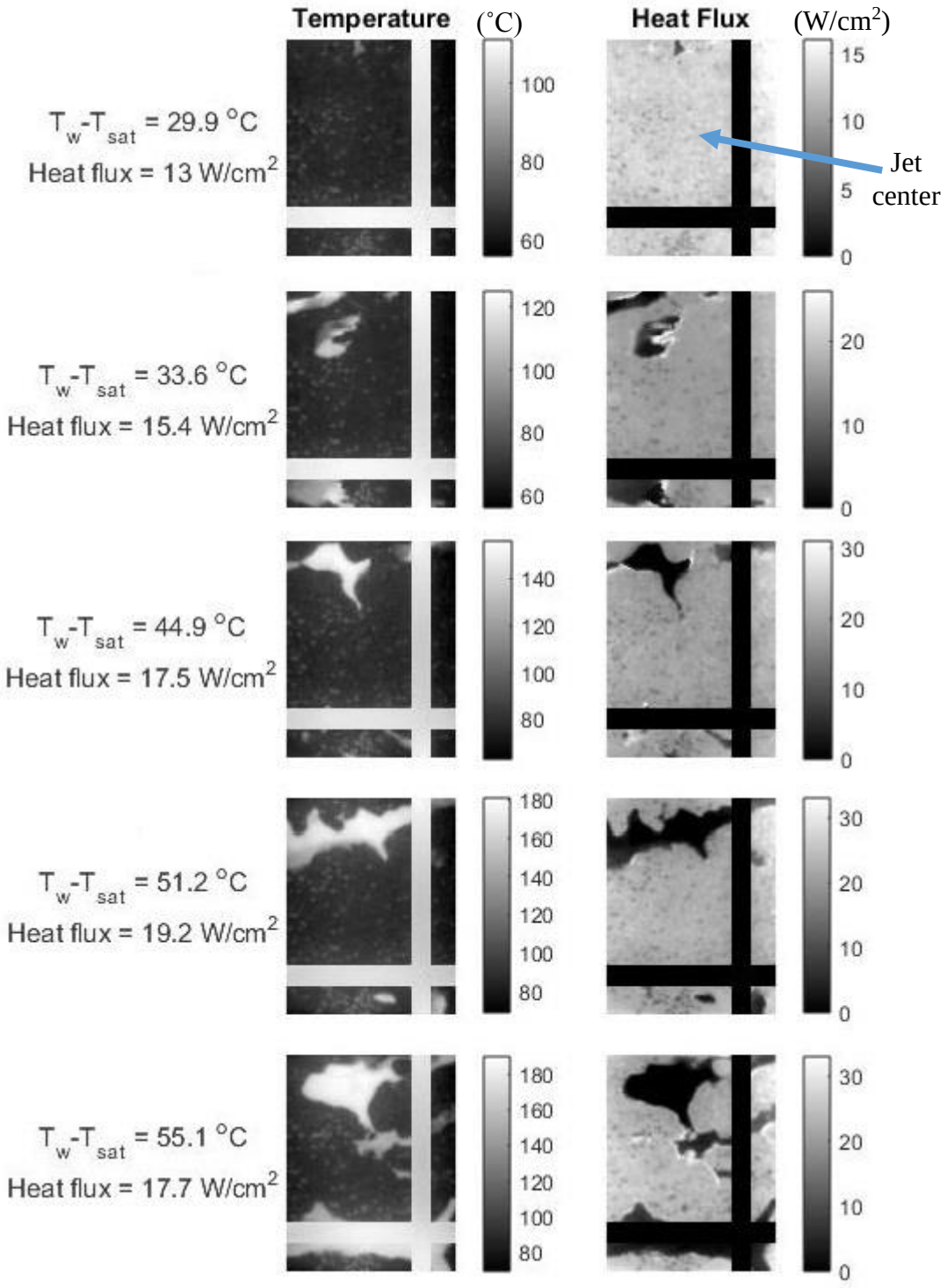

Figure 33: Slug and column nucleate boiling through transition boiling regimes for experiment 2 (far jet). The average wall superheat and heat flux on each row corresponds to the full IR measurement average, not the frame average.

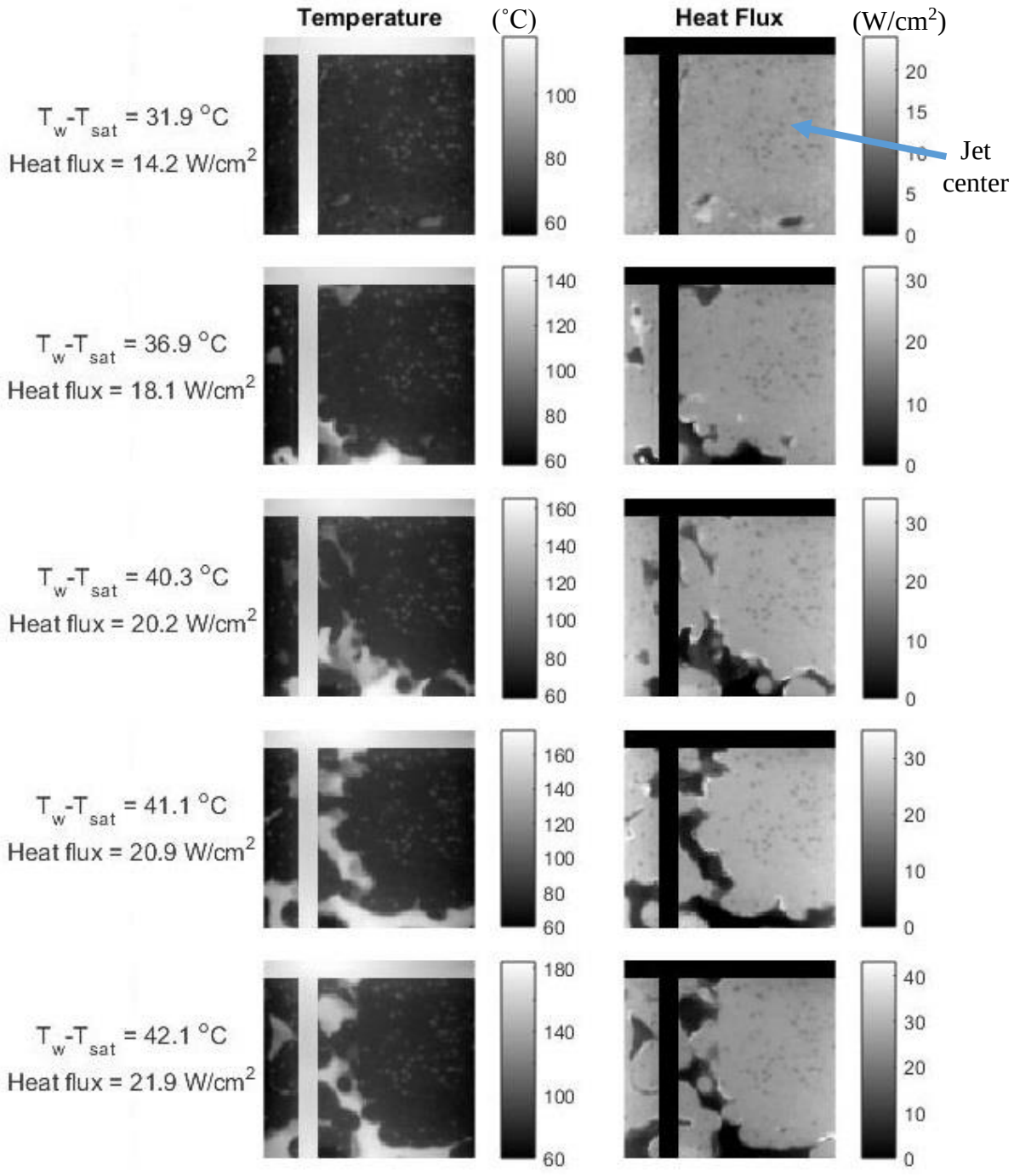

Figure 34: Near CHF boiling data for experiment 4 (close jet). The experiment had large spatial variations in boiling behavior, so a pool boiling regime label was not used. The average wall superheat and heat flux on each row corresponds to the full IR measurement average, not the frame average.

4.1.1.4: Transition to Film Boiling

The two pool boiling cases had similar behavior as they transitioned to film boiling. The transition, shown in Figure 35 for experiment 3, occurred as the interaction between the large dry spots and the wall temperature became unstable. The large superheated dry spots caused the local wall temperature to increase, which resulted in additional dryout and the expansion of the large dry spots. This interaction was stable at lower superheats because the surface could remove all of the generated heat.

Irreversible dry spots, defined as dry spots that do not rewet, have been observed to initiate film boiling [18]. Large dry spots that did not rewet were observed in these experiments, but it is not clear that their reversibility was significant. The rewetting of large dry spots appeared to be a probabilistic phenomenon based on the area and superheat of the dry spot. The dry patches during the transition to film boiling were only irreversible because they were present as the surface transitioned.

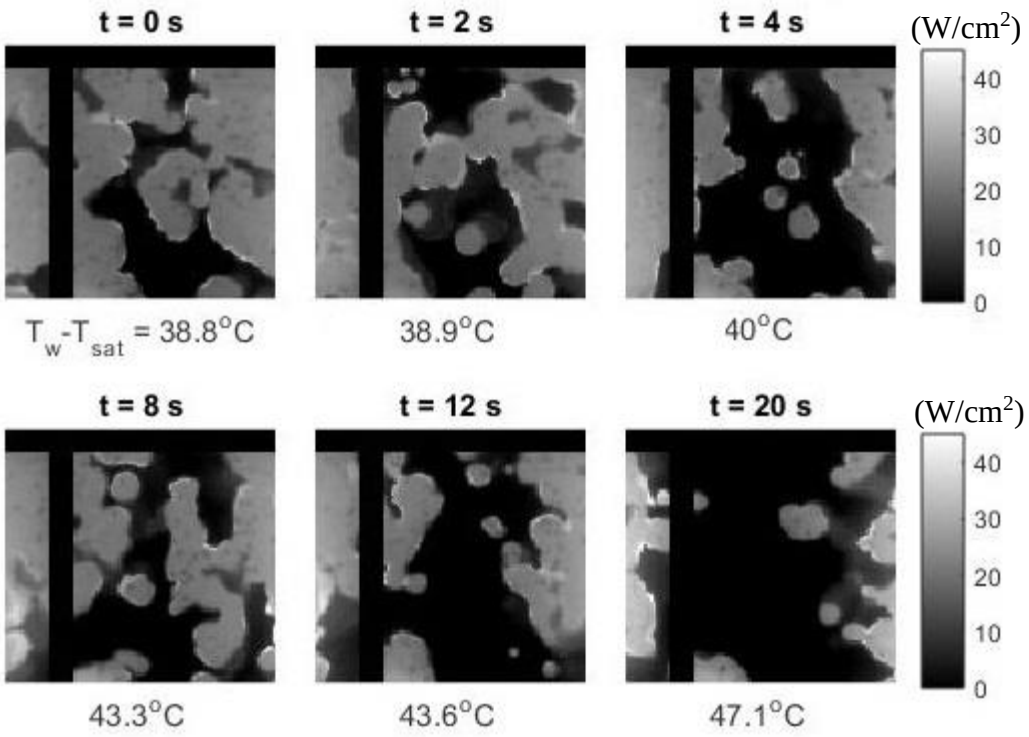

Figure 35: Experiment 3 (pool boiling) heat flux (W/cm^2) data during the transition to film boiling. The average heat flux before the transition was approximately 16.5 W/cm^2. The temperatures shown are the transient (frame average) wall superheats.

The experiment 2 (far jet) transition to film boiling is shown in Figure 36. The same transition mechanisms were observed as the pool boiling experiments. The transition took slightly longer in this experiment, because the jet rewetted locally and helped stabilize the system.

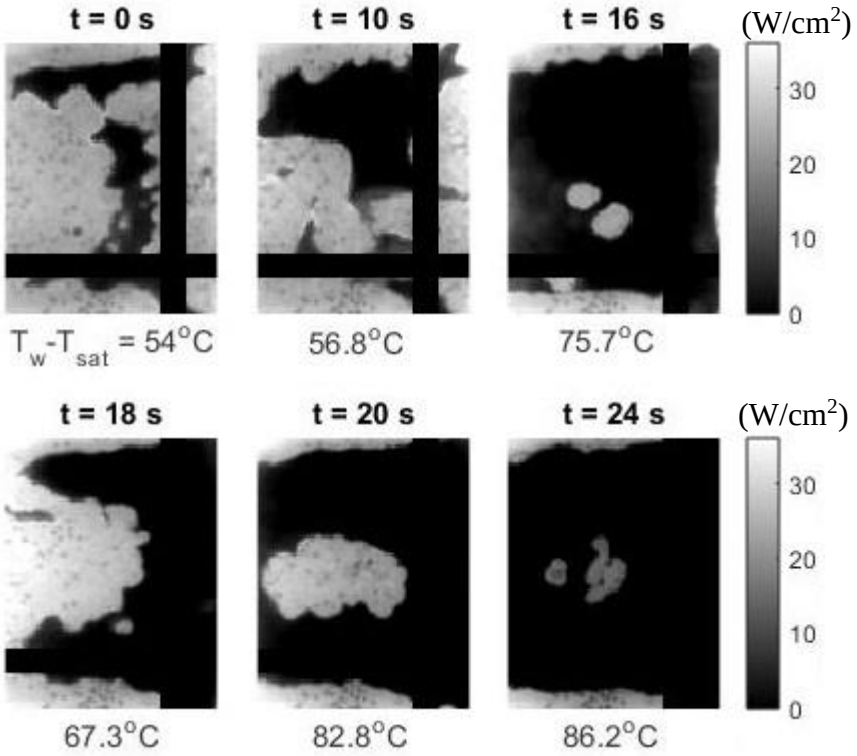

Figure 36: Experiment 2 (far jet) heat flux (W/cm^2) data for the film boiling transition. The average heat flux before the transition was approximately 17.7 W/cm^2. The temperatures shown are the transient (frame average) wall temperatures.

Experiment 4 (close jet) only achieved film boiling locally, as shown in Figure 37, and the same transition mechanisms were observed. The sides of the heater transitioned to film boiling in less than 17 seconds. There was high heat transfer on the right side of the surface that began around t = 12 seconds, and was probably a transient inflow of cold fluid from the side of the heater. A similar inflow occurred at t = 18 seconds in Figure 36 for experiment 2. Experiment 4 was observed for 40 seconds after the transition occurred and it did not develop further. The only transient behavior was small oscillations of the boundary between the nucleate boiling and film boiling regimes. The experiment was then concluded to avoid damage to the system from high temperatures.

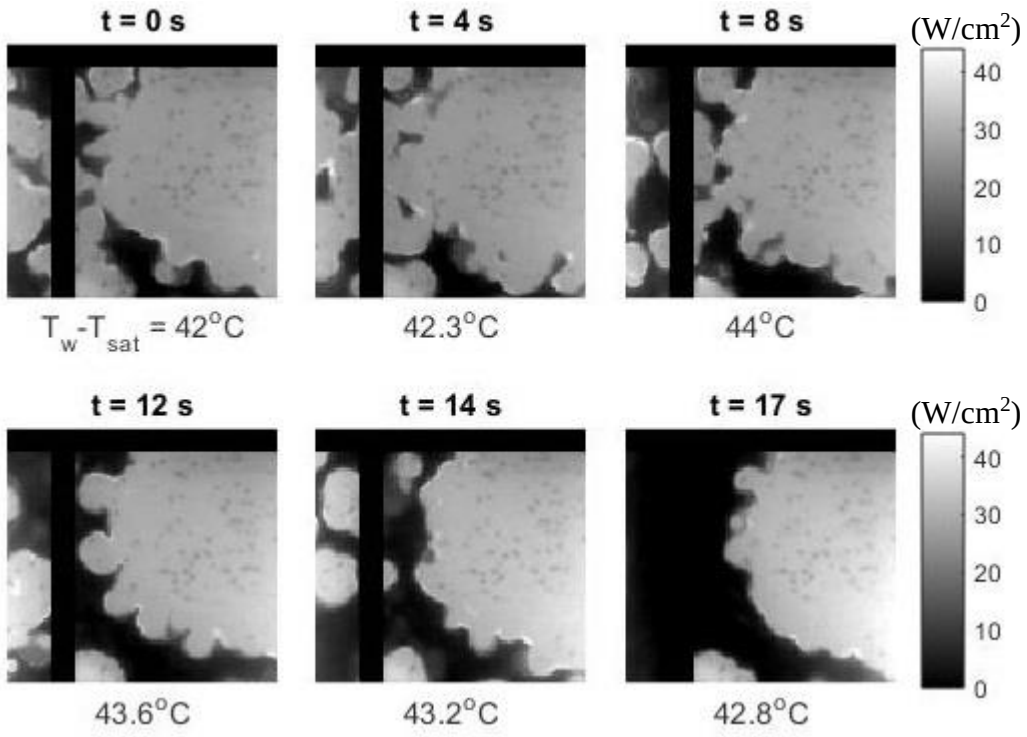

Figure 37: Experiment 4 (close jet) heat flux (W/cm^2) data for the local film boiling transition. The average heat flux before the transition was approximately 22.9 W/cm^2. The temperatures shown are the transient (frame average) wall temperatures.

4.1.2 Contact Line Density and Wetted Fraction

The previous subsection conducted qualitative analysis of IR data through the boiling curve. This subsection quantitatively investigates the wetted fraction, contact line density, temperature, and heat flux to support some of the previous discussion.

Figure 38 and Figure 39 show the WF and CLD evolution though the boiling curve for experiment 1 (pool boiling) and 4 (close jet). Both plots show that the contact line density slowly increased to its maximum at CHF and then rapidly declined during the transition to film boiling. Experiment 2 and 3 both demonstrated the same behavior.

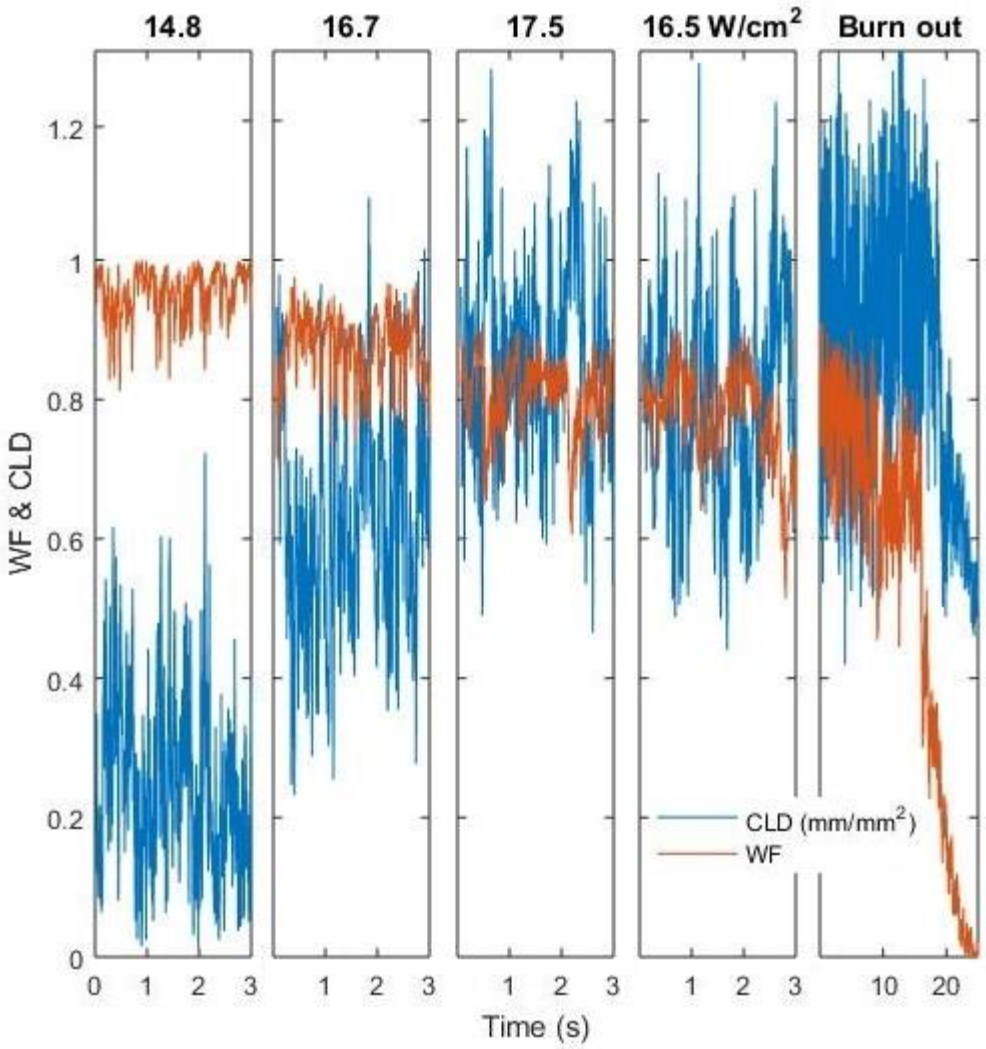

Figure 38: WF and CLD evolution with heat flux for experiment 1 (pool boiling). The plots have increasing wall superheat from left to right.

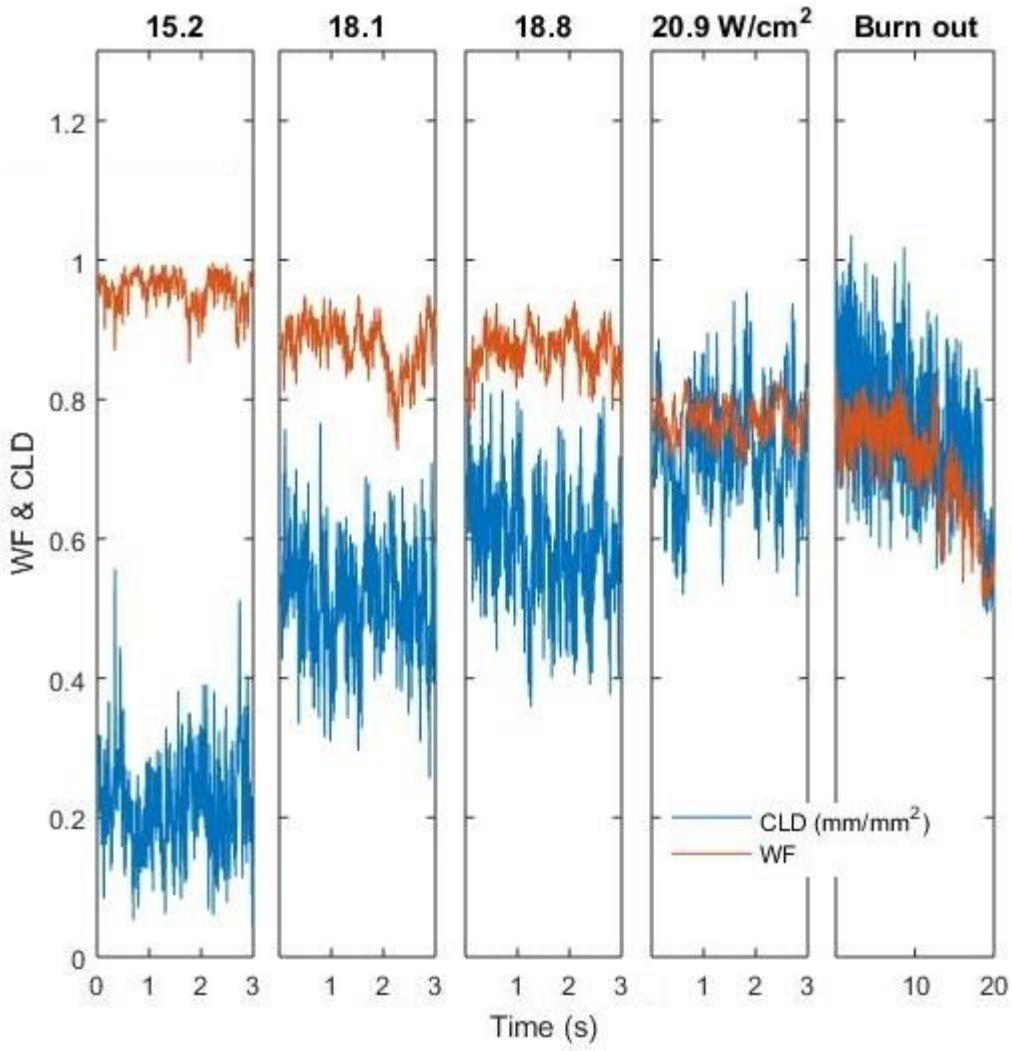

Figure 39: WF and CLD evolution with heat flux for experiment 4 (close jet). The plots have increasing wall superheat from left to right.

Transient CLD, WF, frame average surface temperature, and frame average heat flux plots are shown in Figure 40 and Figure 41 for experiment 1 (pool boiling) and 2 (far jet) near CHF. The plots show that for a given input power, transient increases in the WF caused increases in the heat flux. Therefore, the decreased average WF with increased wall superheat shown in Figure 38 and Figure 39 was a necessary condition, but not the mechanism that enhanced heat transfer. Instead, the

increased wetted area heat transfer compensated for the decreased wetted fraction, which caused the average heat flux to increase until CHF.

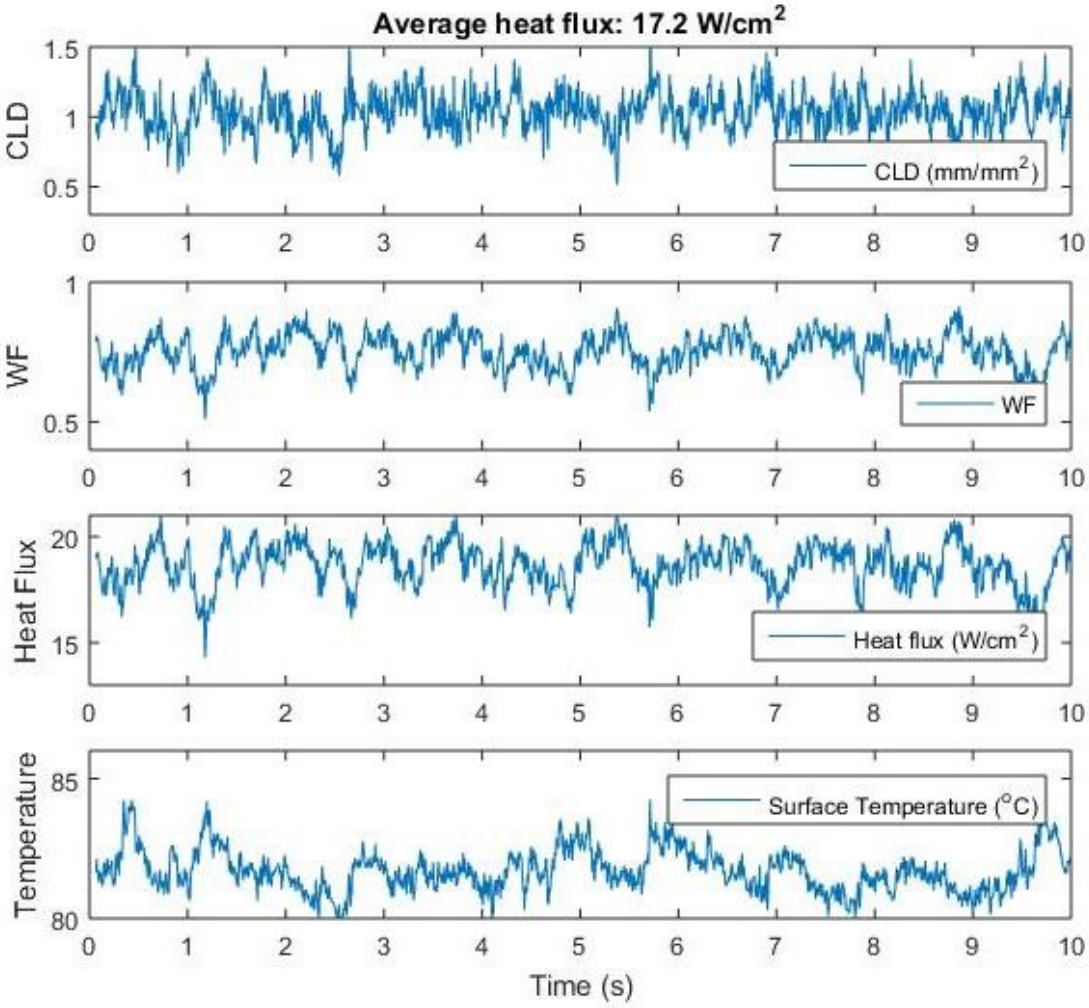

Figure 40: Experiment 1 (pool boiling) transient temperature, heat flux, wetted fraction (WF) and contact line density (CLD) data.

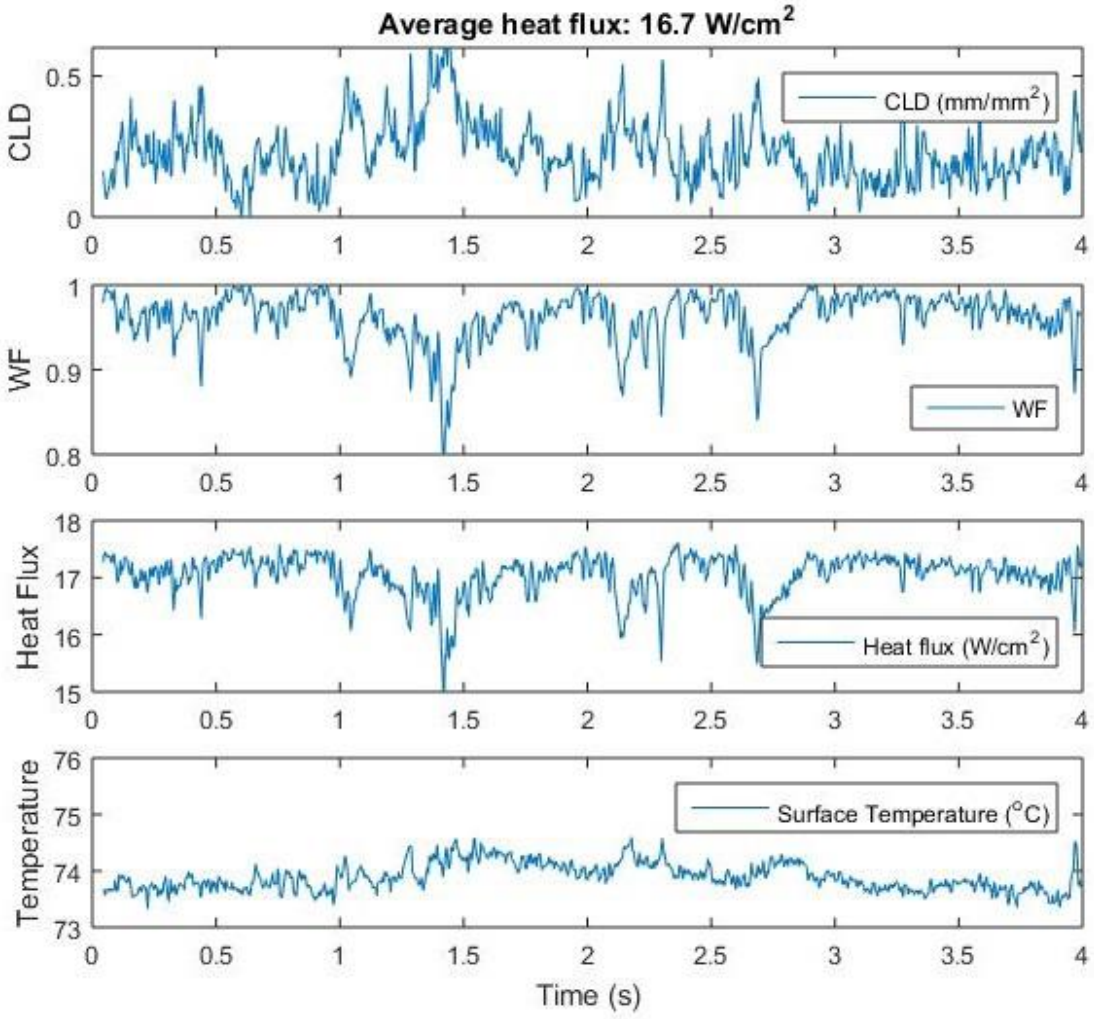

Figure 41: Experiment 2 (far jet) transient temperature, heat flux, wetted fraction (WF) and contact line density (CLD) data.

The Pearson product-moment coefficient was used to determine if there was a linear correlation between the transient wetted fraction, contact line density, wall temperature, and heat flux. The coefficient is equal to one for a perfect positive linear correlation and negative one for a perfect negative linear correlation. The coefficient is defined in Equation 14, where x_i and y_i are the data points, n is the sample size, s is the sample standard deviation, and the bar denotes mean.

Equation 14

$$r_{xy} = \frac{\sum_{i=1}^{n} x_i y_i - n\bar{x}\bar{y}}{(n-1)s_x s_y}$$

Table 8: Pearson coefficient matrix. The TtFB label is for the transition (and only the transition) to film boiling.

		Pearson's correlation coefficient					
Experiment	Heat Flux (W/cm^2)	T_W vs. q"	T_W vs. WF	T_W vs. CLD	Q vs. WF	Q vs. CLD	WF vs. CLD
1	16.7	-0.31	-0.41	0.42	0.95	-0.3	-0.35
1	17.2	-0.32	-0.43	0.53	0.95	-0.48	-0.63
2	18.5	-0.42	-0.54	0.49	0.96	-0.68	-0.77
2	19.2	-0.74	-0.76	0.52	0.98	-0.63	-0.69
3	15.0	-0.12	-0.24	0.48	0.95	-0.46	-0.66
4	18.8	0.15	-0.04	0.20	0.88	-0.26	-0.50
1	TtFB	-0.76	-0.75	-0.47	0.995	0.96	0.65
2	TtFB	-0.91	-0.90	0.10	0.99	0.03	0.00
3	TtFB	-0.73	-0.76	-0.44	0.98	0.82	0.80
4	TtFB	0.05	-0.24	-0.01	0.75	0.65	0.72

The Pearson coefficients are shown in Table 8, where the TtFB label in the heat flux column denotes the transition (and only the transition) from nucleate or transition boiling to film boiling. The wall temperature was used instead of the average surface temperature because it was clear that the latter would have a strong negative correlation with the wetted fraction and heat flux. The average surface temperature includes dry spots, which superheated to the silicon temperature and had low heat flux.

Only the average heat flux and wetted fraction had a strong positive linear relationship for all cases. The pre-TtFB heat flux measurements did not have any other strong correlations. The contact line density did not consistently demonstrate strong linear relationships with the other parameters.

For experiments 1, 2, and 3 (pool boiling, far jet, and pool boiling), the wall temperature had a negative correlation with the wetted fraction and heat transfer during the film boiling transition. That is, the wetted fraction and heat transfer decreased as the wall temperature increased. Experiment 4 (close jet) did not exhibit strong linear correlations because the surface had sections that transitioned to film boiling while others remained in the nucleate boiling regime. The increasing wall superheat during the local transition to film boiling caused enhanced heat transfer in the nucleate boiling regime under the jet.

The transient regional heat transfer contributions from the wetted, receding, and advancing areas are plotted in Figure 42 for experiment 1 (pool boiling) and Figure 43 for experiment 2 (far jet). The plots have increasing wall superheat from left to right. The wetted area generally contributed between 70 and 100 % of the total heat transfer and the percentage decreased as the wall superheat increased. For example, in Figure 42 the wetted contribution decreased approximately 10% due to the advancement from nucleate boiling (NB) to transition boiling (TB). Based on the contribution from the receding and advancing area, the contact line movement contributed less than approximately 10% of the total heat transfer.

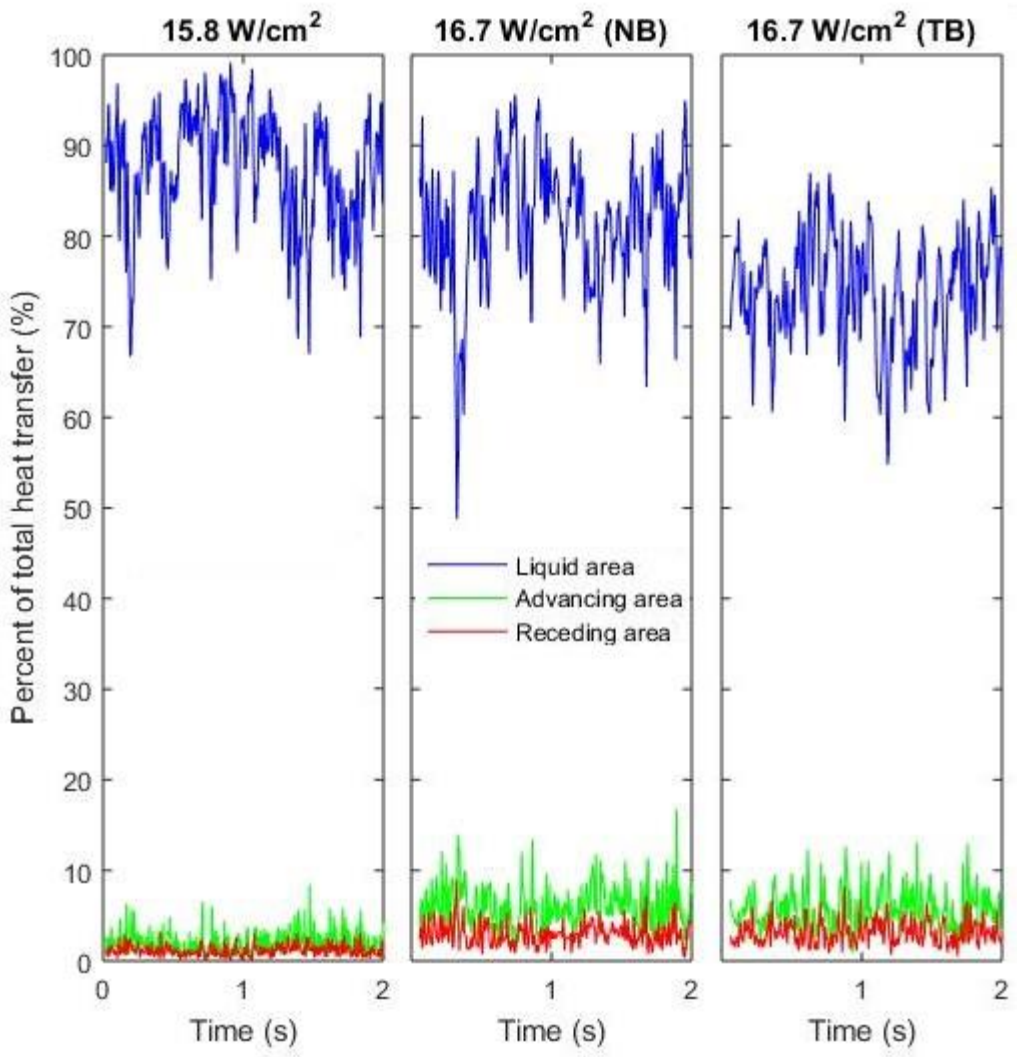

Figure 42: Regional heat transfer contributions from experiment 1 (close jet). The plots have increasing wall superheat from left to right. The (NB) and (TB) stand for nucleate boiling and transition boiling.

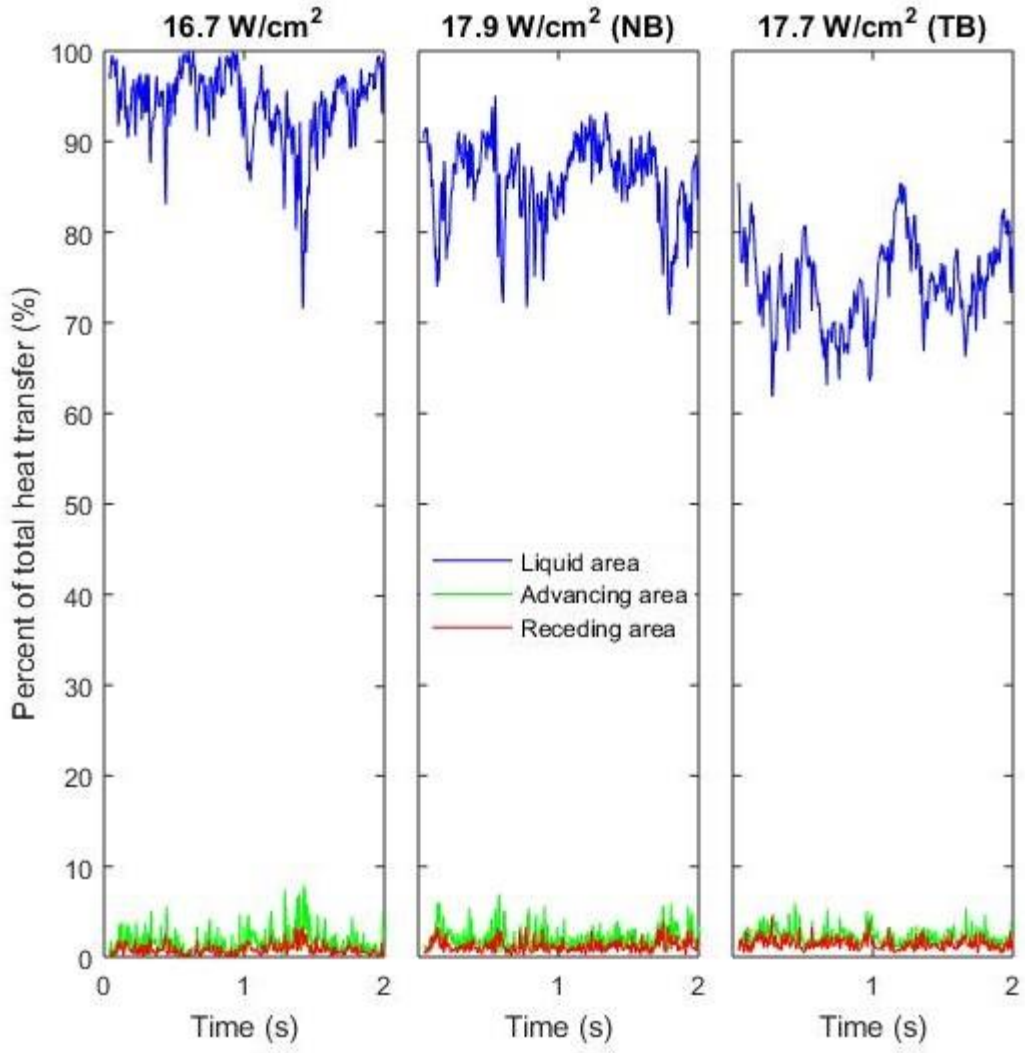

Figure 43: Regional heat transfer contributions from experiment 2 (far jet). The plots have increasing wall superheat from left to right. The (NB) and (TB) stand for nucleate boiling and transition boiling.

Figure 44 to Figure 47 show the boiling curves for each experiment with WF, liquid area heat flux, and the product of the WF and liquid area heat flux. These plots demonstrate that most of the heat transfer was from the wetted area and that the decrease in the heat transfer enhancement with increased wall superheat was due to dryout. CHF occurred when the liquid area heat flux and wetted fraction were

optimal. Therefore, it could be increased by increasing the heat transfer at the wetted area or by increasing the wetted fraction.

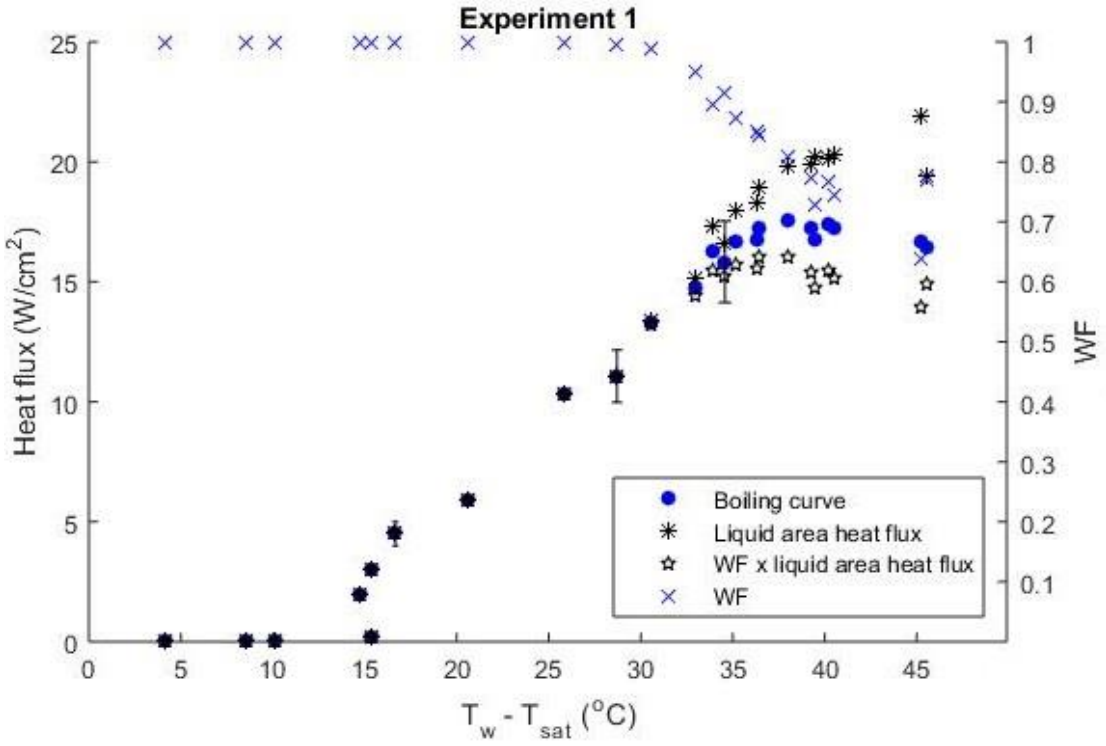

Figure 44: Experiment 1 (pool boiling) boiling curve with liquid area heat flux and WF.

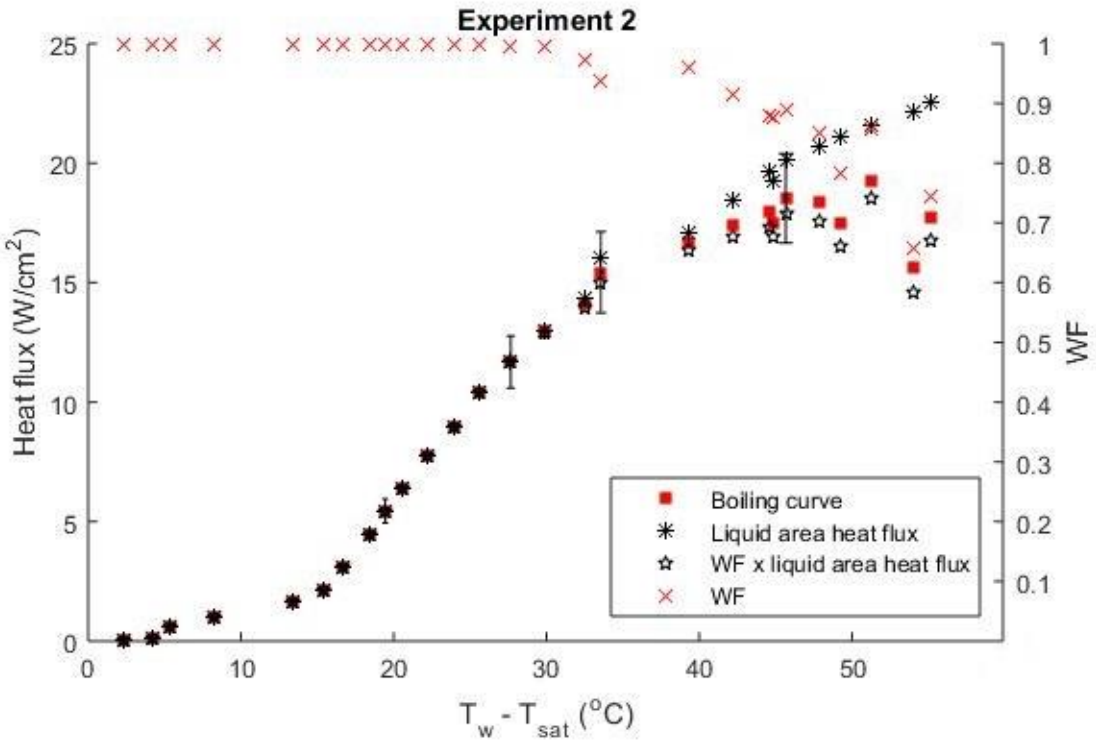

Figure 45: Experiment 2 (far jet) boiling curve with liquid area heat transfer and WF.

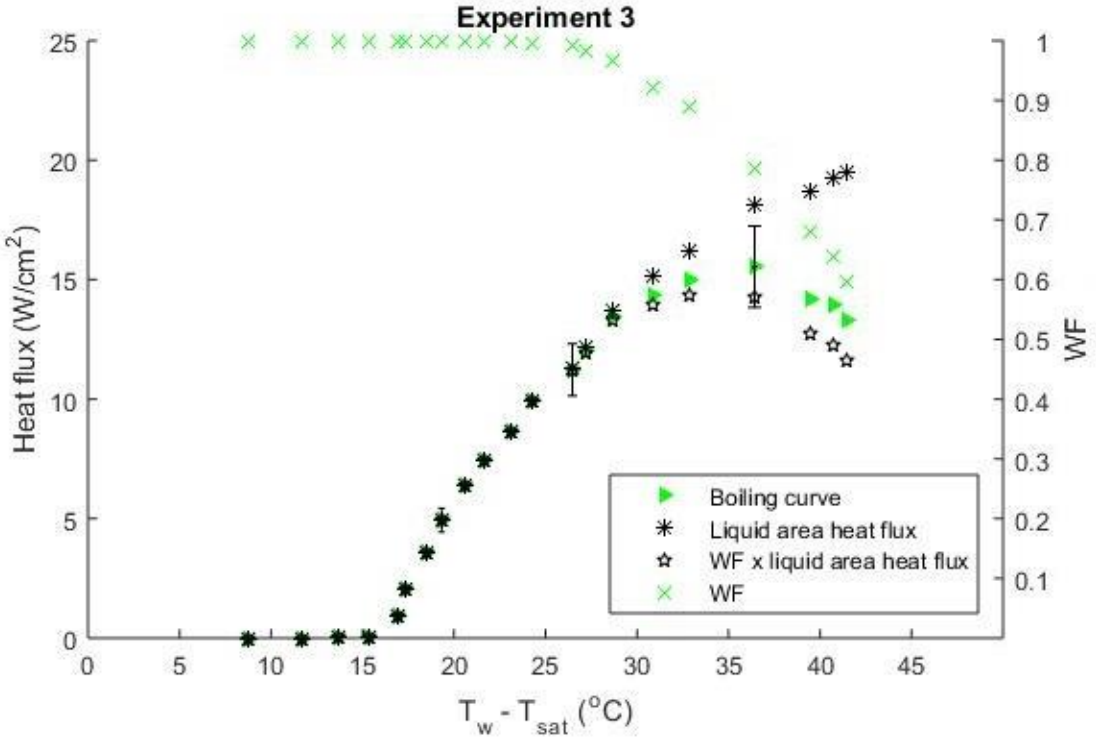

Figure 46: Experiment 3 (pool boiling) boiling curve with liquid area heat transfer and WF.

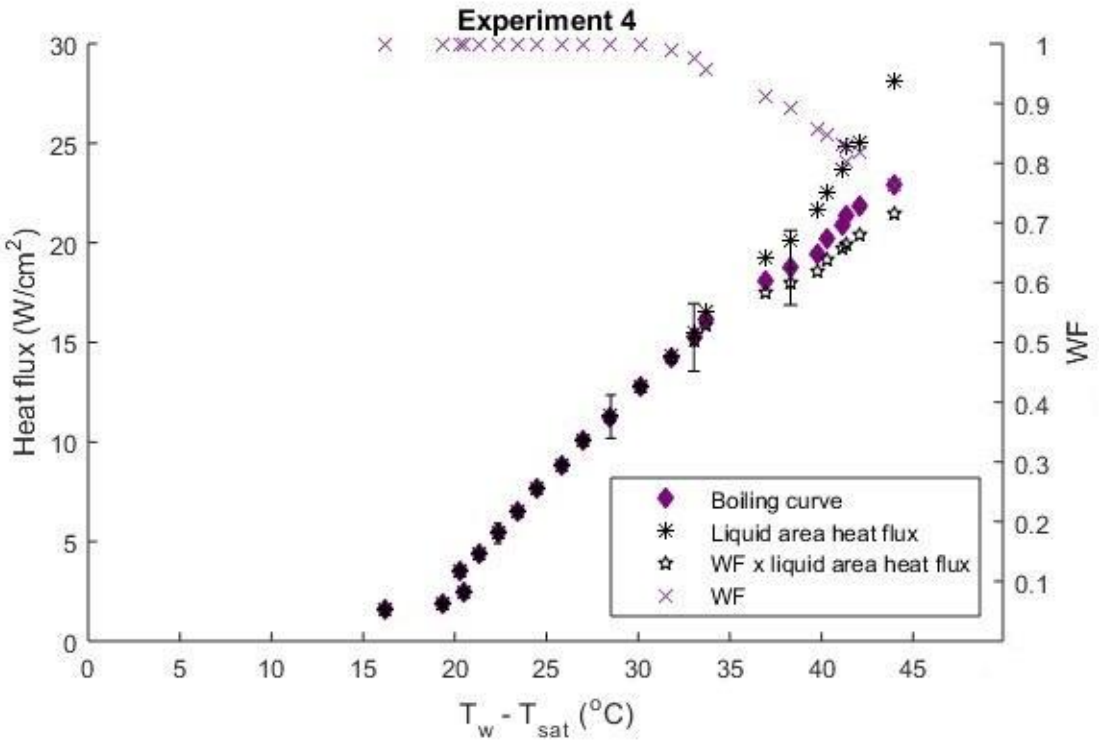

Figure 47: Experiment 4 (close jet) boiling curve with liquid area heat transfer and WF.

4.1.3 Dry Spot Characteristics

The dryout frequency, average duration of dry time, contact line speed, and dry spot area distributions are plotted in this subsection. Figure 48 and Figure 49 demonstrate that dryout was more frequent and lasted longer as the wall superheat increased. In addition, experiment 2 (far jet) and 4 (close jet) had less frequent dryout events than the pool boiling experiments.

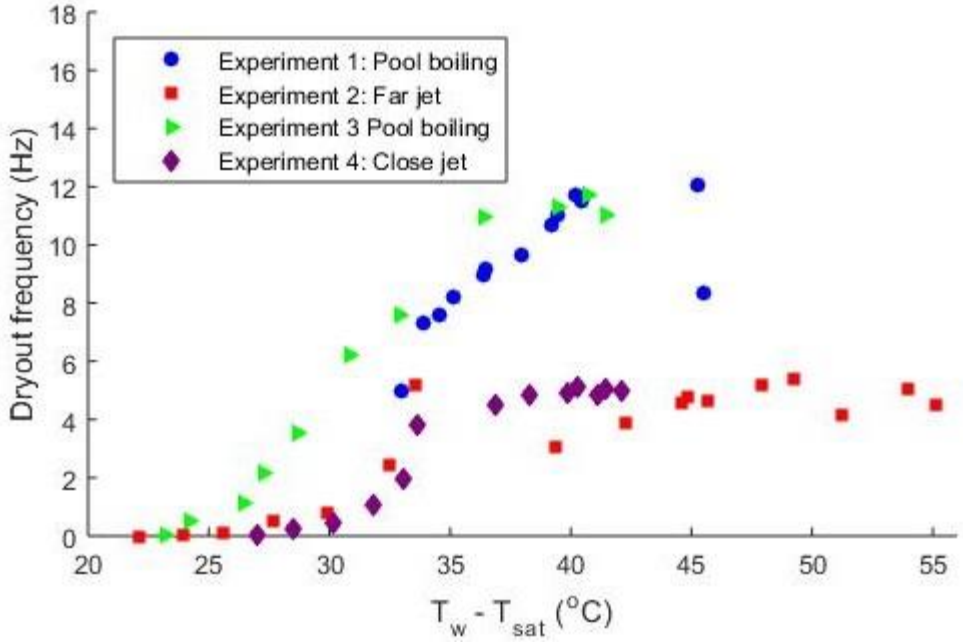

Figure 48: Dryout frequency (Hz) for all experiments.

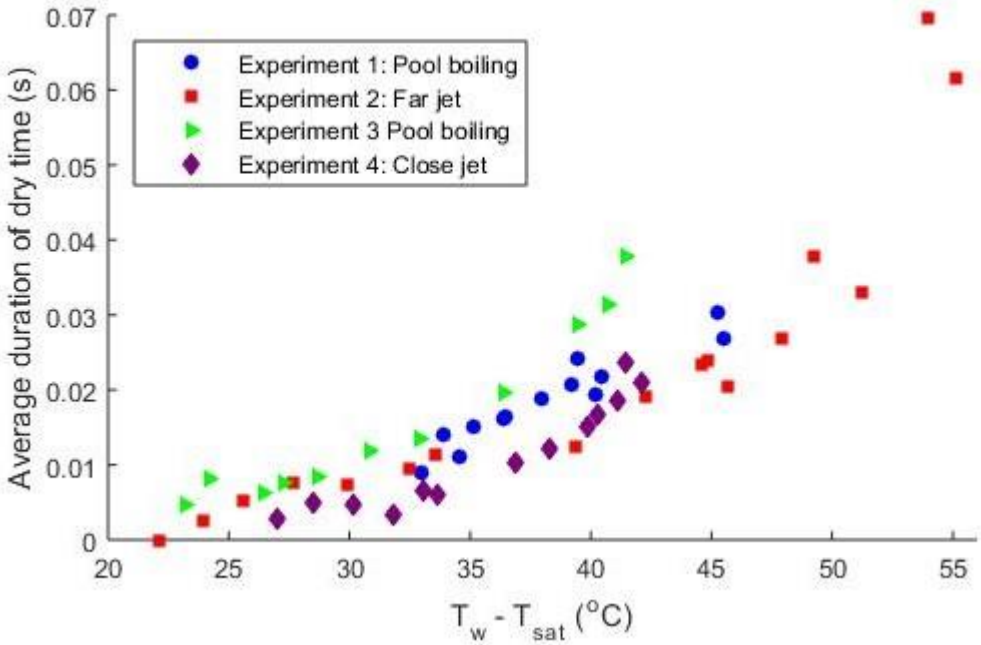

Figure 49: Average duration of dry time (s) for all experiments.

The average contact line speed, plotted in Figure 50, decreased as the wall superheat increased during experiment 1, 2, and 3 (pool boiling, far jet, and pool

boiling). The average contact line speed was approximately constant in experiment 4, but the local behavior was significant and these results are discussed in more detail in the next section. Contact line speed and dry patch size histograms are plotted in Figure 51 to Figure 55. For the dry patch size histograms, the individual dry patches were grouped into 5 mm^2 bins and plotted against their contribution to the total dry area. For example, approximately 87% of the dry area was from patches less than 5 mm^2 during the 16.3 W/cm^2 heat flux measurement in experiment 1 (Figure 53). The right most plot in Figure 53 to Figure 55 show the individual dry patch area contribution during the transition to film boiling. These histograms show that the dry spot size increased and the average contact line speed decreased as the wall superheat increased. In addition, the standard deviation of the contact line speed decreased as the large, low heat transfer, and slow moving dry spots covered more of the surface.

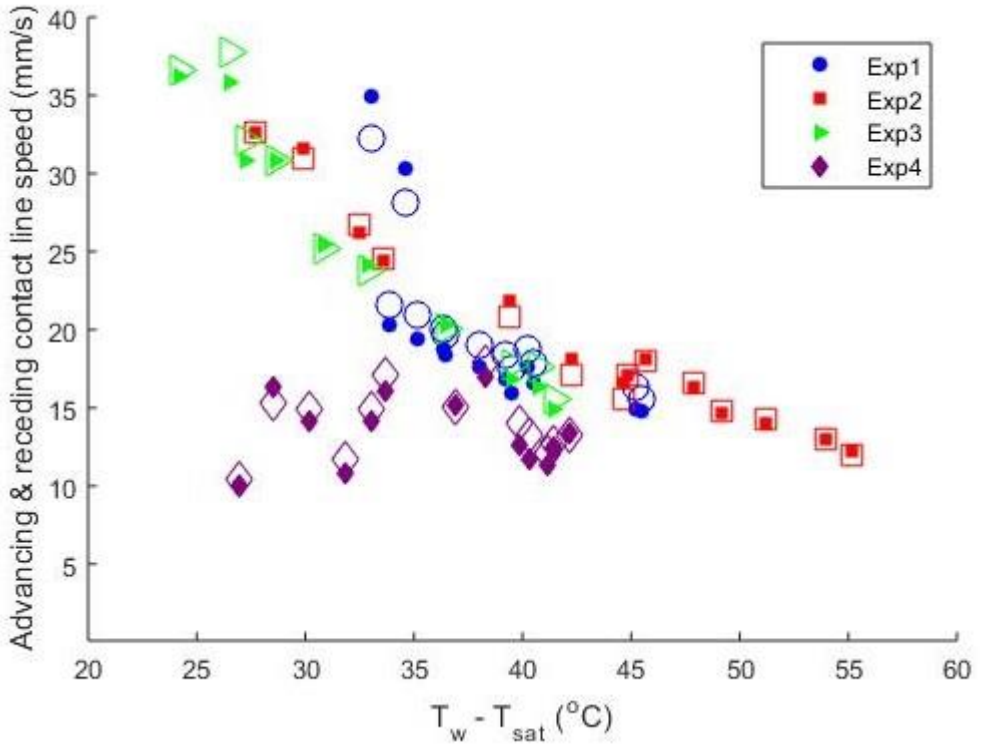

Figure 50: Contact line speed for all experiments. The filled markers are for the advancing area and the receding markers are open.

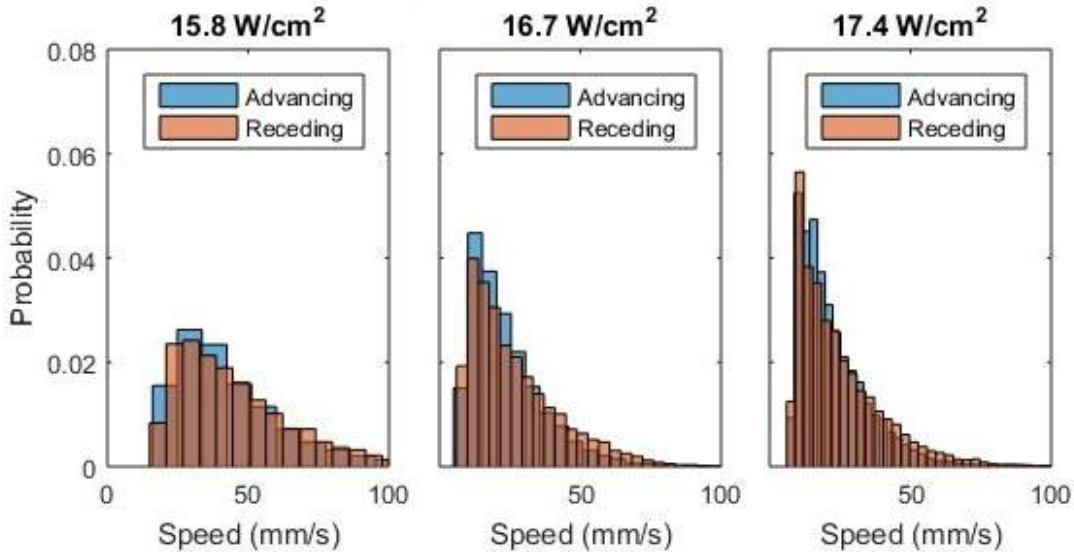

Figure 51: Experiment 1 (pool boiling) contact line speed histograms. The plots have increasing wall superheat from left to right.

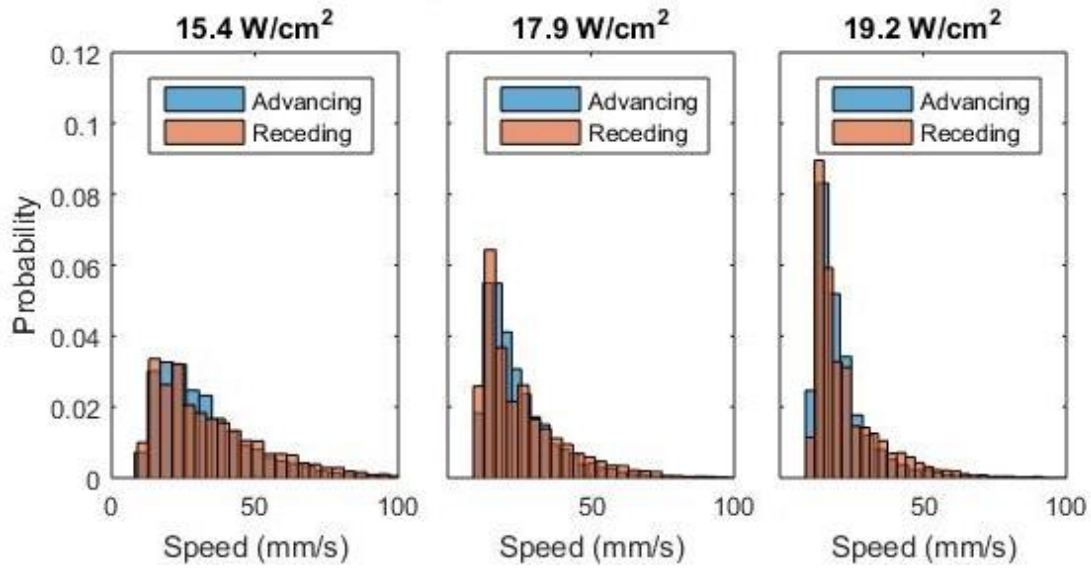

Figure 52: Experiment 2 (far jet) contact line speed histograms. The plots have increasing wall superheat from left to right.

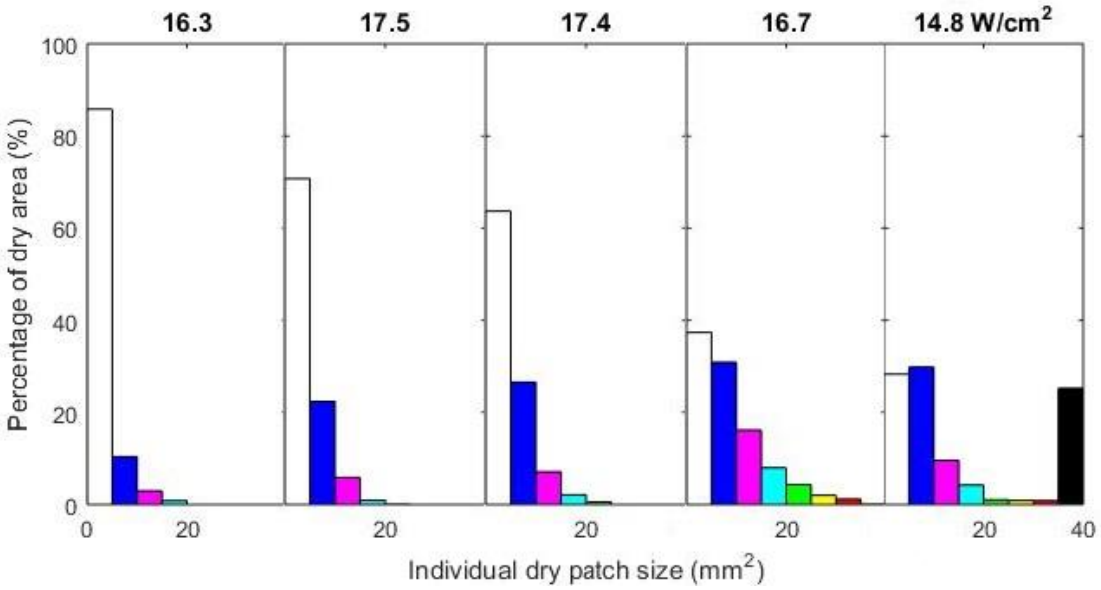

Figure 53: Experiment 1 (pool boiling) dry patch size data. The bar plots show the amount each individual dry patch size, in bins of 5 mm^2, contributed to the total dry area. They are in order of increasing wall superheat. The final bar plot is during the transition to film boiling.

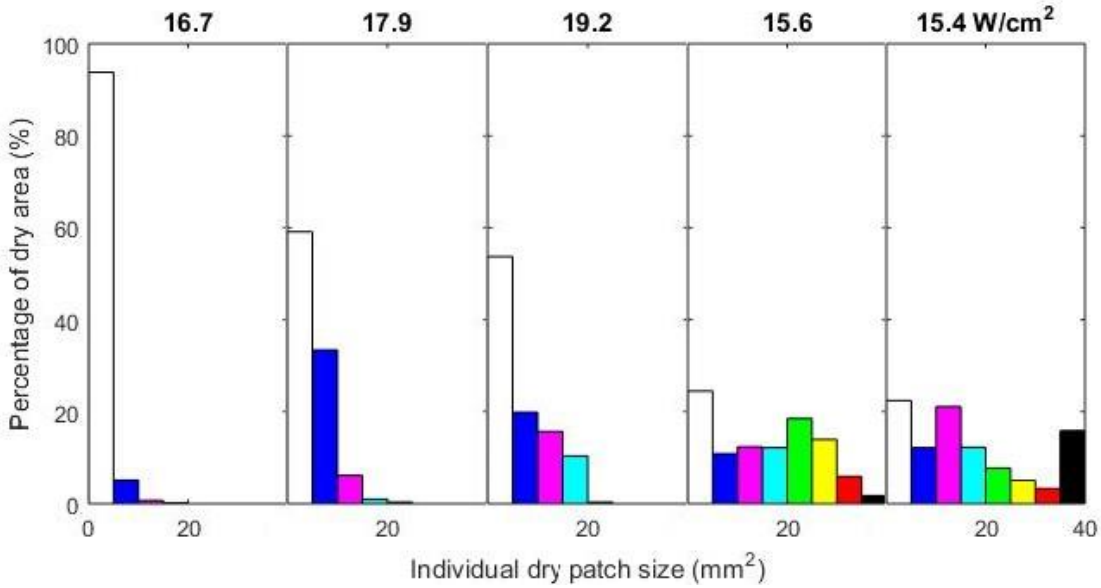

Figure 54: Experiment 2 (far jet) dry patch size data. The bar plots show the amount each individual dry patch size, in bins of 5 mm^2, contributed to the total dry area. They are in order of increasing wall superheat. The final bar plot is during the transition to film boiling.

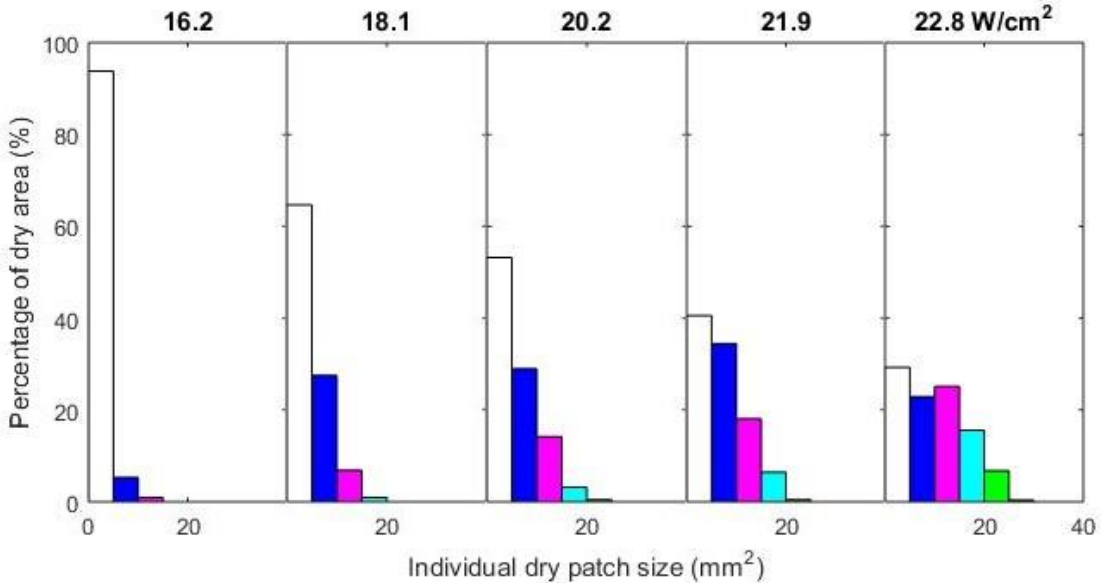

Figure 55: Experiment 4 (close jet) dry patch size data. The bar plots show the amount each individual dry patch size, in bins of 5 mm^2, contributed to the total dry area. They are in order of increasing wall superheat. The final bar plot is during the transition to film boiling.

The transient individual dry patch size contribution to the total dry area during the transition to film boiling of experiment 1 (pool boiling) and 2 (far jet) is plotted in Figure 56 and Figure 57. The dry patches were categorized as large or small, and small dry patches were defined as less than 15 mm^2 and 25 mm^2 for the respective

experiments. The transient dry patch contributions were averaged over ±2 seconds to smooth out the data. The figures also include the wetted fraction and the surface temperature. These plots show that the dry area and surface temperature increased as the dry patches size increased.

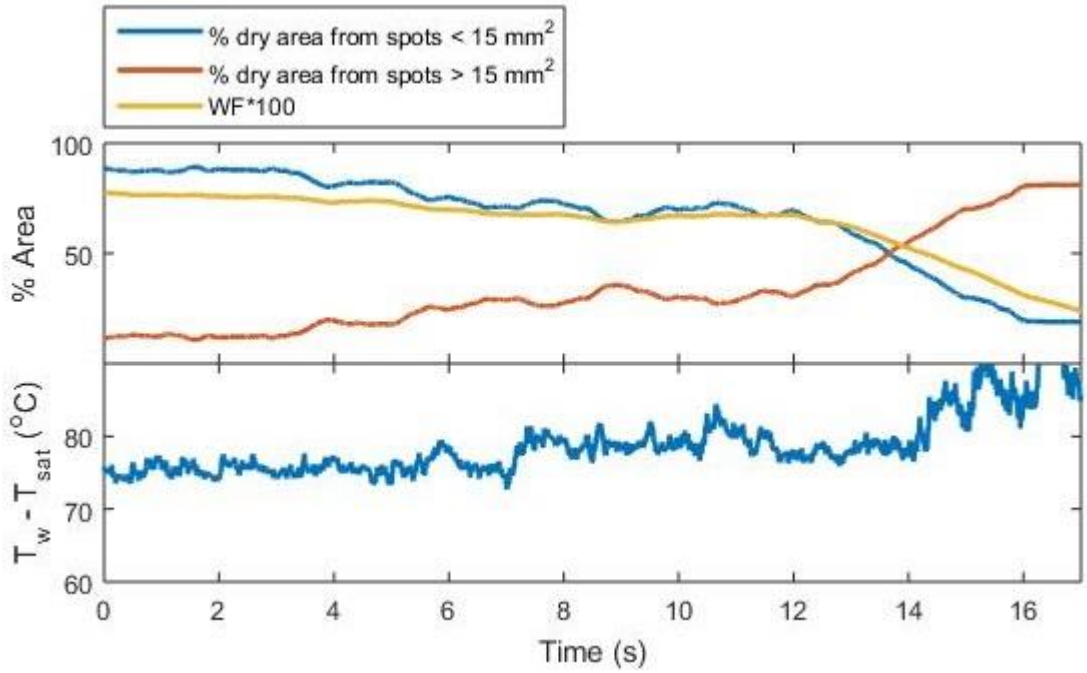

Figure 56: Experiment 1 (pool boiling) dry spot, wetted fraction, and wall temperature data during the transition to film boiling. The top plot shows the percentage of the dry area covered by vapor patches greater and smaller than 15 mm^2 and the WF x 100. The bottom plot shows the transient (frame average) wall temperature.

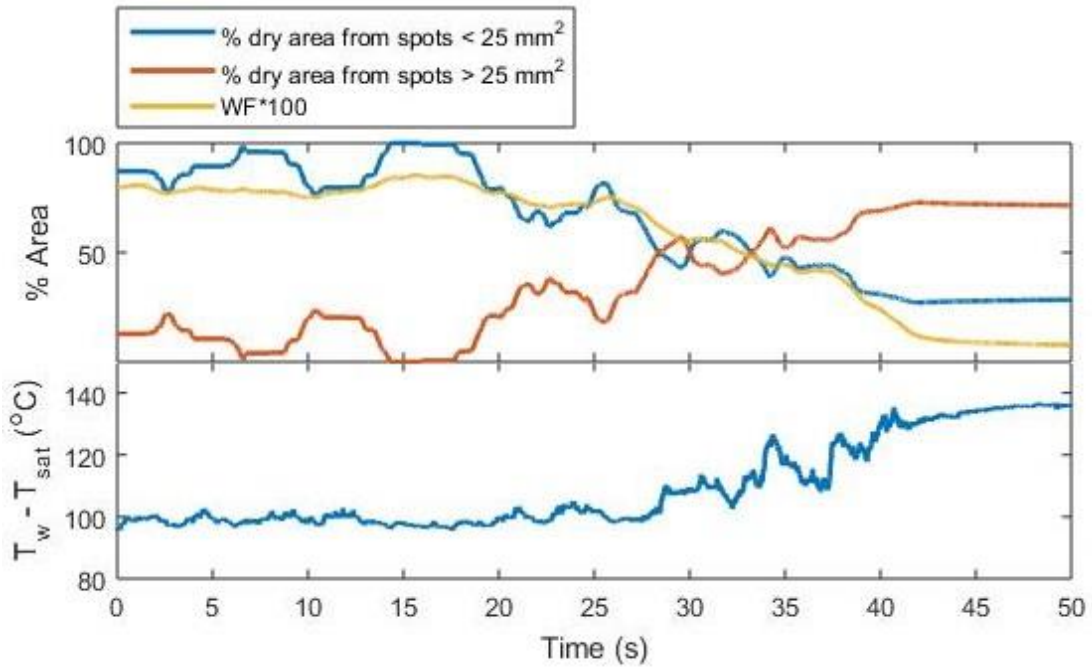

Figure 57: Experiment 2 (far jet) dry spot, wetted fraction, and wall temperature data during the transition to film boiling. The top plot shows the percentage of the dry area covered by vapor patches greater and smaller than 25 mm^2 and the WF x 100. The bottom plot shows the transient (frame average) wall temperature.

Section 4.2: Local Investigation

All four of the experiments demonstrated localized boiling behavior. The forced convection during experiment 2 (far jet) and 4 (close jet) affected the local superheat and dryout. The pool boiling experiments demonstrated localized behavior due to the test heater and holder configuration (Figure 6). The test heater, which had approximately uniform heat generation within the cross-section of the silicon, was not wetted where the O-rings sealed. As a result, the liquid exposed areas near the O-rings had a higher effective heat generation and wall superheat.

The local analysis was conducted by partitioning the test heater surface into rings centered about the jet, as shown in Figure 58. The rings were 1.25 mm thick and

the center circle had a radius of 1.25 mm. The boiling curves and dry spot characteristics were evaluated for each area.

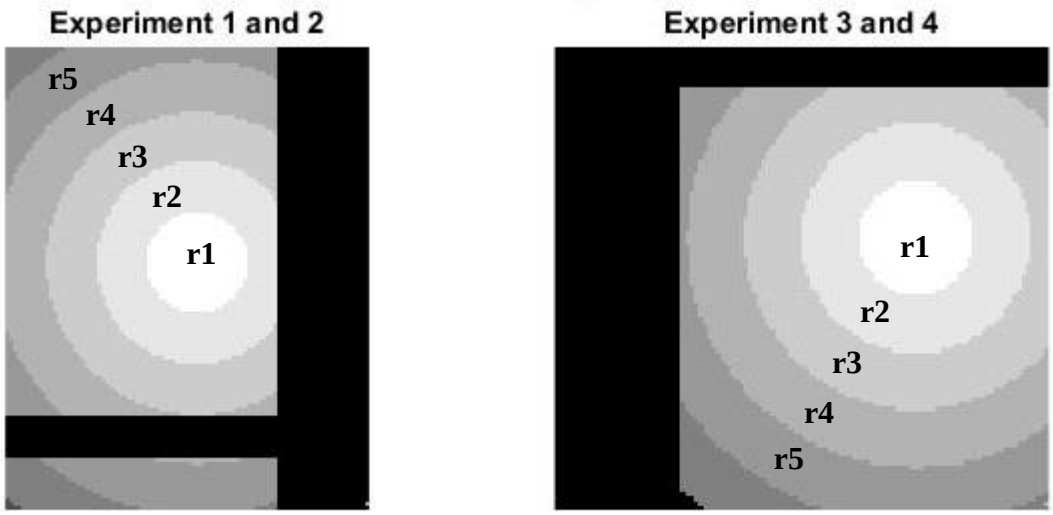

Figure 58: Key for local boiling investigation. The jet is centered at the r1 circle. The radius of r1 is 1.25 mm and each ring has a thickness of 1.25 mm.

4.2.1 Local Boiling Curves

The local boiling curves are plotted for each experiment in Figure 59 to Figure 62. Experiment 4 demonstrated the most distinct local behavior. For example, the first IR measurement (Figure 62), made before the onset of nucleate boiling, demonstrated that the heat transfer coefficient decreased rapidly with radial distance from the jet center. The final IR measurement shows the regions close to the jet were still in the nucleate boiling regime when the peripheral regions were in the transition boiling regime.

The enhanced heat transfer during the slug and column nucleate boiling regime of experiment 4 was discussed in the previous section (see page 56). It was observed that the slope of the boiling curve did not decrease as the wetted fraction

decreased. From Figure 62, this is because the inner two areas had enhanced heat transfer for wall superheats greater than 37 ˚C, and the slope of the local boiling curve increased. The mechanism of enhancement is not known.

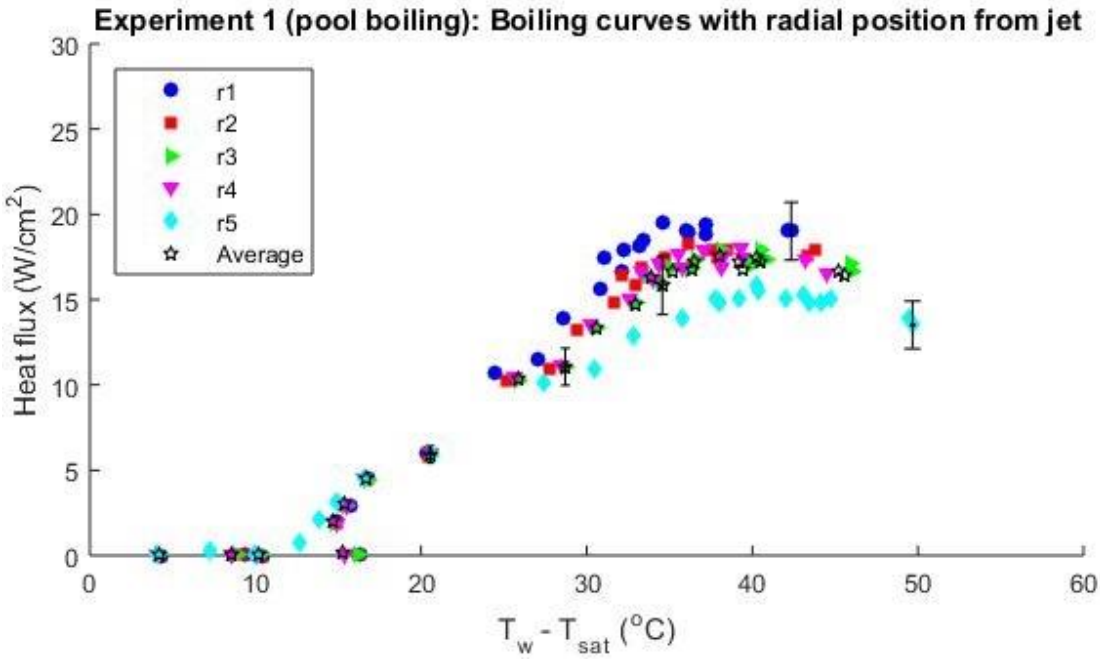

Figure 59: Experiment 1 local boiling curves.

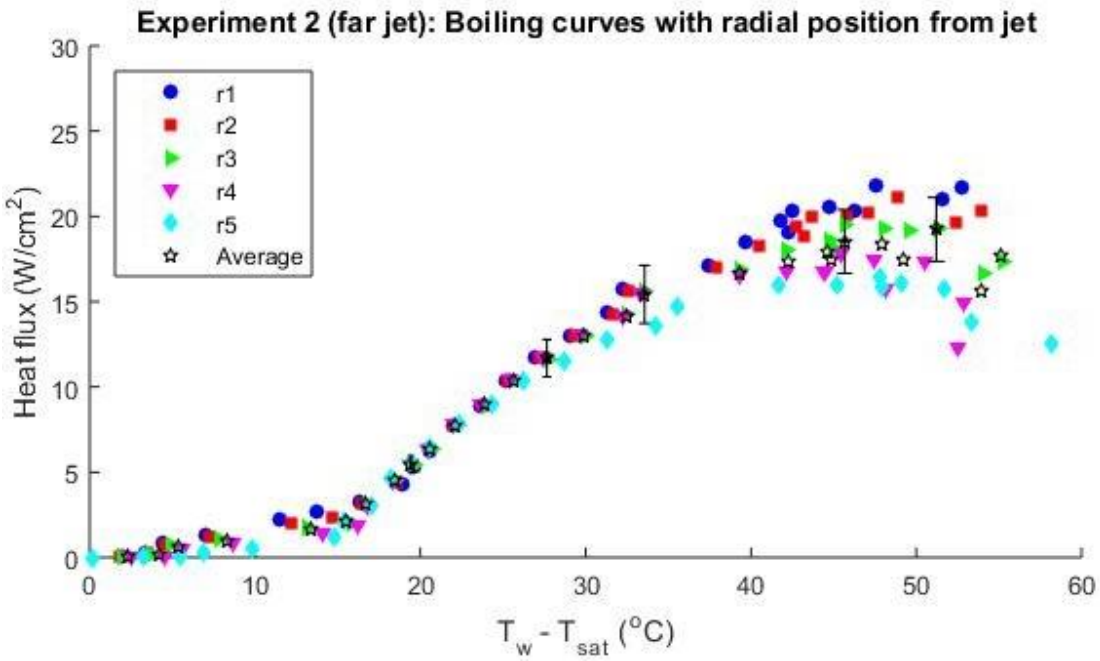

Figure 60: Experiment 2 (far jet) local boiling curves.

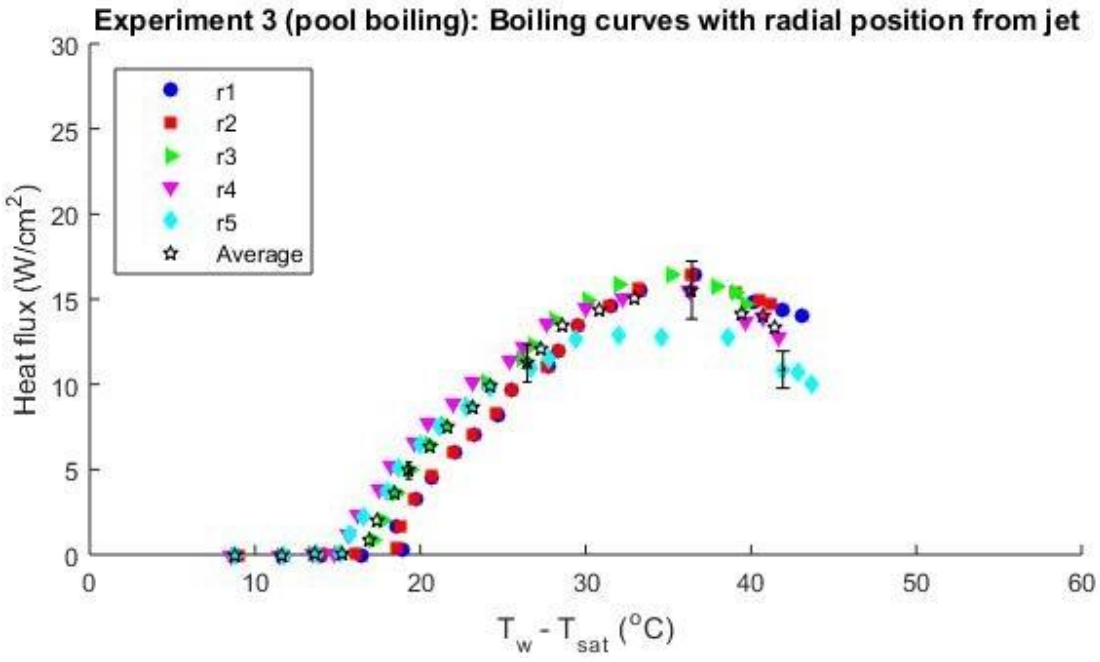

Figure 61: Experiment 3 (pool boiling) local boiling curves.

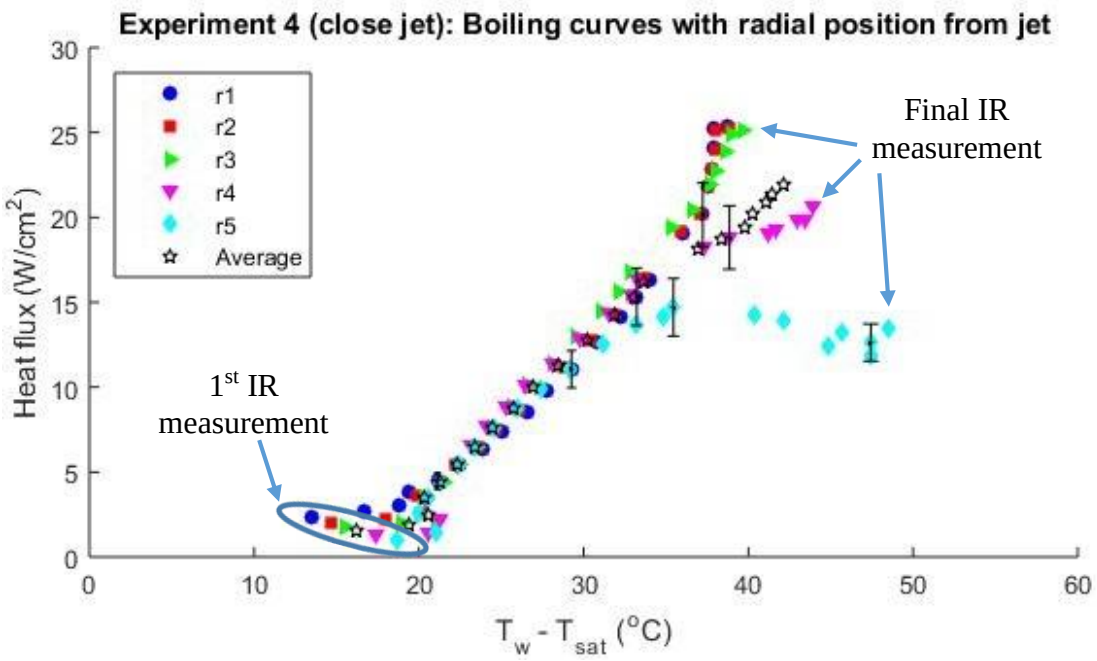

Figure 62: Experiment 4 (close jet) local boiling curves.

The behavior demonstrated in the wetted fraction and liquid area boiling curves shown in Figure 44 to Figure 47 was also observed for the local regimes. This is demonstrated for experiment 4 (close jet) in Figure 63, where the boiling regimes changed most rapidly in space. The r1 and r2 rings had WF>0.99 for all measurements, so they were omitted.

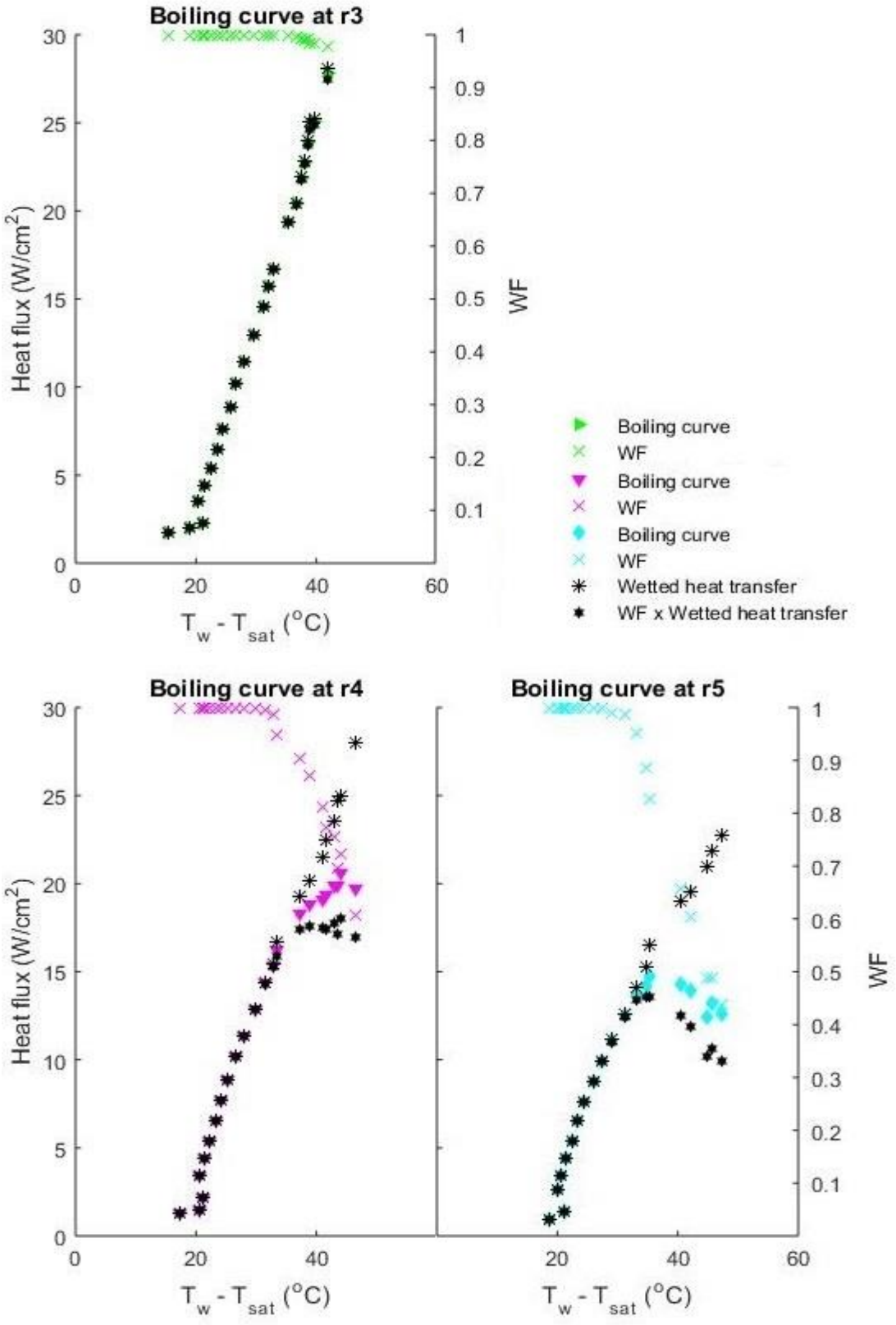

Figure 63: Experiment 4 boiling curve with liquid area heat transfer and WF.

4.2.2 Dry Spot Characteristics

The local dry spot characteristics were plotted with respect to the local superheat. They had less scatter when plotted against local wall superheat instead of the local heat flux or surface averages.

The local dryout frequency is plotted in Figure 64 and Figure 65. Generally, the dryout frequency was maximum near CHF, and then decreased as large, low heat transfer, and long lasting dry spots became more common. The average duration of the dryout events increased rapidly with superheat, as shown in Figure 66 and Figure 67.

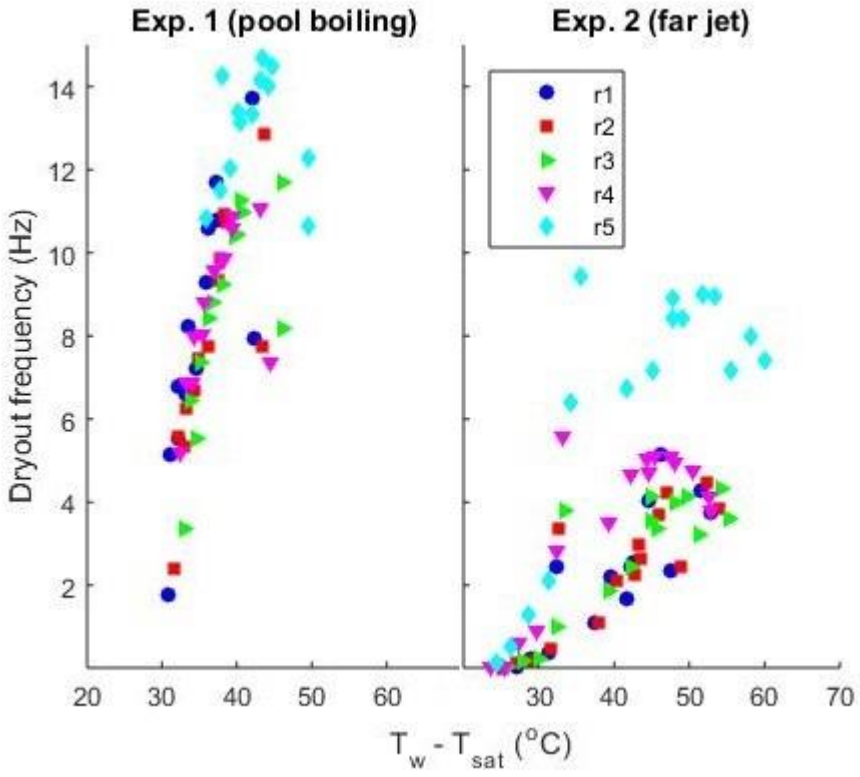

Figure 64: Dryout frequency for experiment 1 (pool boiling) and 2 (far jet).

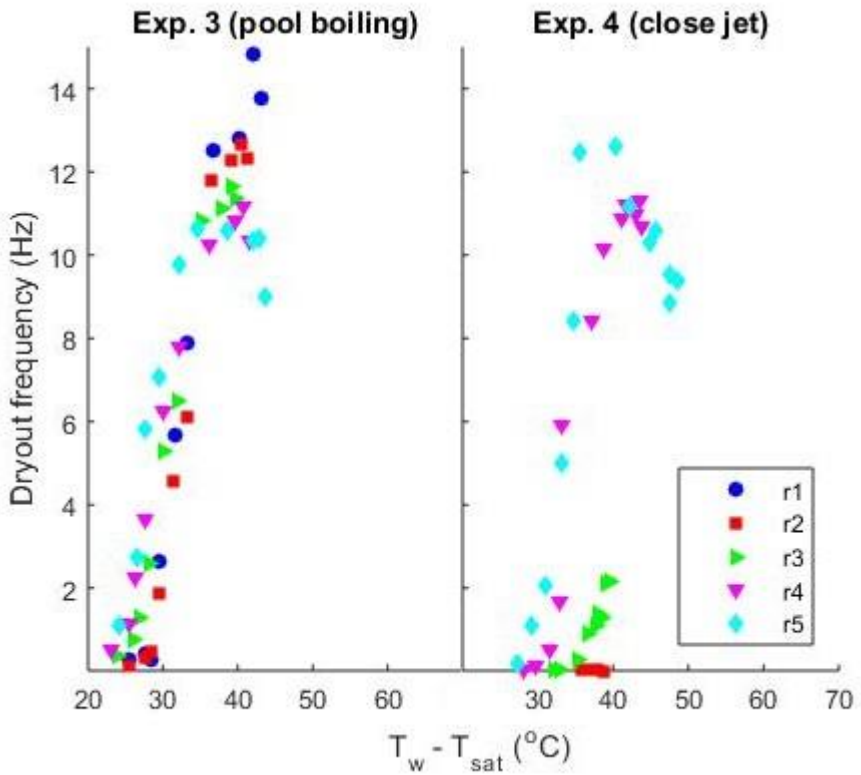

Figure 65: Dryout frequency for experiment 1 (pool boiling) and 2 (close jet).

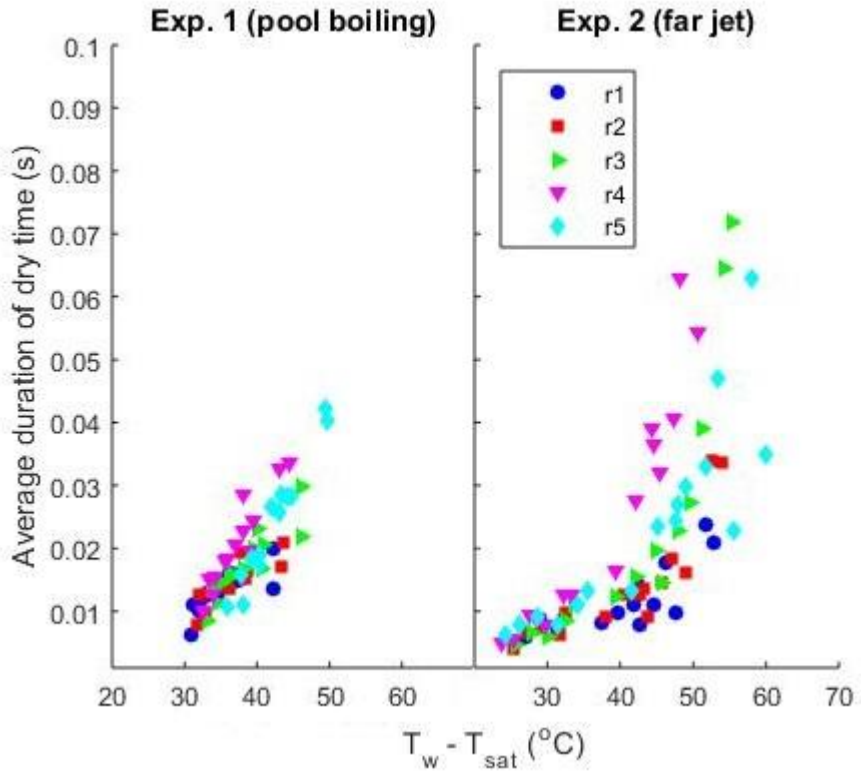

Figure 66: Average duration of dry time for experiment 1 (pool boiling) and 2 (far jet).

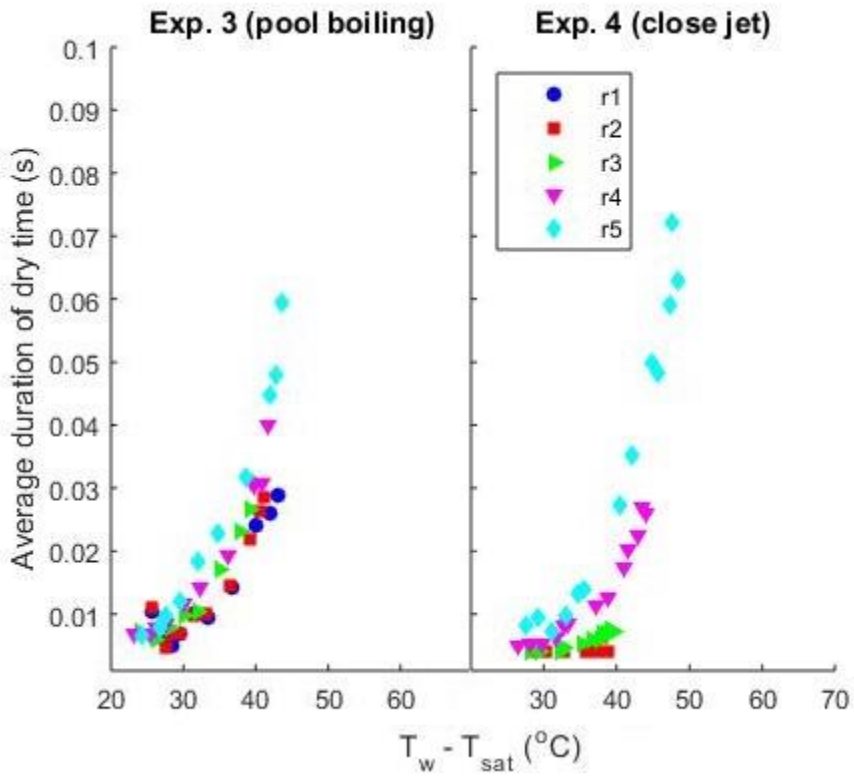

Figure 67: Average duration of dry time for experiment 3 (pool boiling) and 4 (close jet).

The advancing and receding contact line speeds are shown in Figure 68 and Figure 69. All the experiments show that the contact line speed generally decreased with wall superheat. The r2 and r3 rings in experiment 4 had increasing contact line speed with wall superheat, but they were in the early stages of dryout and WF >0.98 for all measurements. Higher superheats would needed to investigate the trends near CHF.

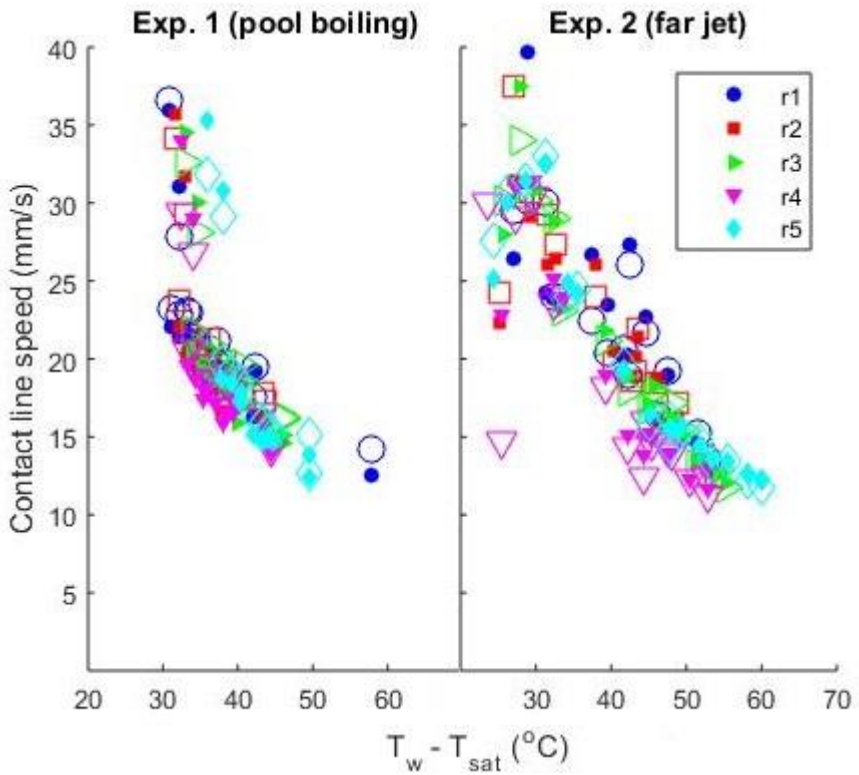

Figure 68: Advancing and receding contact line speed for experiment 1 (pool boiling) and 2 (far jet). The open markers are for the receding areas and the filled markers are for the advancing area.

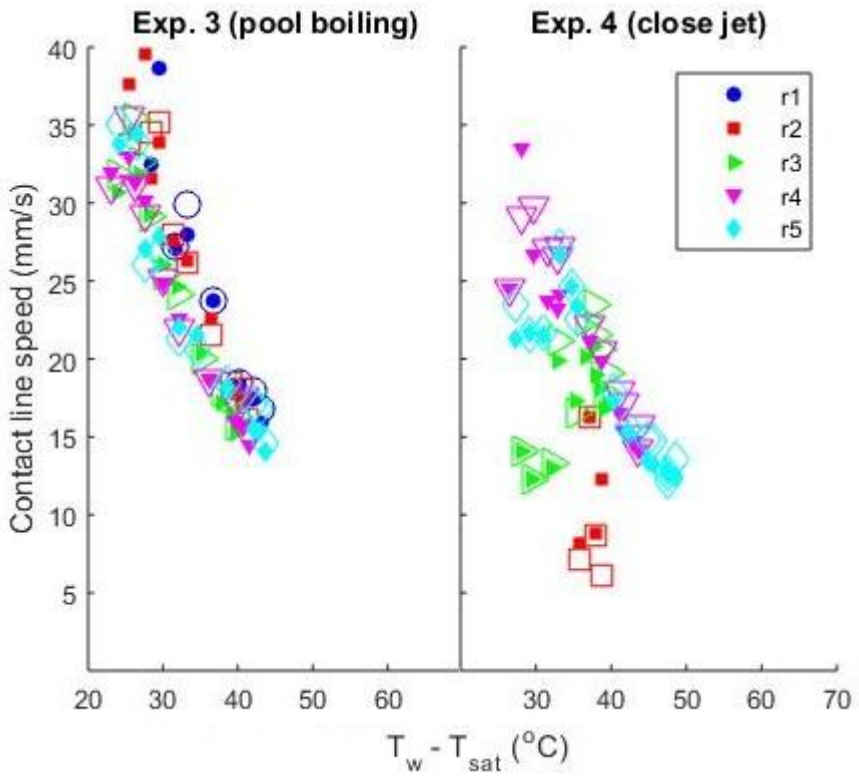

Figure 69: Advancing and receding contact line speed for experiment 3 (pool boiling) and 4 (close jet). The open markers are for the receding areas and the filled markers are for the advancing area.

The experiment 4 data shown in Figure 55, which plots the individual dry patch contribution to the total area, was local to r4 and r5 because they were the only regions with significant dryout. The transient behavior for r4 and r5 during the film boiling transition is plotted in Figure 70. The transient dry patch size contributions to the total dry area were averaged over ± 0.8 seconds to smooth out the data. The figure shows that the wetted fraction decreased and the average wall temperature increased slightly as the dry spots become larger. The wall temperature spiked to high superheats during the transition and then cooled. The cooling was assumed to be due to the forced convection and transient liquid inflows.

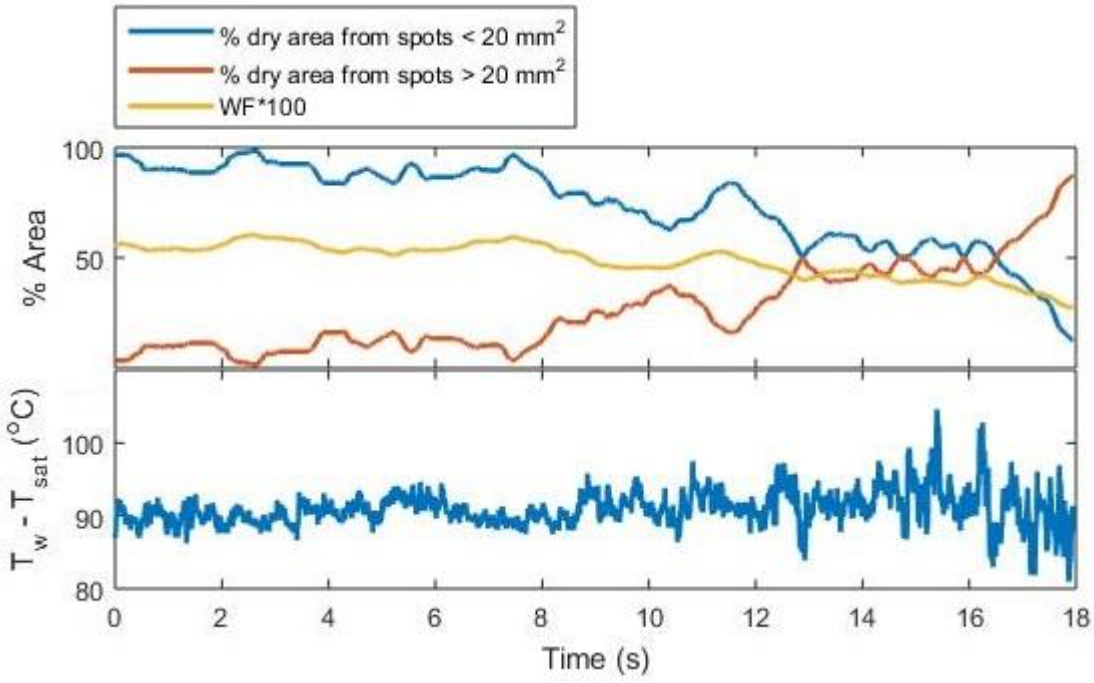

Figure 70: Experiment 4 (close jet) dry spot, wetted fraction, and wall temperature data during the transition to film boiling. The top plot shows the percentage of the dry area covered by vapor patches greater and smaller than 20 mm^2 and the WF x 100. The bottom plot shows the frame average wall temperature.

Chapter 5: Conclusions

A study has been conducted on CHF mechanisms and the transition to film boiling during pool boiling and submerged jet impingement. The impinging jet experiments offered new perspective on the conditions that cause CHF, the generality of pool boiling CHF mechanisms, the transition to film boiling, and the significance of the macro flow field.

5.1 CHF Mechanisms

It has been observed that the pool boiling and impinging jet experiments were governed by similar CHF mechanisms. This finding suggests a generality of pool boiling CHF mechanisms and that they may extend to more forced convection flows. The following CHF mechanisms were observed for all experiments:

1. The dry patches were classified into two categories. The first group were generally small dry patches that had very short lifetimes, fast contact line speeds, and moderate heat transfer. They were observed at all heat fluxes after the onset of dryout and became less frequent at high wall superheats. The second group were relatively large dry patches that were believed to form when the liquid entrained within a moderate heat transfer dry patch boiled before it rewetted, which resulted in superheating. These dry spots had long life times, slow contact lines speeds, and very low heat transfer. Their frequency increased with wall superheat and they were less likely to rewet as their size increased.

2. Most of the heat transfer near CHF was through the wetted area and the decrease in the heat transfer enhancement with increased wall superheat was due to dryout. CHF occurred when the liquid area heat flux and wetted fraction were optimal. As a result, CHF could be increased by increasing the heat transfer at the wetted area or by increasing the wetted fraction.

5.2 The Film Boiling Transition

Early transition boiling regime measurements could be obtained because the heat generation within the silicon decreased locally at dryout. This was unique to this test heater, and therefore the generality of the film boiling transition in these experiments may be questionable. However, it was observed that similar mechanisms caused the transition during the pool boiling and impinging jet experiments.

The transition to film boiling occurred when the heat generated within the silicon exceeded the heat transfer from the surface. The low heat transfer and slow moving dry patches described above were the catalysts for the transition to film boiling. These spots superheated and caused the surrounding wall temperature to increase, which increased the probability of additional dryout and superheating. This process caused the wetted fraction and average heat flux to decrease.

5.3 Analysis of Hydrodynamic Models

The hydrodynamic models postulated that CHF was limited by the ability of the bulk liquid to penetrate the vapor and resupply the test heater. For the Zuber model, the Helmholtz instability between the vapor and liquid caused vapor columns

to collapse and prevent liquid resupply. However, the observed results did not support this model. The jet in experiment 2 provided only slight enhancement to CHF, but supplied approximately 4 times more liquid to the test surface than could be boiled if all the input power at CHF converted liquid to vapor.

The macrolayer model stated that CHF occurred when a large bubble hovered over the boiling surface and prevented the bulk fluid from rewetting a liquid film. The jet in experiment 2 penetrated the reported macrolayer thickness [11], however, and it is believed that the high mass flow rate would have dispersed the vapor bubble, resupplied the liquid film, and significantly increased CHF if this model was correct.

While the jet during experiment 2 did not significantly increase CHF, surface enhancements have been demonstrated to increase CHF by over 100% [14 - 16]. The surface enhancements increased CHF by promoting rewetting with wicking surfaces or increasing the heat transfer at the liquid area. These results support the conclusion by Theofanous [18] that CHF is governed by the surface characteristics and micro dynamics, instead of the macro fluid dynamics.

Experiment 4, where the volumetric flow rate was 105 ml/min (2.45 g/s) and the jet height was 3.3 mm, demonstrated CHF enhancement locally. The jet was observed to enhance heat transfer at the wetted area and prevent dryout, which demonstrates that the jet affected the micro dynamics.

Appendix

Table 9: Camera settings summary for experiment 1.

Measured heat flux (W/cm^2)	Camera frequency per integration time(Hz)	Number of integration times	Was dryout present?
0	839	1	no
0	839	1	no
0	839	1	no
0.1	839	1	no
0.3	839	1	no
1.9	839	1	no
3.1	839	1	no
4.7	839	1	no
6.2	839	1	no
10.7	419.5	2	yes
11.5	419.5	2	yes
13.8	419.5	2	yes
15.4	419.5	2	yes
16.5	419.5	2	yes
16.9	166.6	3	yes
17.4	166.6	3	yes
17.5	166.6	3	yes
18.0	166.6	3	yes
18.3	166.6	3	yes
18.2	166.6	3	yes
17.8	166.6	3	yes
18.2	166.6	3	yes
18.3	166.5	3	yes
18.0	166.6	3	yes
17.6	166.6	3	yes
TtFB	166.6	3	Yes

Table 10: Camera settings summary for experiment 2.

Measured heat flux (W/cm^2)	Camera frequency per integration time(Hz)	Number of integration times	Was dryout present?
0	500	1	no
0	500	1	no
0	500	1	no
0.1	500	1	no
0.5	500	1	no
0.9	500	1	no
1.6	500	1	no
2.2	500	1	no
3.1	500	1	no
4.6	500	1	no
5.6	500	1	no
6.5	500	1	no
8.1	250	2	no
9.1	250	2	yes
10.5	250	2	yes
11.9	250	2	yes
13.2	250	2	yes
14.3	250	2	yes
15.7	250	2	yes
17.0	250	2	yes
17.9	250	2	yes
18.1	250	2	yes
18.5	250	2	yes
19.0	250	2	yes
19.0	250	2	yes
18.4	250	2	yes
16.9	250	2	yes
20.1	250	2	yes
19.0	250	2	yes
TtFB	250	2	yes

Table 11: Camera settings summary for experiment 3.

Measured heat flux (W/cm^2)	Camera frequency per integration time(Hz)	Number of integration times	Was dryout present?
0	200	1	no
0	200	1	no
0	200	1	no
0	200	1	no
0	200	1	no
0	200	1	no
0.9	200	1	no
2.0	200	1	no
3.6	200	1	no
5.0	200	1	no
6.4	200	1	no
7.5	200	1	no
8.7	250	1	no
10.0	250	1	yes
11.3	250	1	yes
12.2	250	2	yes
13.6	250	2	yes
14.6	250	2	yes
15.3	250	2	yes
16.1	250	2	yes
15.2	250	2	yes
15.2	250	2	yes
TtFB	250	2	yes

Table 12: Camera settings summary for experiment 4.

Measured heat flux (W/cm^2)	Camera frequency per integration time(Hz)	Number of integration times	Was dryout present?
1.4	200	1	no
1.9	200	1	no
2.5	200	1	no
3.5	200	1	no
4.5	200	1	no
5.5	200	1	no
6.6	200	1	no
7.7	200	1	no
8.9	200	1	no
10.2	200	2	no
11.4	250	2	yes
12.9	250	2	yes
14.4	250	2	yes
15.4	250	2	yes
16.3	250	2	yes
18.0	250	2	yes
19.0	250	2	yes
19.6	250	2	yes
20.2	250	2	yes
20.8	250	2	yes
21.1	250	2	yes
21.6	250	2	yes
TtFB	250	2	yes

Glossary

Advancing area: Area that was dry in the previous frame but wet in the present frame

Average duration of dry time: the average amount of time each dryout event lasts at an average pixel

Contact line density (CLD): the total contact line length divided by the total area (mm/mm^2)

Contact line length: the total length (mm) of the contact line in a frame

Contact line speed: the speed (mm/s) that the contact line moves at each advancing and receding area

Critical heat flux (CHF): The maximum heat flux of the nucleate boiling regime

Dryout frequency: the frequency at which dryout events occur

Receding area: Area that was wet in the previous frame but dry in the present frame

Transition boiling: The boiling regime between nucleate and film boiling. It begins at CHF and is characterized by decreasing heat flux with increasing wall temperature

Triple phase contact line (contact line): the boundary between the liquid, vapor, and solid boiling surface

Wall superheat: The wall temperature minus the saturated temperature

Wall temperature: The average wetted temperature

Wetted fraction: the fraction of the surface that is covered by liquid

Bibliography

[1] M. Corradini, “Thermal Hydraulics of Nuclear Systems,” 2015.

[2] S. S. Kutateladze, “On the transition to film boiling under natural convection,” *Kotloturbostroenie*, vol. 3, pp. 10–12, 1948.

[3] N. Zuber and R. Corporation, “Hydrodynamic Aspects of Boiling Heat,” 1959.

[4] K. Dhir and H. Lienhard, “Extended Hydrodynamic Theory of the Peak and Minumum Pool Boiling Heat Fluxes,” *NASA*, no. July, 1973.

[5] W. M. Rohsenow, P. Griffith, T. H. E. Office, and O. F. Naval, “Correlation of maximum heat flux data for boiling of saturated liquids,” *Off. Nav. Res.*, 1955.

[6] Y. Haramura and Y. Katto, “A new hydrodynamic model of critical heat flux, applicable widely to both pool and forced convection boiling on submerged bodies in saturated liquids,” *Int. J. Heat Mass Transf.*, vol. 26, no. 3, pp. 389–399, 1983.

[7] C. K. Guan, J. F. Klausner, and R. Mei, “A new mechanistic model for pool boiling CHF on horizontal surfaces,” *Int. J. Heat Mass Transf.*, vol. 54, no. 17–18, pp. 3960–3969, 2011.

[8] A. K. Rajvanshi, J. S. Saini, and R. Prakash, “Investigation of macrolayer thickness in nucleate pool boiling at high heat flux,” *Int. J. Heat Mass Transf.*, vol. 35, no. 2, pp. 343–350, 1992.

[9] H. S. Ahn and M. H. Kim, “Visualization study of critical heat flux mechanism on a small and horizontal copper heater,” *Int. J. Multiph. Flow*, vol. 41, pp. 1–12, 2012.

[10] S. Gong, W. Ma, and T. N. Dinh, “An experimental study of rupture dynamics of evaporating liquid films on different heater surfaces,” *Int. J. Heat Mass Transf.*, vol. 54, no. 7–8, pp. 1538–1547, 2011.

[11] I. C. Bang, S. H. Chang, and W.-P. Baek, “Visualization of a principle mechanism of critical heat flux in pool boiling,” *Int. J. Heat Mass Transf.*, vol. 48, no. 25–26, pp. 5371–5385, 2005.

[12] S. G. Kandlikar, “A Theoretical Model to Predict Pool Boiling CHF Incorporating Effects of Contact Angle and Orientation,” *J. Heat Transfer*, vol. 123, no. 6, p. 1071, 2001.

[13] S. G. Kandlikar and M. E. Steinke, “Contact angles and interface behavior during rapid evaporation of liquid on a heated surface,” *Int. J. Heat Mass Transf.*, vol. 45, no. 18, pp. 3771–3780, 2002.

[14] J. P. 0’Connor and S. M. You, “A Painting Technique to Enhanc.pdf,” *J. Heat Transfer*, vol. 117, pp. 387–393, 1995.

[15] H. O’Hanley, C. Coyle, J. Buongiorno, T. McKrell, L. W. Hu, M. Rubner, and R. Cohen, “Separate effects of surface roughness, wettability, and porosity on the boiling critical heat flux,” *Appl. Phys. Lett.*, vol. 103, no. 2, pp. 2011–2016, 2013.

[16] M. Mccarthy, M. Rahman, and E. Olceroglu, “Role of Wickability on the Critical Heat Flux of Structured Superhydrophilic Surfaces,” *Langmuir*, vol. 30, pp. 11225–11234, 2014.

[17] T. G. Theofanous, J. P. Tu, a T. Dinh, and T. N. Dinh, “The Boiling Crisis Phenomenon, J,” *Exp. Therm. Fluid Sci. P*, vol. 26, pp. 6–7, 2002.

[18] T. G. Theofanous, T. N. Dinh, J. P. Tu, and a. T. Dinh, “The boiling crisis phenomenon part II: Dryout dynamics and burnout,” *Exp. Therm. Fluid Sci.*, vol. 26, no. 6–7, pp. 793–810, 2002.

[19] C. Gerardi, J. Buongiorno, L.-W. Hu, and T. McKrell, “Infrared thermometry study of nanofluid pool boiling phenomena.,” *Nanoscale Res. Lett.*, vol. 6, no. 1, p. 232, 2011.

[20] T. H. Kim, E. Kommer, S. Dessiatoun, and J. Kim, “Measurement of two-phase flow and heat transfer parameters using infrared thermometry,” *Int. J. Multiph. Flow*, vol. 40, pp. 56–67, 2012.

[21] I.-C. Chu, H. C. No, and C.-H. Song, “High Heat Flux Boiling Structure and CHF Mechanism in a Horizontal Pool Boiling,” *8th Int. Conferance Boil. Condens. Heat Transf.*, 2012.

[22] S. Nishio and H. Tanaka, “Visualization of boiling structures in high heat–flux pool-boiling,” *Int. J. Heat Mass Transf.*, vol. 47, no. 21, pp. 4559–4568, 2004.

[23] J. Jung, S. J. Kim, and J. Kim, “Observations of the critical heat flux process during pool boiling of FC-72,” *J. Heat Transfer*, vol. 136, no. 4, p. 41501, 2014.

[24] A. Ono and H. Sakashita, “Measurement of surface dryout near heating surface at high heat fluxes in subcooled pool boiling,” *Heat Mass Transf.*, vol. 52, pp. 814–821, 2009.

[25] A. Ono and H. Sakashita, “Liquid–vapor structure near heating surface at high heat flux in subcooled pool boiling,” *Int. J. Heat Mass Transf.*, vol. 50, no. 17–18, pp. 3481–3489, 2007.

[26] H. Sakashita and A. Ono, “Boiling behaviors and critical heat flux on a horizontal plate in saturated pool boiling of water at high pressures,” *Int. J. Heat Mass Transf.*, vol. 52, no. 3–4, pp. 744–750, 2009.

[27] N. Seiler-Marie, J. M. Seiler, and O. Simonin, “Transition boiling at jet impingement,” *Int. J. Heat Mass Transf.*, vol. 47, pp. 5059–5070, 2004.

[28] H. Auracher and W. Marquardt, “Experimental studies of boiling mechanisms in all boiling regimes under steady-state and trnsient conditions,” *Int. J. Therm. Sci.*, vol. 41, no. 7, pp. 586–598, 2002.

[29] H. Robidou, H. Auracher, P. Gardin, and M. Lebouche, “2002_Robidou_Controlled cooling of a hot plate with a water jet.pdf,” *Exp. Therm. Fluid Sci.*, vol. 26, pp. 123–129, 2001.

[30] D. H. Wolf, F. P. Incropera, and R. Viskanta, “Local jet impingement boiling heat transfer,” *Heat Mass Transf.*, vol. 39, pp. 1395–1406, 1996.

[31] D. E. Hall, F. P. Incropera, and R. Viskanta, “Jet Impingement Boiling From a Circular Free-Surface Jet During Quenching- Part 1—Single-Phase Jet,” *Journal*, vol. 123, pp. 911–917, 2001.

[32] D. E. Hall, F. P. Incropera, and R. Viskanta, “Jet Impingement Boiling From a Circular Free-Surface Jet During Quenching: Part 2—Two-Phase Jet,” *J. Heat Transfer*, vol. 123, no. October, p. 911, 2001.

[33] A. Sharan and J. H. Lienhard, “On predicting burnout in the jet-disk configuration,” *J. Heat Transfer*, vol. 107, pp. 398–401, 1985.

[34] Y. Qiu and Z. Liu, “Critical heat flux of steady boiling for saturated liquids jet impinging on the stagnation zone,” *Int. J. Heat Mass Transf.*, vol. 48, no. 21–22, pp. 4590–4597, 2005.

[35] Y. Qiu and Z. Liu, “Nucleate boiling on the superhydrophilic surface with a small water impingement jet☆,” *Int. J. Heat Mass Transf.*, vol. 51, no. 7–8, pp. 1683–1690, 2008.

[36] M. J. Rau and S. V. Garimella, “Confined Jet Impingement With Boiling on a Variety of Enhanced Surfaces,” *J. Heat Transfer*, vol. 136, no. 10, p. 101503, 2014.

[37] M. J. Rau, S. V. Garimella, E. M. Dede, and S. N. Joshi, “Boiling Heat Transfer From an Array of Round Jets With Hybrid Surface Enhancements,” *J. Heat Transfer*, vol. 137, no. 7, p. 071501, 2015.

[38] C. H. Shin, K. M. Kim, S. H. Lim, and H. H. Cho, “Influences of nozzle-plate spacing on boiling heat transfer of confined planar dielectric liquid impinging jet,” *Int. J. Heat Mass Transf.*, vol. 52, no. 23–24, pp. 5293–5301, 2009.

[39] S. Garimella, “Nozzle-geometry effects in liquid jet impingement heat transfer,” *Int. J. Heat Mass Transf.*, vol. 39, no. 14, pp. 2915–2923, 1996.

[40] Z.-H. Liu and J. Wang, “Study on film boiling heat transfer for water jet impinging on high temperature flat plate,” *Heat Mass Transf.*, vol. 44, pp. 2475–2481, 2000.

[41] W. Timm, K. Weinzierl, and a. Leipertz, “Heat transfer in subcooled jet impingement boiling at high wall temperatures,” *Int. J. Heat Mass Transf.*, vol. 46, pp. 1385–1393, 2003.